TUNING AND OPTOMECHANICS OF COUPLED PHOTONIC CRYSTAL NANOBEAM CAVITIES

DU HAN

(*B.S., Shanghai Jiao Tong University, China*)

A THESIS SUBMITTED

FOR THE DEGREE OF DOCTOR OF PHILOSOPHY

DEPARTMENT OF MECHANICAL ENGINEERING

NATIONAL UNIVERSITY OF SINGAPORE

2016

DECLARATION

I hereby declare that the thesis is my original work and it has been written by me in its entirety. I have duly acknowledged all the sources of information which have been used in the thesis.

This thesis has also not been submitted for any degree in any university previously.

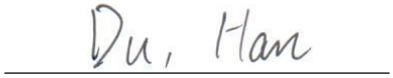

Du, Han

8th September, 2016

Acknowledgements

Herein I would like to own my sincere gratitude to all persons who have helped me with this dissertation.

Firstly, I would like to express my acknowledgement to my main supervisor Prof. Zhou, Guangya for his continuous support of my Ph.D study and related research, for his patience, motivation, and immense knowledge. His guidance helped me in all the time of research and writing of this thesis. I could not have imagined having a better supervisor for my Ph.D study. Besides my main supervisor Prof. Zhou, my co-supervisor Prof. Chau, Fook Siong and Dr. Deng, Jie also advised me a lot for my Ph.D project and I would like to acknowledge them as well.

Besides my supervisors, I would like to thank my senior colleagues in my research group, Dr. Du, Yu, Dr. Mu, Xiaojing, Dr. Shi, Peng, Dr. Tian, Feng, Dr. Zhang, Wei, Dr. Zhang, Xingwang, Dr. Chen, Guoqiang and Mr. Zou, Yongchao, for their valuable suggestions and assistance on device designs, fabrications and measurements.

My sincere thanks also goes to researchers, Dr. Tang, Xiaosong and Mr. Chen, Yifan from Institute of Materials Research and Engineering (IMRE), Mr. Zhao, Yunshan from Cicfar Lab, ECE Dept, Dr. Ren, Yaping from Centre for Quantum Technologies, *etc*. They also provided much help to my research work, including device fabrication, characterization and testing.

I’m also thankful to our laboratory staff, Mr. Suhaimi Bin Daud, Mr. Goh Tiong Lai, Alvin, Mr. Abdul Malik Bin Baba, and Mrs. Low-Chee Sui Cheng, Amy for their technical support to our laboratory facilities and house-keeping service to our laboratory and office.

As to the financial support to my Ph. D project, I would like to thank the Singapore MOE research grant No. R-265-000-416-112.

At the end, I would like to acknowledge my parents for their love, patience, and support.

Du, Han

NUS, Singapore

September 2016

Table of Contents

Summary

The history of micro-electromechanical systems (MEMS) can be traced back to the 1960s. In the past decades, worldwide researchers committed themselves to the development of such micro systems. MEMS devices benefit not only from space advantage but also high performance. Thanks to the further development of micro and nano fabrication techniques, the footprint of MEMS devices can be further shrunk to nano-scale and thus nano-electromechanical systems (NEMS) emerged. Such MEMS/NEMS devices have many merits, including ultra-low energy consumption, ultra-small footprint, high operating rate and low per unit cost compared with macro devices.

Si nano photonics has also been widely studied due to their potential in future optical communication, signal processing systems, *etc*. Compared with conventional optical systems, nano photonic devices also have the merits of on-chip compatibility, low energy consumption, and ultra-high operating rate. Importantly, such Si photonic devices can be fabricated together with the nano mechanical devices using a series of standard nano fabrication processes and thus Si photonic devices can be easily integrated with NEMS actuators. Consequently, it is believed that the combination of nano mechanics and nano photonics has promising future not only in academia but also in engineering. As reported in literatures, on-chip optical gradient force has the capability to deform and reconfigure nano structures and thus it is promising to develop

optical force driven devices for all-optical systems.

This thesis focuses on mechanical tuning and optomechanics of photonic devices based on coupled photonic crystal nanobeam cavities, with studies including nano fabrication process development, device tuning with NEMS actuators, investigation of optical gradient force and tunable cavity optomechanics.

High efficiency resonance tuning by electrostatically shifting the coupled nanobeam cavities in the lateral direction has been achieved. Coupling strength tuning over wide range with high precision is demonstrated and the repeatability and dynamic tuning are also proven, as well as the mode symmetry inversion. Based on the lateral tuning, lateral shearing optical gradient force is predicted and demonstrated in experiments. It is the first study of such lateral shearing optical force according to the author's knowledge. The study of optical force has great potential in all-optical system development. Thus, a more attractive area, cavity optomechanics, is also investigated in this thesis and a tuning method of cavity optomechanics is proposed and experimentally demonstrated.

List of Publications

Journal papers

[1] **Du, H.**, Zhang, X., Deng, J., Zhao, Y., Chau, F. S., & Zhou, G. (2016). Lateral shearing optical gradient force in coupled nanobeam photonic crystal cavities. *Applied Physics Letters*, **108**(17), 171102.

[2] **Du, H.**, Zhang, X., Chen, G., Deng, J., Chau, F. S., & Zhou, G. (2016). Precise control of coupling strength in photonic molecules over a wide range using nanoelectromechanical systems. *Scientific Reports*, **6**, 24766.

[3] **Du, H.**, Chau, F. S., & Zhou, G. (2016). Mechanically-Tunable Photonic Devices with On-Chip Integrated MEMS/NEMS Actuators. *Micromachines*, **7**(4), 69.

[4] **Du, H.**, Zhou, G., Chau, F. S. (2016). A Micromachined Tunable Bistable Mechanism. *IEEE J. MEMS*, **25**(4), 708-715

[5] Zhang, X., Zhou, G., Shi, P., **Du, H.**, Lin, T., Teng, J., & Chau, F. S. (2016). On-chip integrated optofluidic complex refractive index sensing using silicon photonic crystal nanobeam cavities. *Optics letters*, **41**(6), 1197-1200.

[6] Shi, P., **Du, H.**, Chau, F. S., Zhou, G., & Deng, J. (2015). Tuning the quality factor of split nanobeam cavity by nanoelectromechanical systems. *Optics express*, **23**(15), 19338-19347.

Conference proceedings

[7] **Du, H.**, Lin, T., Shi, P., Tian, F., Chau, F. S., & Zhou, G. (2014). Design of a resonant magnetic field sensor based on coupled 1-D photonic crystal cavities. In *Optical MEMS and Nanophotonics (OMN), 2014 International Conference on* (pp. 199-200), IEEE.

[8] **Du, H.**, Chau, F. S., Zhou, G. (2016). A Tunable Micro Bistable Mechanism. In *8th Asia-Pacific Conference of Transducers and Micro/Nano Technologies (APCOT 2016).*

[9] **Du, H.**, Zhang, X., Deng, J., Chau, F. S., Zhou, G. (2016). Lateral Shearing Tuning of Dual-coupled Photonic Crystal Nanobeam Cavities. In *Optical MEMS and Nanophotonics (OMN), 2016 International Conference on* (pp. 89-90), IEEE.

List of Figures

List of Tables

List of Symbols

a	cavity holes period
b	width
d	displacement
d_{om}	optomechanical wavelength detuning coefficient
E	Young's Modulus
F	force
g	gap
g_{om}	optomechanical coupling coefficient
k	spring constant
L, l	length
n	index
m	number
P, p	optical mode
r	radius
T	transmission
ΔT	temperature change
t	thickness
U	potential energy
V	voltage
β	propagation constant
ω /$\Delta\omega$	frequency (angular frequency) / frequency detuning
ρ	attenuation constant
κ	coupling coefficient
ε	permittivity
χ	eigenvalue
φ / $\Delta\varphi$	phase / phase difference
Ω_M	mechanical resonance frequency
γ_M	mechanical damping factor
τ	photo lifetime
$1/\tau_w$	cavity decay rate due to feeding waveguide coupling loss
$1/\tau_i$	intrinsic loss of the cavity
asterisk *	complex conjugate

Abbreviations

1D	one-dimensional
2D	two-dimensional
3D	three-dimensional
AC	alternating current
CMT	coupled mode theory
DC	direct current
DI water	distilled water
DIP	dual in-line package
DRIE	deep-RIE
EBL	electron beam lithography
EDFA	erbium doped fiber amplifier
FDTD	finite-difference time-domain
FEM	finite element method
FIB	focused ion beam
HF	hydrogen acid
HMDS	hex-methyl-di-silazane
IPA	isopropyl
MEMS	micro-electromechanical systems
MZI	Mach-Zehnder interferometer
NEMS	nano-electromechanical systems
OSA	optical spectrum analyzer
PhC	photonic crystal
Q factor	quality factor
RIE	reactive-ion-etching
SEM	scanning electron microscope
SOI	silicon-on-insulator
TE	transverse electric
TLS	tunable laser source
WGM resonator	whispering-gallery-mode resonator

Chapter 1. Introduction

1.1. Research Background

Nowadays, semiconductors play an important role in our lives. Semiconductor components take an irreplaceable place in modern electrical and electronic equipment, ranging from radios to satellites. Yet the development of semiconductor-based electronic devices has seemingly reached a bottleneck. Due to issues such as parasitic capacitance, the operating rate of semiconductor components is limited and cannot be further enhanced with conventional methods [1]. To address such limitations and make breakthroughs, both industrial and academic researchers are trying their best to investigate novel technologies as alternatives. Many of them have turned their eyes to photonic techniques. Photonics utilizes photons as the information carrier instead of electrons. Photonic signal processing has already been proven to have ultra-high operation rate and low crosstalk between channels [2, 3]. Yet the cost and yield problem still limits the further industrialization and commercialization of photonic technology, while conventional electronic devices already can be industrially manufactured with low cost and high yields [4]. The trade-off between electronics and photonics is widely discussed in literatures [5-10]. It is believed that these two technologies can be combined together to complement each other.

The key advantage of photonic techniques over conventional electronic techniques is their potential ultra-high operation rate. Numerous studies have been carried out to

develop methods to dynamically control photonic devices, known as tunable photonics, which has many advantages such as flexibility and error compensation. Based on existing studies, the traditional tuning mechanisms for on-chip photonic devices can be generally classified into three groups, thermo-optic [11], electro-optic [12, 13], and mechanical methods. Among them, thermo-optical methods have the advantage of a relatively wide tuning range, but they are limited by their slow operating speed and high energy consumption [11] and thus are not ideal for practical applications. Electro-optic methods are fast in general but they suffer from a limited tuning range because the tuning is based on the manipulation of optical indices, which vary only slightly with respect to modulation voltage [14]. Besides, electro-optical methods and thermo-optical methods do not have the capability to drastically reconfigure the photonic structures or significantly tune the coupling strength between them, which describes the interaction between them and is determined by the mode overlap integral of them. In contrast, mechanical tuning, mechanically displacing or deforming structures, is a natural way to tune photonic devices and has many outstanding advantages over other methods. Despite the drawbacks of electro-optical methods, electro-optical tuning still dominates current studies of tunable photonics and is relatively mature compared with mechanical tuning. Yet the nascent mechanical tuning methods are believed to be good candidates to complement the electro-optical tuning and further accelerate the development of photonic technologies [15].

Actuation using micro/nano-electromechanical systems (MEMS/NEMS) is the most

widely used on-chip mechanical tuning method and the history of MEMS can be traced back to the last century [16-18]. To date, MEMS devices are widely commercialized; for example, MEMS actuators are utilized to drive the micro cameras on cell phones. Thanks to the development of micro and nano fabrication techniques, MEMS devices has further shrunk and thus, NEMS devices have emerged [19, 20]. NEMS technology is rapidly developing and NEMS actuators and sensors are employed for various state-of-art studies, for example, a study regarding the near-field radiation heat transfer in nano-scale, in which ultra-precise and reversible mechanical control is required and realized using a NEMS electrostatic actuator [21].

Silicon photonic devices are widely built with materials like single crystal silicon, poly-silicon, and silica including silicon oxide, silicon nitride, *etc.* and they have already proven to have strong capabilities in infrared (IR) light confinement and modulation [22, 23]. Silicon and silica are commonly-used MEMS/NEMS materials as well, making it possible to build photonic devices on-chip monolithically integrated with MEMS/NEMS actuators. More importantly, it is easy to combine their fabrication processes and there exist well-established fabrication techniques for such device manufacturing. The existing studies of on-chip mechanical tuning of photonic devices with MEMS\NEMS actuators will be reviewed in detail in the next chapter.

With the development of photonic technologies, the on-chip optical gradient force is reported to have the capability to deform and thus reconfigure nano structures [24, 25].

Besides, compared with conventional optical force generated by free-space light used for optical trapping, the on-chip optical gradient force generated by guided modes in photonic structures can be bipolar, portending a promising future of all-optical controlled photonic systems. Furthermore, on-chip cavity optomechanics is more attractive, in which the optical and mechanical degrees of freedom are coupled together. Using cavity optomechanics, mechanical cooling and amplification can be realized as a result of the interaction between photons and phonons [26]. Optical systems for communication and signal processing based on cavity optomechanics are also believed to be promising. The current progress of on-chip optical gradient force and cavity optomechanics will be reviewed in the next chapter.

1.2. Objectives

This thesis describes the study of on-chip mechanical tuning and cavity optomechanics of photonic devices based on coupled photonic crystal nanobeam cavities. The four main goals are to:

(1) Develop nano fabrication process and testing methods for on-chip mechanically tunable photonic devices and optomechanical devices.

(2) Investigate the photonic device tuning with mechanical methods and demonstrate a resonance tuning in a dual-coupled photonic crystal nanobeam cavities system with integrated NEMS actuators; and study the coupling strength tuning based on

such tuning mechanism.

(3) Study the on-chip optical gradient force and investigate a novel lateral shearing optical force generated by dual-coupled photonic crystal nanobeam cavities; and develop a measurement method to detect the proposed optical force in static mode.

(4) Study the on-chip cavity optomechanics; and develop and demonstrate a tuning method for cavity optomechanics in coupled photonic crystal nanobeam cavities.

Due to limitations, the photonic devices that are experimentally investigated in this thesis are based on single crystal silicon and thus the devices are all passive.

1.3. Outline of the Thesis

The thesis starts with an introduction chapter, Chapter 1, regarding the research background, objectives and outline of this thesis.

Chapter 2 reviews existing studies related to the study in this thesis. The review is divided into four sections, photonic crystal cavities, MEMS/NEMS tunable photonic devices, on-chip optical gradient force and on-chip cavity optomechanics.

Chapter 3 mainly discusses the nano fabrication process developed for the photonic devices investigated in this thesis. The testing equipment and setup are also introduced.

Chapter 4 discusses a study of the lateral tuning of dual-coupled photonic crystal

nanobeam cavities. It starts with a design principle of the cavities investigated in the proposed study. Then coupled mode theory is investigated as the basic theory of the study in this chapter. Device design is sequentially introduced. Finally, the theoretical and experimental results are presented and discussed.

Chapter 5 presents a study of the lateral shearing optical gradient force in coupled photonic crystal nanobeam cavities. The physics of optical gradient force is first briefly described and then the optical force generated by coupled photonic crystal nanobeam cavities is introduced. The experimental methods and results are elaborated upon and discussed.

Chapter 6 proposes a tuning method for on-chip cavity optomechanics based on dual-coupled cavities. The theory of cavity optomechanics is briefly discussed and the proposed method is experimentally demonstrated.

Chapter 7 lists the main conclusions of the studies in this thesis and proposes some future research suggestions.

Chapter 2. Literature Review

This chapter reviews existing studies related to tunable photonic devices and cavity optomechanics of on-chip photonic devices. The review covers four topics, photonic crystal cavities, MEMS/NEMS tunable photonic devices, on-chip optical gradient force and on-chip cavity optomechanics.

2.1. Photonic Crystal Cavities

The photonic devices investigated in this thesis are based on photonic crystal nanobeam cavities. Due to the large volume of literature on photonic crystal cavities, the topic of PhC cavities will be selectively reviewed only in this section. Yet, studies of NEMS tunable PhC cavities will be reviewed in detail in the next section.

Optical resonators with high quality factors (Q factor) and small mode volume are powerful tools to manipulate light and matter. Such resonators can be applied to diverse areas, including quantum technology [27], optical trapping [28], optofluidics [29], nonlinear optics [30], and nanoparticle detection [31, 32]. Among optical resonators, photonic crystal cavities, when compared with other kinds of optical resonators or non-resonant structures, have been demonstrated to have many advantages [33-36].

Photonic crystal (PhC) [37, 38], a kind of photonic bandgap structure, is an optically functional periodic structure. Analogous to semiconductor materials in which a periodic atom array can affect electron collective motions, photonic crystals can confine photons

due to Bragg scattering, resulting in bandgaps. Photons with frequencies within photonic bandgaps cannot propagate in the crystal. Photonic components based on conventional rectangular waveguides can also be achieved using photonic crystals such as photonic crystal waveguide filters [22] and couplers [39]. However, one of the most attractive usages of photonic crystals is for building PhC cavities by inducing defects into them.

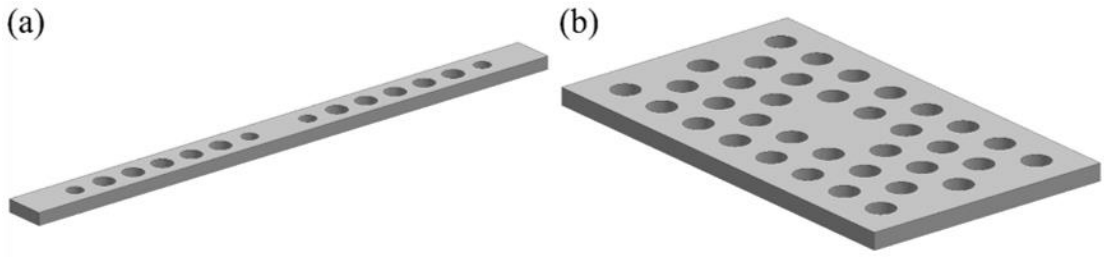

Figure 2.1 Schematics of (a) 1D PhC cavity and (b) 2D PhC cavity.

PhC cavities can be generally grouped into three types: one-dimensional (1D), two-dimensional (2D) and three-dimensional (3D) cavities. Among these, 3D cavities are difficult to be fabricated on-chip and characterized, whilst 1D and 2D cavities are the most widely studied. Typical configurations are shown in Figs. 2.1(a) and (b). 2D PhC cavities are formed by inducing defects inside a planar photonic crystal [40]. Reported 2D cavities that are fabricated on silicon-on-insulator (SOI) material systems can have Q factors of over 10^6 [35]. Similarly, 1D PhC cavities (also known as nanobeam cavities) built by putting two PhC Bragg mirrors together to form a Fabry-Pérot-like resonator can also have Q factors of over 10^6 [41-43].

These PhC cavities can be applied to diverse areas. For example, optical switching can

be realized in photonic crystal cavities based on the mechanism of nonlinear index variation caused by the plasma effect of carriers generated by two-photon absorption [44]. In optical switching, characterizations of the high quality factor and small mode volume are desired because these characterizations can lead to the reduction of switching energy. PhC cavities have also been proven to realize strong coupling of matter and light [45-48], which has great potential in the studies of cavity quantum electrodynamics. Other applications, like PhC lasers [49] and chemical sensing [50, 51] have also been demonstrated.

PhC nanobeam (1D) cavities have the merit of a small footprint and thus the ease to be mechanically controlled. Consequently, they become a powerful alternative to 2D PhC cavities. Dual-coupled nanobeam cavities also have intrinsic symmetric and anti-symmetric supermodes. More importantly, compared with 2D cavities, 1D cavities have ultra-high design flexibility [42, 43]. A design principle will be introduced in Chapter 4. In a word, it is reasonable to employ PhC nanobeam cavities for the study in this thesis.

2.2. MEMS/NEMS Tunable Photonic Devices

With electrostatic tuning of photonic structures based on diverse configurations including waveguides, ring/disk resonators and PhC cavities, various applications like tunable optical modulators, couplers, filters, routers and switches are developed. The tuning using MEMS/NEMS has already been proven to be advantageous, which will be

reviewed in this section.

2.2.1. MEMS/NEMS tunable photonic devices based on waveguides and ring/disk resonators

A dielectric rectangular waveguide is a conventional on-chip photonic structure for wave-guiding, in which the light is confined by total internal reflection with a higher index than its surrounding. Mechanically tunable photonic devices based on waveguides are generally built with configurations of segmented waveguides, coupled waveguides and their derivatives.

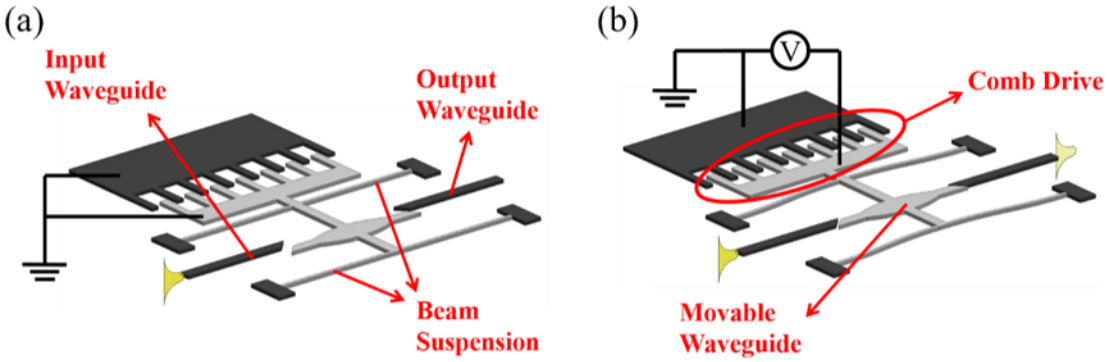

Figure 2.2 Schematics of the (a) "off" and (b) "on" states of the switch based on segmented waveguides configuration. The light grey parts denote movable structures while the dark grey parts indicate fixed structures. (The schematics in the figures below in this chapter follow the same rule.)

Instinctively, the transmission of light along segmented waveguides is roughly proportional to the total effective mode overlap integral of the waveguide cross-sections, which varies with the offset of the centers of the fixed and movable waveguide segments. Thus, one can build an optical switch by mechanically moving the central movable waveguide segment [52]. The switch configuration is illustrated by Figs. 2.2(a)

and (b), from which it can be seen that the switch utilizes a monolithically integrated comb drive actuator. The comb drive actuator actuates through electrostatic attraction. For more details of MEMS/NEMS comb drive, one can refer to Refs [53, 54]. The movable fingers of the comb drive are rigidly connected to the movable waveguide segment, while the entire movable structure is supported by beam suspensions. At the initial condition, the movable waveguide segment has a large offset from the fixed input and output waveguides and the transmission is nearly zero, indicating an "off" state of the switch. If a voltage is applied across the fixed and movable fingers of the comb drive, the movable waveguide segment is displaced and thus the offset is reduced; the transmission thus increases, representing an "on" state. Such comb drive and beam suspensions can be standardly designed [55] for large displacements with high positioning accuracy. This segmented waveguides configuration can also be applied to transduction [56] and displacement sensing [57] applications. Other optical switches and filters can also be achieved with a similar segmented waveguides design [58, 59].

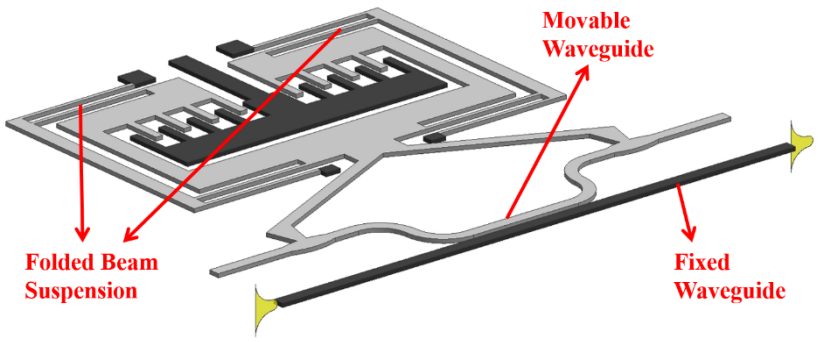

Figure 2.3 Schematic of the tunable waveguide coupler controlled by a comb drive actuator.

Similar NEMS actuation and supporting methods can be used to build coupler switches

based on coupled waveguides [60-65]. As illustrated in Fig. 2.3, this device is also actuated with comb drive, while folded beam suspensions instead of straight beam suspensions are used to support the movable structure to release potential residual stresses that may result from fabrication. Light is launched into and collected from the fixed waveguide. A comb drive similar to that described above is used to control the coupling gap between the coupled waveguides by varying the applied voltage, in which case the output light can be modulated. Extinction ratio of over 10 dB at a wavelength of 1550 nm was reported to be experimentally demonstrated on such coupler switches [61] with a measured rise time of about 18 μs [62]. In addition, a similar 1×3 switch has also been developed based on triple-coupled waveguides configuration [65]. Besides in-plane tuning of the dual-coupled waveguides, out-of-plane tuning has also been investigated for on-chip large scale switches [66, 67]. It is noted that not only the output light intensities can be controlled by tuning the coupling gap between the waveguides, but the output phase information can also be modulated. For example, a phase shifter has been developed based on a similar principle of waveguide coupling [68], in which the electrostatic force is applied directly to the waveguides with a voltage across them.

Besides changing the coupling gap, moving one of the waveguides along its length direction while maintaining a constant coupling gap will result in light modulation as a result of variation in the effective optical path length. This method is also known as delay line modulation and can be used to control optical phase information [69-71]. A

combination of optical path length tuning and coupling strength tuning is also possible [72].

Due to intrinsic light field resonant enhancement, optical resonators are widely used for light control because they are wavelength-selective and usually have relatively high sensitivity to tuning. A well-known family of conventional micro optical resonators is micro ring/disk resonators, also known as whispering-gallery-mode (WGM) resonators. Reported ring/disk resonators fabricated with silicon/silica materials can have *Q* factors of over 10^8 [73]. Generally, a ring resonator system consists of a ring and coupled channel waveguides, which is a classic wavelength-selective add-drop filter with four ports named as input, through, add and drop.

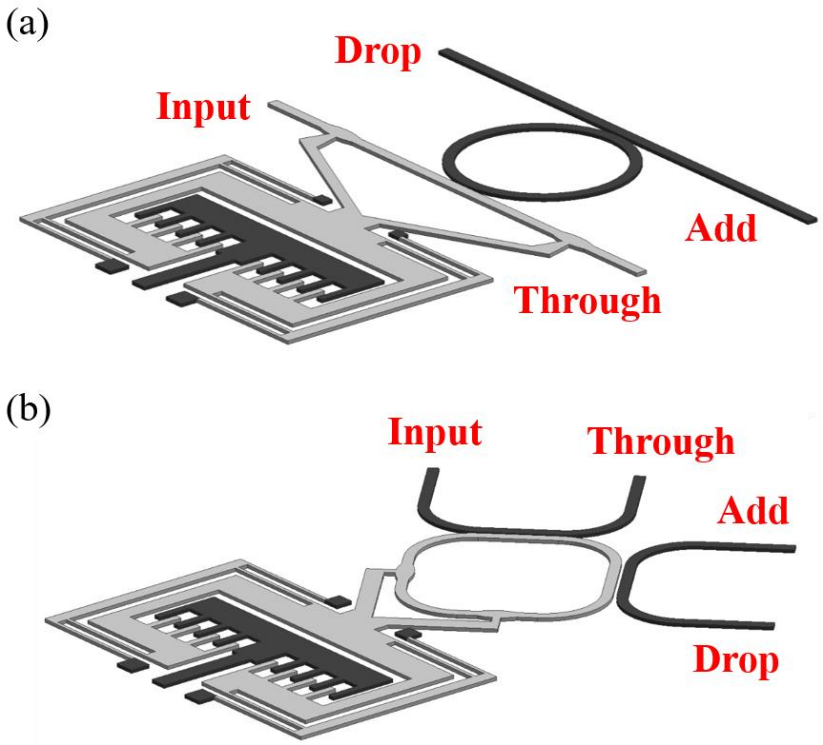

Figure 2.4 Schematics of the tuning mechanisms based on the ring resonator system by mechanically moving (a) the channel waveguide and (b) the ring.

By tuning the coupling strength between the ring and channel waveguides through like changes in the coupling gap, the system's resonance wavelength and/or the full width at half maximum (FWHM) can be manipulated. Such a tuning mechanism can be realized by translating the channel waveguide (see Fig. 2.4(a)) [74-76] or the ring (see Fig. 2.4(b)) [77] with the integrated comb drive. The coupling gap between the ring and channel waveguides can be controlled by applying different voltages to the comb drive.

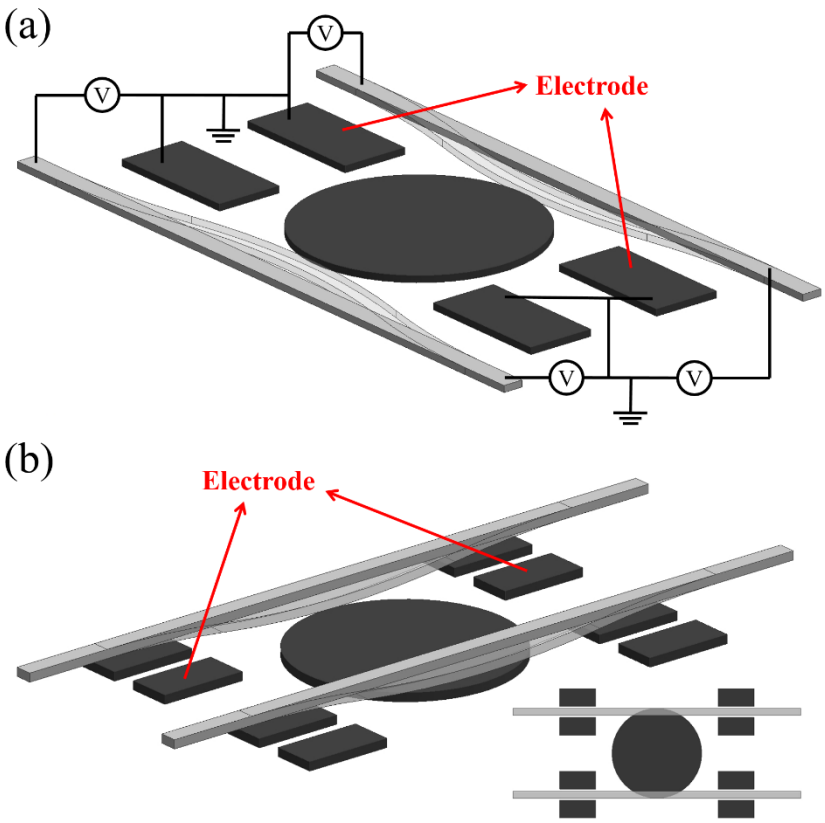

Figure 2.5 Schematics of (a) in-plane and (b) out-of-plane tuning mechanisms for add-drop filters, consisting of a disk resonator coupled with suspended channel waveguides.

A relatively simple way to tune the coupling strength between the channel waveguides and the resonator through deformation of the waveguides has also been reported [78]. As illustrated in Fig. 2.5(a), two free-standing waveguides are coupled with a disk resonator. When a voltage is applied across the waveguides and the on-chip fixed

electrodes as shown in the figure, the flexible waveguides will bend towards the disk, thus obviating the need for an additional bulky MEMS actuator. (It is noted that the displacement control accuracy and driving range of this kind of electrostatic actuator is not comparable to that of the comb drive.) The results of wavelength switching with an extinction ratio of 9 dB were reported. Besides in-plane waveguides actuation, out-of-plane waveguides bending (see Fig. 2.5(b)) that achieved an enhanced extinction ratio of over 20 dB has also been reported [79, 80]. As shown, the channel waveguides are suspended above the disk and the vertical coupling gap between them can be adjusted with a voltage applied across the suspended waveguides and the electrodes beneath them. When coupled out-of-plane, the waveguides are tangentially positioned as illustrated in the inserted top view to obtain a relatively strong coupling between the disk and waveguides. Such an add-drop filter has been demonstrated to have a wide tunable bandwidth, ranging from 12 to 27 GHz [81].

Besides static tuning, dynamic modulation based on such devices has also been demonstrated to have a high signal to noise ratio [82]. In the study cited in [83], dynamic optical intensity modulation controlled by an electrically-excited mechanical resonator is experimentally demonstrated.

2.2.2. MEMS/NEMS tunable photonic devices based on PhC cavities

PhC cavities, as introduced in Section 2.1, are another advantageous group of optical resonators and also can be functionalized through mechanical tuning. For example,

MEMS/NEMS actuators can be integrated to vary the coupling between PhC cavities and waveguides, thereby enabling a range of tunable photonic devices. Kanamori *et al*. developed a wavelength-selective channel drop switch with a 2D PhC cavity in-plane coupled to a movable waveguide with the gap between them controlled by a comb drive [84]. The drop efficiency can be controlled to 12.5 dB with a 600 nm gap variation. The combination of MEMS/NEMS with PhC cavities can form mechanically-tunable photonic resonators/cavities, which are attractive for quantum signal processing [46], controlling of slowing and stopping light [85], tunable lasers [86] and many other applications.

Resonance control of optical resonators has long been studied and numerous mechanically tuning methods that do not modify the nature of the resonators have been developed. One of the established methods utilizes evanescent field perturbation (or proximity perturbation), in which dielectric probes or cantilevers are suspended above 2D PhC cavities [87, 88] or micro ring resonators [89, 90] through complicated fabrication processes and driven by non-monolithic actuators. Besides the complicated system configuration, generally, only small tuning ranges can be achieved with relatively large mechanical displacements. To enhance the tuning range using evanescent field perturbation, Chew *et al*. studied near-field perturbation to 1D PhC cavities using nano-scale probes driven by monolithic NEMS comb drive actuators [91, 92]. In these reported studies, nano probes with different shapes are investigated and compared. However, the probe perturbation methods also suffer from transmission and

Q factor degradation and the tuning range is still small though relatively enhanced.

To develop a cavity resonance tuning method with large tuning range and without significant transmission and *Q* factor reduction, the coupled-cavity tuning approach is proposed. When two cavities are coupled together, the resonance frequencies of their coupled supermodes can be adjusted by controlling the coupling coefficient between them, which is determined by the overlap integral of the mode fields of the two resonators. The coupling between two optical resonators could be described by the well-established temporal coupled mode theory (CMT), which will be introduced in detail in Section 4.2. Essentially resonance control can be realized by tuning the coupling strength, which can be easily implemented with on-chip integrated MEMS/NEMS actuators. A number of experimental demonstrations of the coupled-cavity resonance tuning approach have been reported. They are commonly based on 1D (nanobeam) PhC cavities due to their small footprint and ease of mechanical control. For example, when a voltage is applied across two in-plane-coupled 1D cavities, the induced electrostatic force pulls the two cavities together and thus changes the coupling strength between them [93]. A resonance wavelength shift of up to 9.5 nm on an even mode was observed. Using a similar method, vertically-coupled nanobeam cavities can also be electrostatically controlled [94]. In order to achieve large variations in coupling gap and, consequently, large wavelength tuning ranges, integration of MEMS/NEMS comb drive actuators with PhC cavities is found to be highly advantageous.

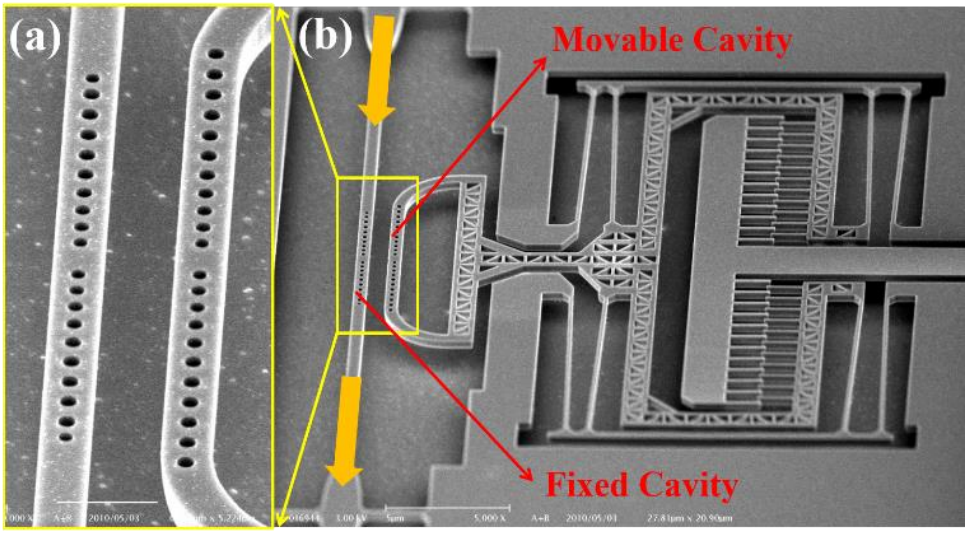

Figure 2.6 SEM images of (a) close-up view of the dual-coupled nanobeam cavities and (b) NEMS comb drive controlled dual-coupled nanobeam cavities system.

Figures 2.6(a) and (b) show a dual-coupled nanobeam cavities system in which one of the coupled cavities is fixed and light is launched into and collected from this cavity. The other movable cavity is integrated with a NEMS comb drive that controls the coupling gap. With this mechanism, up to 8 nm red-shift of an even mode and 3.8 nm blue-shift of an odd mode were observed in experiments without significant *Q* factor degradation when the coupling gap was changed from 750 to 150 nm [95]. Compared with the study in Ref [93], the resonance tuning in Ref [95] is purely based on coupling strength variation, without deforming the cavities. To further broaden the resonance tuning range, a triple-coupled nanobeam cavities system was proposed and developed using two on-chip integrated comb drives, where over 24 nm of resonance shift was experimentally demonstrated [96]. It is also interesting to note that in contrast to systems with large wavelength tuning ranges, ultra-precision resonance tuning over a small range has also been reported. For example, to accurately measure the

optomechanical coupling coefficients of a set of dual-coupled 1D PhC nanobeam cavities, a comb drive that is combined with a mechanical displacement shrinkage mechanism is used for ultra-fine control of the coupling gap and correspondingly, the resultant resonance [97].

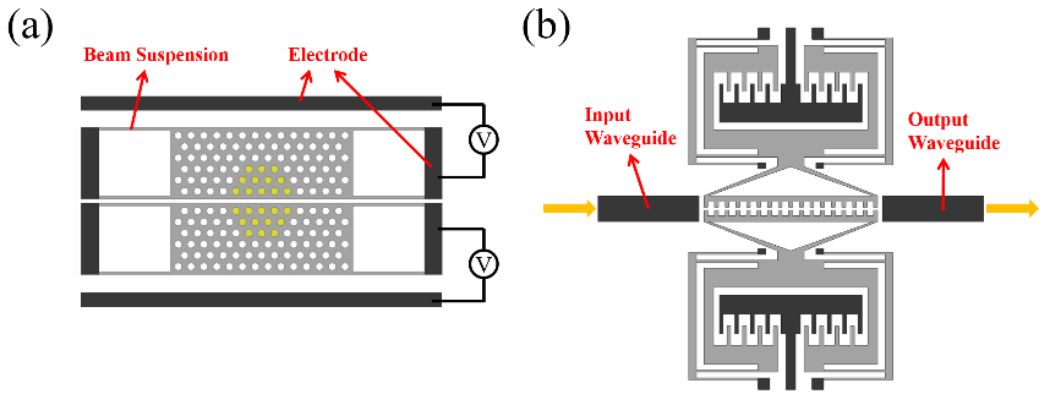

Figure 2.7 (a) Schematic of a tunable air-slot 2D PhC cavity with integrated electrostatic actuators. The yellow holes denote the defect region of the 2D PhC slab. (b) Schematic of a tunable transversely split nanobeam cavity.

Another way to control the cavity resonance is to reconfigure or deform cavities using MEMS/NEMS. For 2D cavities, there is a popular design, which can be referred to as air-slot cavities, having ultra-small mode volumes [98]. As shown in Fig. 2.7(a), an air-slot is inserted in a planar photonic crystal slab and the dimensions of the air holes near the cavity center are adjusted to attain high *Q* factors. As can be seen, the air gap can be electrostatically tuned with the illustrated electrical configuration. In the reported experiments, strong opto-electro-mechanical coupling and resonance shifting were demonstrated [99, 100]. Besides air-slot 2D cavities, reconfigurable or deformable cavities can also be realized with 1D cavities. As shown in Fig. 2.7(b), the ladder-like cavity is transversely split by an air-slot into two symmetric parts, which are both

movable and mechanically controlled by their individual comb drives. The width of the air-slot is controlled by varying the voltage applied to the actuators. In the reported experiments, a resonance shift of up to 17 nm of the second-order mode was detected with an air-slot width increment of 26 nm while the *Q* factor varied only slightly [101]. 1D PhC cavities can also be longitudinally split and mechanically tuned. One can refer to Refs [102-104], while details will not be elaborated. Yet, there is no coupling strength tuning involved in the reconfiguration or deformation of PhC cavities.

As discussed above, on-chip tuning mechanisms for photonic devices using monolithically integrated MEMS/NEMS generally have the merits of simple system configurations and fabrication processes, high precision, good reversibility, dynamic control capability, and low energy consumption. Therefore, the tuning methods have promising applications in future optical communication, sensing and quantum processing systems.

However, among these reviewed works, there are few studies discussing the coupling strength tuning between coupled photonic structures, even though it is one of the strong capabilities of NEMS tuning. The study of the interactions between optical micro/nano resonators, which are strongly coupled to each other through their evanescent fields, is of high impact for both their fundamental physics and potential applications [105-109]. Analogous to chemical molecules formed by coupled atoms, coupled optical micro/nano resonators are also known as photonic molecules [110, 111]. The coupling

strength between resonators (photonic molecules), which characterizes their interaction, is a key parameter [112]. Precise control of coupling strength enables the entanglement generation in quantum-emitter-embedded photonic systems [113], improvement of single photon statistics in single photon devices [114], realization of spontaneous symmetry breaking [115] and Josephson phenomenon [116] in photonic molecules, and many others. However, due to fabrication imperfections, fine control of coupling strength is hard to achieve. Although several methods including laser non-thermal oxidation and water micro-infiltration have been developed for post-fabrication compensation of the coupling strength, they are however irreversible, hard to control and have limited accuracy and tuning ranges [117, 118]. Thus the author proposes to study coupling strength tuning of coupled photonic resonators using NEMS actuators.

2.3. Optical Gradient Force Based on On-chip Photonic Devices

Conventional optical forces are usually generated by free-space light mainly for optical trapping [119] and they have been investigated for decades, while nowadays the study of optical force is focused on the optical gradient force generated by on-chip photonic devices. As discussed, such optical force can be bipolar depending on mode symmetry. For example, as illustrated in Fig. 2.8, when the mode is symmetric, the force is attractive, while if the mode is anti-symmetric, the force can be repulsive.

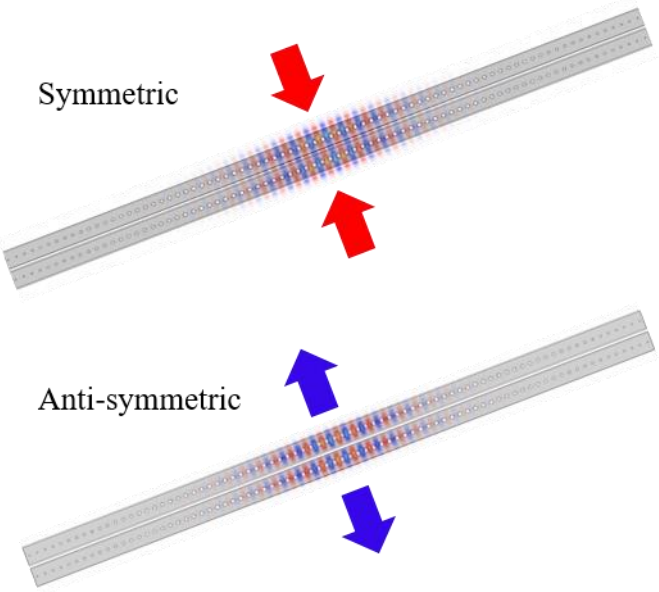

Figure 2.8 Illustration of the optical gradient force direction depending on mode symmetry.

Optical gradient force is theoretically predicted to arise from the overlap between parallel guided waves evanescently coupled together and the force can be attractive or repulsive depending on the mode symmetry of the two guided waves [120]. Models of optical gradient force between coupled waveguides have been established [121] and many numerical studies have been reported to predict optical force generated by diverse kinds of photonic configurations, including coupled planar waveguides [122], waveguide and coupled substrate [123], coupled WGM resonators [124] and coupled 2D PhC cavities [125]. Generally, the optical force generated by optical resonators has a higher magnitude than that arising from non-resonant structures because the light energy is resonantly enhanced in resonators.

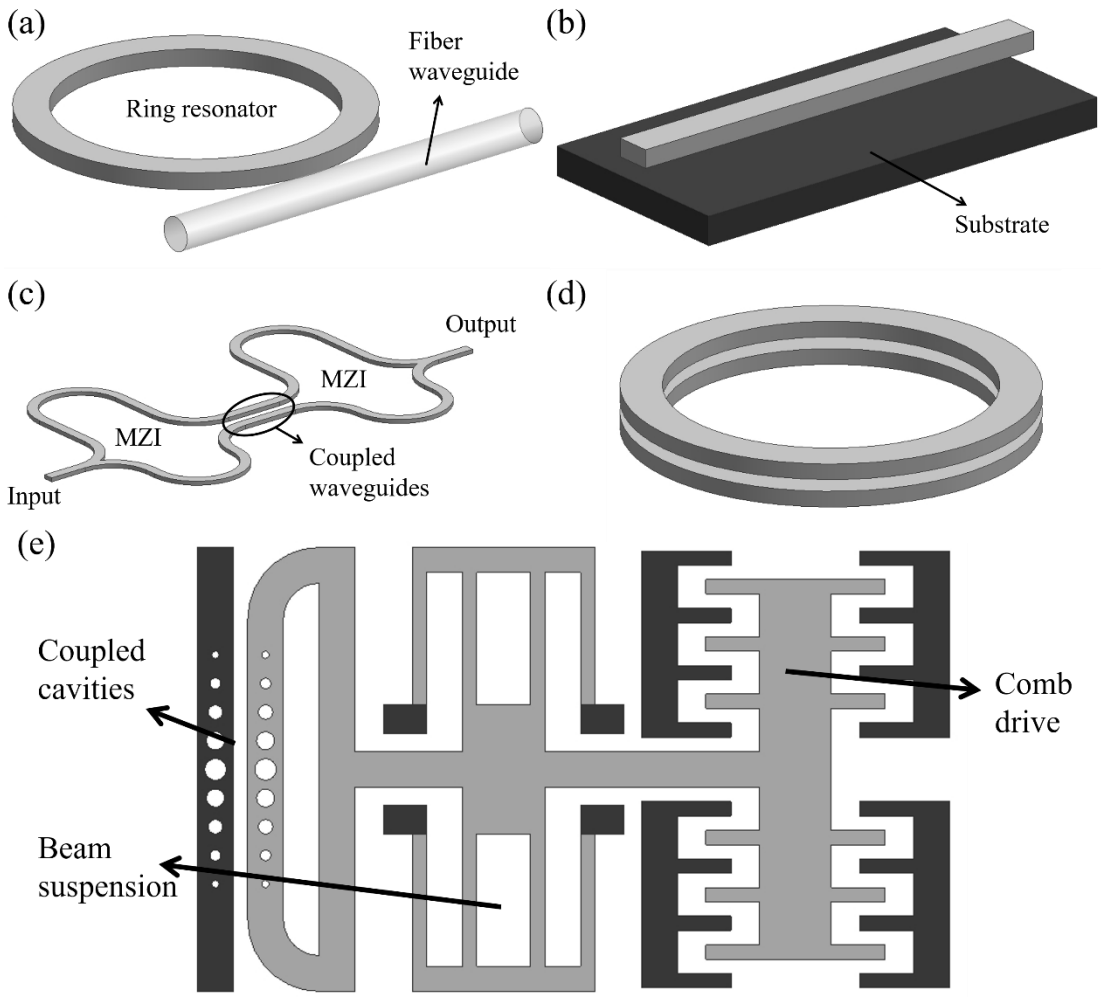

Figure 2.9 Schematics of photonic configurations, (a) ring resonator coupled with tapered-fiber waveguide, (b) waveguide coupled with its dielectric substrate, (c) coupled waveguides with MZIs, (d) vertically coupled WGM resonators, and (e) NEMS comb drive controlled coupled PhC nanobeam cavities.

With the development of nano fabrication and testing techniques, experimental studies of on-chip optical gradient force have been widely reported. Such a force is demonstrated to arise from a ring resonator and a coupled tapered-fiber based waveguide (the configuration is illustrated in Fig. 2.9(a)) in 2007 [126], and nearly one micrometer displacement of the waveguide was observed in experiments. Actually, in the reported study, the device cannot be regarded to be totally on-chip. As for totally on-chip optical gradient force studies, the configuration of a waveguide coupled with

its dielectric substrate was investigated in 2008 for optical gradient force [127]. As illustrated in Fig. 2.9(b), the waveguide is suspended over the substrate. The force is generated between waveguide and the substrate and is detected by monitoring the evanescent coupling of the guided wave to the substrate. In this study, the nano mechanical device is driven in the dynamic mode and a strong spring softening effect was observed, indicating a relatively large magnitude of the force. A limitation in this study is that the mode symmetry and thus the force direction cannot be manipulated. In another configuration based on coupled waveguides, the input light is manipulated by a monolithically integrated Mach–Zehnder interferometer (MZI) as illustrated by Fig. 2.9(c) [24]. The input light is split and launched into the two MZI arms with different lengths, which could induce a phase difference before the coupled waveguides. By changing the input wavelength and thus the difference of effective light path length in the two MZI arms, the phase difference can be controlled. In this way, the mode symmetry in the coupled waveguides can be manipulated. The output light from the coupled waveguides is also tuned by another MZI based on the same mechanism to enhance displacement detection sensitivity by examining the output phase information. In experiments, switching between attractive and repulsive force by varying the input wavelength was demonstrated and mechanical oscillation excited by optical force was achieved. A very similar study is reported in Ref [25]. Generally the optical gradient force generated by non-resonant structures will have a relatively low magnitude. To address this issue, Cai *et al* designed and fabricated a device based coupled PhC

waveguides [128]. The PhC waveguides have relatively low group velocity of their guided waves and thus the optical force generated can be enhanced. The experimentally detected optical force in this study is estimated to be as high as 1.01 pN/μm/mW (force magnitude over unit waveguide length and pumping power).

Other configurations like coupled optical resonators have also been investigated. In the study of Ref [129], vertically coupled WGM resonators (see the schematic in Fig. 2.9(d)) were investigated as an all-optical wavelength router driven by optical gradient force. In experiments, both static and dynamic working modes were realized. Besides, in a large-scale vertically coupled WGM resonators system, an optical force-induced mechanical deformation of as large as 20 nm was realized with input power of only 3 mW [130]. Coupled PhC nanobeam cavities have also been investigated to study the optical gradient force. In the report of Ref [131], the device is based on NEMS-controlled coupled nanobeam cavities as illustrated in Fig. 2.9(e). As shown, one of the cavities is fixed and light is launched into and collected from this cavity, while the other cavity is a movable cavity integrated with NEMS comb drive and supported by spring suspensions, and thus the coupling gap between cavities can be manipulated by applying voltage to the comb drive. The force is measured in static mode through monitoring the mode resonance wavelength shifting. In experiments, an estimated attractive force of 6.2 nN when pumping on an even mode and an estimated repulsive force of 1.9 nN when pumping on an odd mode with less than 1mW incident laser power were demonstrated. This study indicates a very high energy efficiency of the optical

gradient force.

However, among the reviewed studies of optical gradient force, especially the force generated by coupled PhC nanobeam cavities, there is no report of optical gradient force in the lateral direction (along the cavity beam). As mentioned, to better understand the optical gradient force generated by on-chip photonic devices and develop all-optical controlled system based on it, it is important to fully study all kinds of optical gradient force. Due to the absence of the study on lateral shearing optical gradient force, a study concerning such force was carried out by the author and this is described in Chapter 5.

2.4. On-chip Cavity Optomechanics

Besides statically deforming nano structures, the optical force can also interact with mechanical vibration, resulting in many interesting phenomena. The optical spring effect has been theoretically predicted for years [132, 133] and has been demonstrated in experiments [134-136], in which the optical mode and mechanical deformation interact with each other. More specially, the effect will result in mechanical resonance frequency shift, depending on the optical pumping frequency detuning. Furthermore, it was found that the optical pumping could dramatically enhance or suppress the mechanical oscillation, i.e., mechanical amplification or cooling [26, 137-142]. Now it is being extensively investigated as cavity optomechanics. Earlier studies of optomechanics are based on the type of optical force of radiation pressure (for example, the study in Ref [143]). Nowadays, both radiation pressure and optical gradient force

are investigated for cavity optomechanics in on-chip photonic devices.

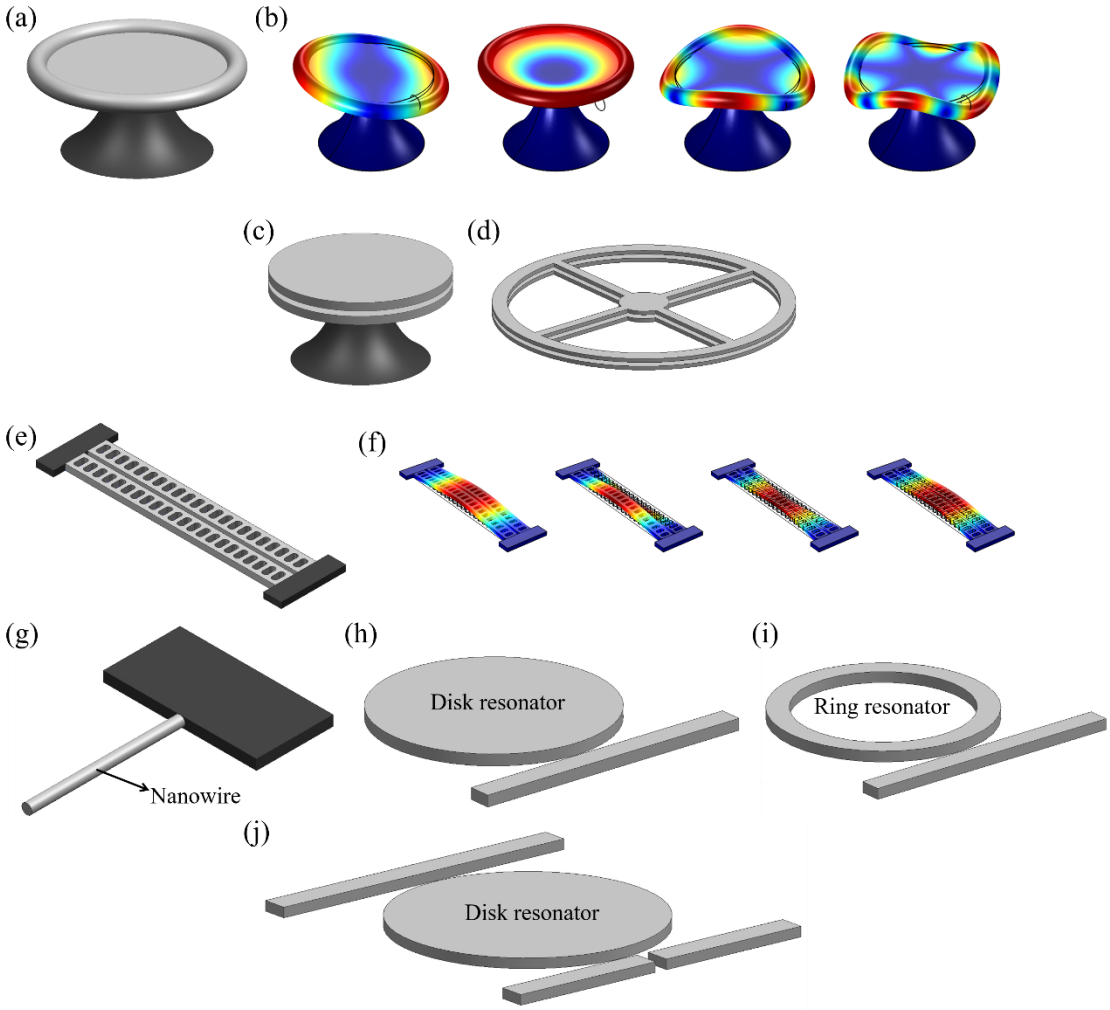

Figure 2.10 Schematics of photonic structures of (a) toroid resonator, (c) vertically coupled disk resonators, (d) vertically coupled wheel-shape ring resonators, (e) coupled nanobeam zipper cavities, (g) nanowire (h) disk resonator coupled with a waveguide, (i) ring resonator coupled with a waveguide, and (j) disk resonator coupled with multi-channel waveguides, one of which is segmented. Typical mechanical resonance mode shapes of (b) toroid resonator and (f) coupled zipper cavities.

One of the classic photonic structures used to investigate optomechanics is the toroid resonator as illustrated in Fig. 2.10(a). Some typical mechanical resonance mode shapes of the toroid resonator are illustrated in Fig. 2.10(b). In the study of Ref [144], a nano toroid resonator was optomechanically excited and mechanical resonance with *Q* factor

reaching 1×10^5 was achieved. In experiments, both mechanical amplification and cooling were observed, and the study showed a potential displacement detection with sensitivity of sub-fm/$Hz^{1/2}$. Such optomechanical systems based on toroid resonators were also investigated for mass sensing [145] and magnetic field detection [146]. The study in Ref [147] investigated the mechanical normal mode coupling in a micromechanical system to understand the physics of mechanical dissipation and it revealed the potential of cavity optomechanics to break the limitation to the mechanical *Q* factors due to mechanical damping induced by material loss. Such cavity optomechanics can also induce a transparency effect [148, 149], providing new tools for light propagation controlling, for example on-chip slowing and storage of light.

Photonic configuration of vertically coupled disk resonators (see Fig. 2.10(c)) was also studied for optomechanics [150] and this cited study revealed that the optical gradient force may have higher optomechanical driving capability than radiation pressure in a coupled disk resonators system. In another study based on vertically coupled disk resonators, it indicated that the optomechanical coupling can be used to reduce and even eliminate the anchor loss of a mechanical resonator through the destructive interference of the elastic waves [151]. A similar design of vertically coupled wheel-shape micro-ring resonators (see Fig. 2.10(d)) was also studied for broad band tuning [152].

Coupled PhC nanobeam cavities are another typical photonic structures for cavity optomechanics. Eichenfield *et al* designed and fabricated coupled zipper cavities, the

configuration of which is given in Fig. 2.10(e) with typical mechanical resonance mode shapes illustrated in Fig. 2.10(f) [153]. Large per-photon optical gradient force was realized. Due to the large force and the minimized structure mass, the structure mechanical rigidity is determined to a great extent by the optical mode. There are also theoretical studies of cavity optomechanics based on coupled zipper cavities [154, 155] and a vertically coupled 2D PhC cavities system has been theoretically investigated as well [156]. Besides coupled PhC cavities, optomechanics has also been demonstrated on single deformable or reconfigurable 1D [157-159] and 2D [160-163] PhC cavities. In the study of Ref [159], optical signals in a 1.5 MHz bandwidth were tuned over a frequency span of 11.2 THz via cavity optomechanics; in the study of Ref [160], an estimated optomechanical coupling rate of 320 kHz was achieved.

Optomechanics can even be achieved in a silicon nanowire structure, as illustrated in Fig. 2.10(g). For example, a study demonstrated cooling of silicon nanowires mechanical vibration to 30-40 K from room temperature, indicating great potential in zeptogram-scale mass detection [164]. Remarkably, this study shows that though the mechanical structure's dimensions are much below that of the light wavelength of light, the optomechanical coupling remains very strong. Simple structure like a micro-pillar has also been demonstrated with optomechanical coupling [165].

Photonic configurations consisting disks or rings should not be ignored. Cavity optomechanics based on the classical systems of disk or ring coupled with a waveguide

(see Figs. 2.10(h) and (i)) has also been reported. In the study of Ref [166], the nonlinear behavior of an optomechanically excited nanostructure was observed based on a ring-bus waveguide coupled system. In another study, force sensing with spectral density of 15 aN/Hz$^{1/2}$ was achieved based on an optomechanical disk-waveguide coupled system [167]. A more complicated system consisting of a disk coupled with multi-channel waveguides, one of which is segmented, was investigated for radio frequency signal amplification [168]. As illustrated by the schematic in Fig. 2.10(j), the disconnected waveguide is driven out-of-plane via optomechanics, resulting in optical signal modulation.

To sum up, with the ability to measure nanomechanical oscillation beyond the quantum-limit [138, 169, 170], currently cavity optomechanics is widely studied for sensing applications with ultra-high resolution [144] and even for investigation of gravitational waves [171]. It is believed to have potential in both fundamental physics and innovative technologies. Another key achievement of optomechanics is its demonstrated capability to maintain high mechanical Q factors for an optomechanical resonator oscillating in heavy loss condition, like in liquids [172, 173]. This achievement indicates a promising future for the application of optomechanics to biological and biomedicine sensing [174].

For better control and measurement of mechanical motion using cavity optomechanics, it is important to develop tuning methods for the cavity optomechanics, which is scarcely reported in the literature, probably because no effective method to reconfigure

the optomechanical device has been tried. Yet, as discussed in Section 2.2, NEMS tuning could serve as a strong tool to adjust the optomechanical devices to achieve tunable cavity optomechanics. This tuning method proposed in this thesis is described in Chapter 6.

Chapter 3. Nano Fabrication Process and Experimental Testing Setup

In this chapter, experimental methodologies used in this thesis study will be introduced. The development of nano fabrication process for the proposed photonic devices is a key component of the study in this thesis and it will be discussed in Section 3.1. In addition, the testing setup and equipment are introduced in the following section.

3.1. Nano Fabrication Process

3.1.1. Introduction to micro and nano fabrication techniques

Standard micro fabrication processes have been established for released MEMS microstructures and they generally can be categorized as bulk micromachining or surface micromachining. Bulk micromachining forms structures by selectively etching inside the material substrate, in which case anisotropic etching is commonly used. Unlike bulk micromachining, surface micromachining builds structures by depositing and etching of different layers on top of the substrate. Bulk micromachined devices are space-consuming and are usually limited to anisotropic materials. By comparison, surface micromachining permits flexibility in materials selection and enable high-resolution patterns and thus is widely used for the fabrication of MEMS/NEMS devices and photonic circuits.

Traditional photolithography is a common method to define the patterns in micro fabrication and has a resolution in the micron- and submicron-scale. Improved methods, including electron beam lithography (EBL), focused ion beam (FIB), optical projection lithography, extreme UV lithography and X-ray lithography [175], are frequently used for nano patterning processes. Among them, EBL and FIB have an ultra-high resolution of several nanometers. No physical mask is required and patterns are formed by scanning a focused electron/ion beam dot by dot. Thus, they are flexible but time-consuming processes and are used extensively for fabricating nano-scale photonic structures such as photonic crystals and plasmonic nano dots. FIB even combines lithography and etching together to form the structures, while there is no etching involved in EBL. After defining the pattern, such as by EBL, material etching and deposition are utilized to form the structures. The most commonly-used etching methods are ion milling [176] and reactive ion etching (RIE) [177]. Whilst ion milling is advantageous in the precise etching/patterning of materials like metals, it can cause crystal damage, induced by ion impact, when etching single crystal materials [178]. Conventional RIE usually cannot achieve high aspect ratios and near-vertical sidewalls. Thus, the Deep-RIE technique has been developed [179] and widely used in nano fabrication, especially of single crystal materials like single crystal silicon [180].

As for deposition, there are diverse techniques of chemical [181] and physical [182, 183] vapor deposition and sputtering [184] of metallic and various kinds of dielectric materials. Last but not the least, chemical etching of sacrificial layers is always required

to form suspended structures for mechanical tuning. Hydrofluoric (HF) acid etching of silicon dioxide (SiO_2) is a common final fabrication process step to release and functionalize MEMS/NEMS devices. It is usually done using the HF vapor, instead of the liquid phase to avoid adhesion/stiction of nano structures arising from liquid surface tension [185].

3.1.2. Flow of the developed nano fabrication process

As for the nano fabrication used in this thesis, it is conducted by the procedure described below. The devices are fabricated on 4' silicon-on-insulator (SOI) wafers, with top single crystal silicon device layer of 260 nm, lightly p-type doped, while the total wafer thickness is 675 ±15 μm. The top layer silicon has an electrical resistivity ranging from 13.5 to 22.5 Ohm-cm and the crystal orientation is (100). The key structures are built first before other accessorial electrical functional structures. Before starting, the wafer is cleaned with acetone and isopropyl alcohol (IPA) and flushed with distilled water (DI water). The wafer is coated with EBL resist ZEP520, which is positive resist, with a highest spinning speed of 3000 rpm/s, resulting in a resist thickness of about 250 nm. Then patterns of suspended structures such as PhC cavities, NEMS actuators (comb drive actuators as shown in Fig. 3.1) and suspensions are defined with EBL. Before exposure, the wafer is pre-baked for two minutes with a temperature of 180℃.The structures are formed by DRIE and the etching is stopped on the box silicon dioxide layer. After etching and removing the residual EBL resist the structure of a single device

is realized as illustrated in Fig. 3.1.

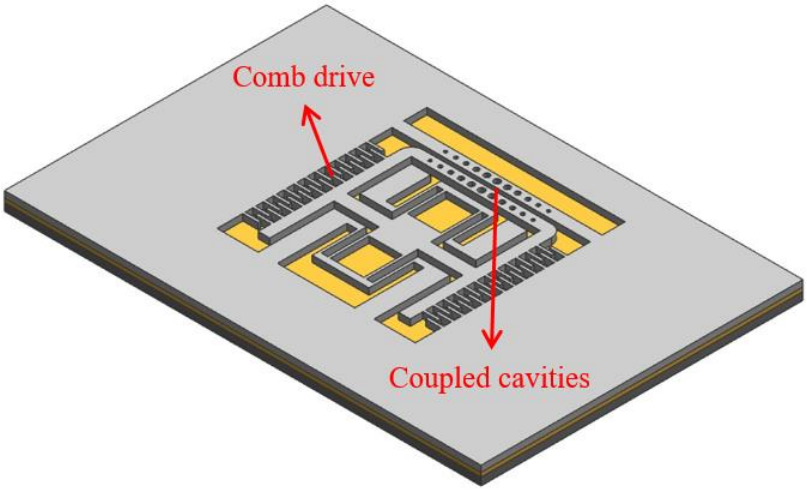

Figure 3.1 Illustration of the structure after forming the suspended structures by DRIE etching, and removing the residual EBL resist. The light and dark gray layers denote the top silicon device layer and the silicon substrate respectively, while the yellow layer denotes the SiO_2 box layer.

After removing the residual resist, the wafer is cleaned and coated with another layer of EBL resist and the grating couplers and tapered rib waveguide are patterned again by EBL. These structures are formed by DRIE with an etching depth of 80 nm. After etching, the residual resist is removed again with Micro-remover 1165. The structure of a single device is illustrated in Fig. 3.2.

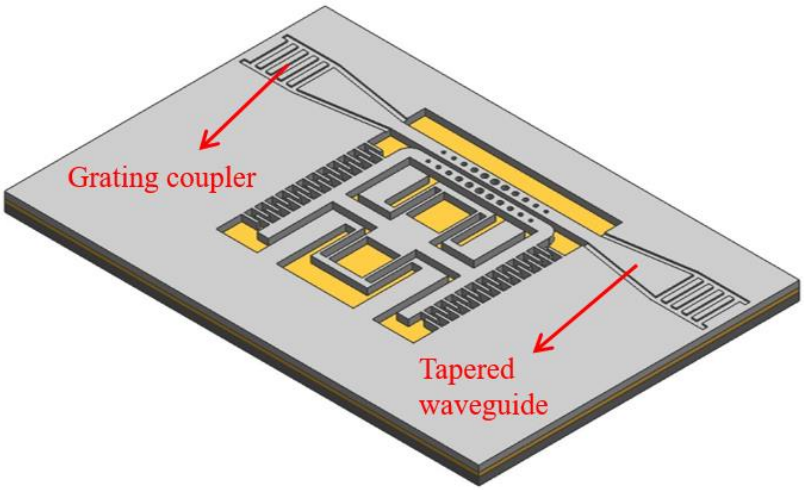

Figure 3.2 Illustration of the structure after forming the grating couplers and tapered rib waveguide by DRIE etching, and removing the residual EBL resist.

Subsequently, the wafer is carefully cleaned and treated by HMDS oven, followed by coating with positive photon-resist AZ5214E (or AZ9260), which is positive resist. Before exposure, the wafer is pre-baked for 1.5 minutes (for AZ5214E or 10 minutes for AZ9260) with a temperature of 90℃. Then the structures of isolation trenches are patterned by traditional photolithography and formed by RIE or DRIE etching through the device layer. After removing the residual photon-resist with resist stripper (or with acetone and IPA), the structure is obtained as illustrated in Fig. 3.3.

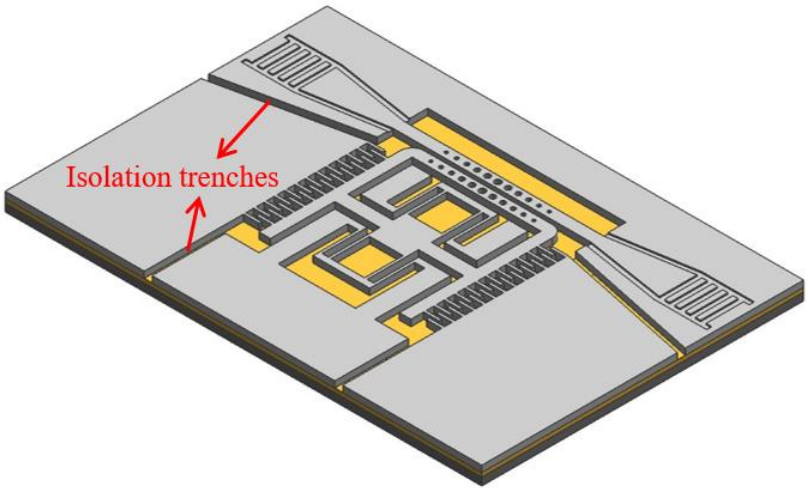

Figure 3.3 Illustration of the structure after forming the isolation trenches by DRIE or RIE etching, and removing the residual photon-resist.

The wafer is then cleaned and coated with AZ9260. Another photolithography step is conducted to pattern the gold electrodes, which are formed by metal deposition with electron beam evaporator and a lift-off process. The structure is illustrated in Fig. 3.4. In the lift-off process, after gold deposition, the wafer is immersed in acetone for over three hours. Then the wafer (whilst still immersed in acetone) is treated with ultrasonic waves for five minutes, after which the gold patterns are formed.

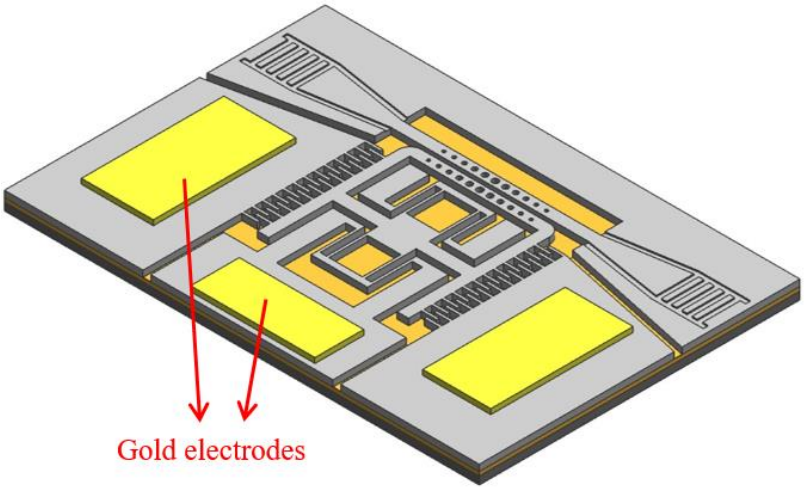

Figure 3.4 Illustration of the structure after forming the gold and electrodes by electron beam evaporator metal deposition and a lift-off process.

The last step is to release the suspended structure from the substrate using HF vapor. Before release, the wafer is diced into small chips, which makes them easier for release, device packaging and testing. A single device after the entire fabrication process is illustrated in Fig. 3.5.

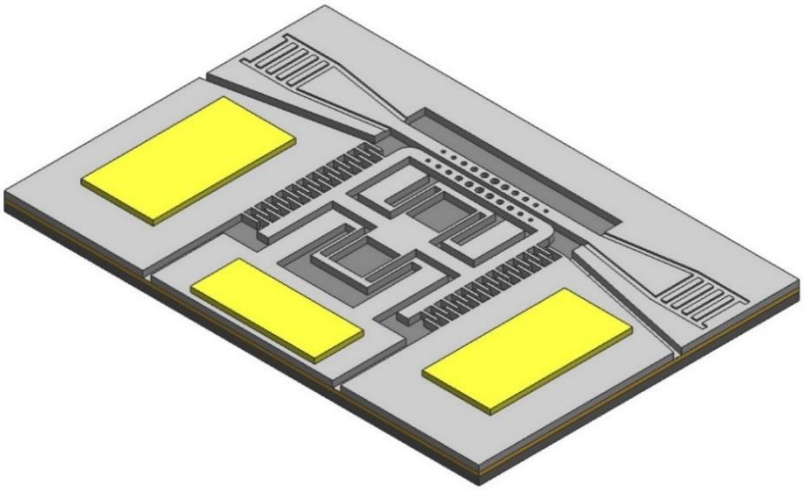

Figure 3.5 Illustration of a completely fabricated device.

The entire fabrication process is summarized in Fig 3.6.

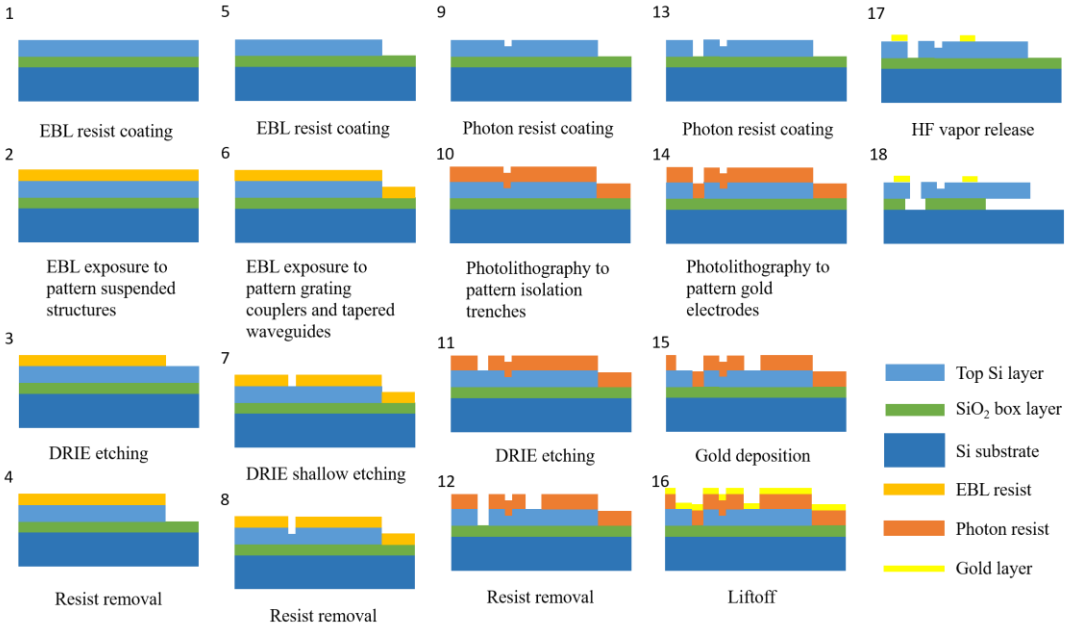

Figure 3.6 Flow chart of the fabrication process.

In the HF vapor release process, the sample chips after dicing, as shown in Fig. 3.7(a), are placed at and cover the through-holes on the sample holder, face down (the holder is shown in Fig. 3.7(b)). Then the holder is placed on a Teflon beaker containing moderate amount of HF solution (49% HF, 1:1 diluted). The entire setup is shown in Fig. 3.7(c) and as can be seen, the sample chips are heated with an osram lamp and the temperature is controlled by adjusting the distance between the lamp bulb and the sample chips. The entire setup is placed in a fume hood for safety reasons and the release process roughly takes about 8 hours.

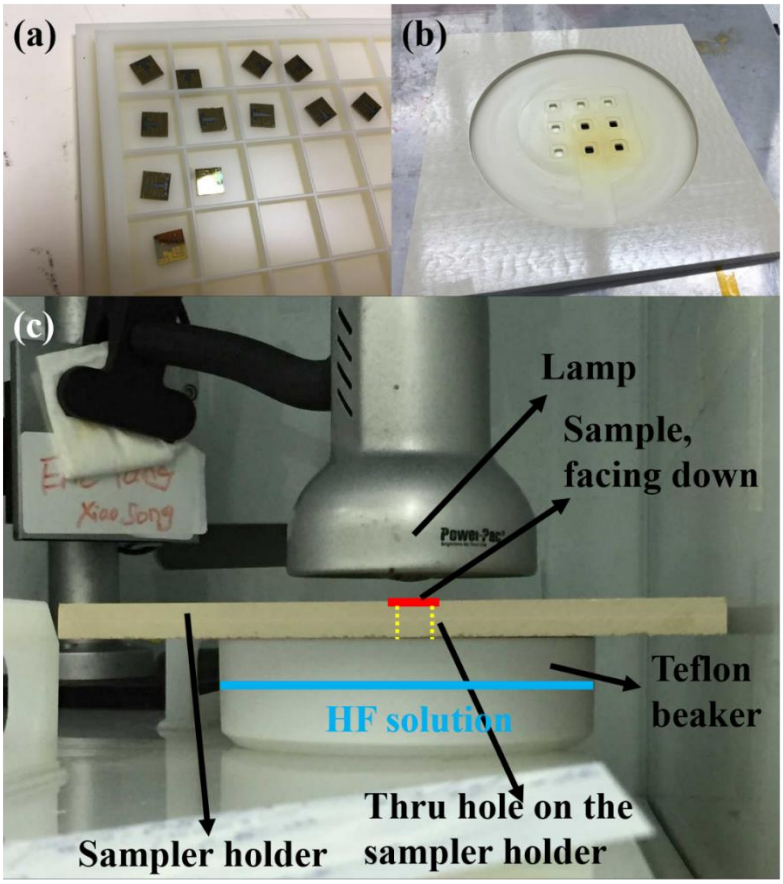

Figure 3.7 Pictures of (a) sample chips after dicing for release, (b) sample holder used in HF vapor release and (c) release setup.

3.1.3. Results and discussion

Figure 3.8 shows SEM images of some successfully fabricated devices. As can be seen, the device is suspended after HF vapor undercuts the structure. The triangular holes on the bulk serve as etching windows during the release. The period of production is about three weeks and nearly one hundred of such devices can be fabricated in one fabrication cycle with a yield about 50%.

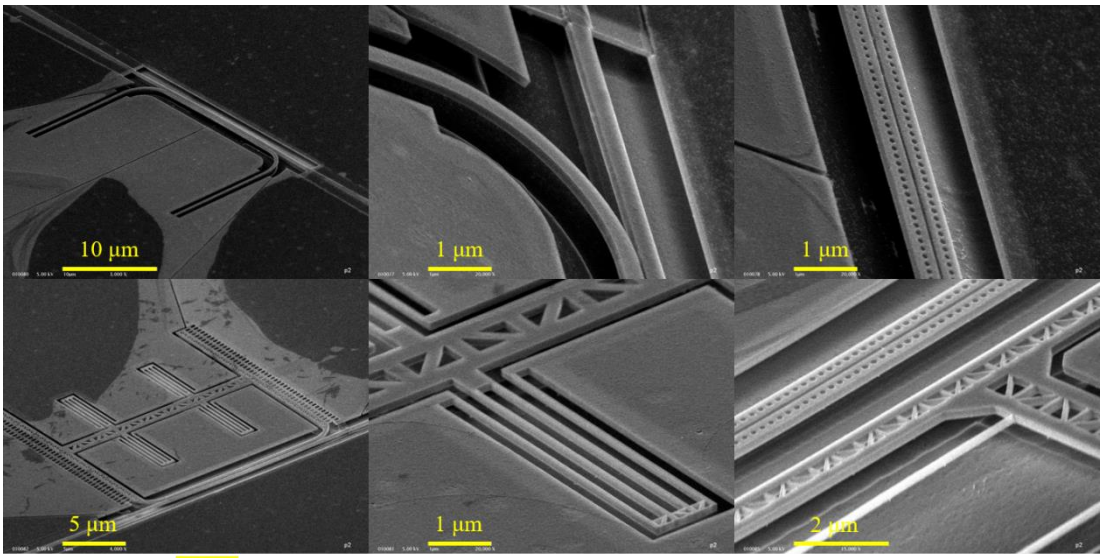

Figure 3.8 SEM images of successfully fabricated devices.

The key and most difficult steps are nano etching (with DRIE) and HF vapor release. Except for the grating couplers and tapered rib waveguides, the suspended parts of the device have to be fully etched. Yet it is quite difficult to guarantee success because the etch rate of the DRIE is not stable. SEM can be used to check whether the device is fully etched but SEM characterization is only accessible after the wafer is diced into small chips, when it is too late to remedy the situations. Figure 3.9 shows an example of a failed device. As can be seen, there are still silicon materials left in the rectangular holes and at the corners. These residual materials would definitely make the device non-functional. To solve this problem, careful calibration of the etch rate every time before etching real samples is necessary.

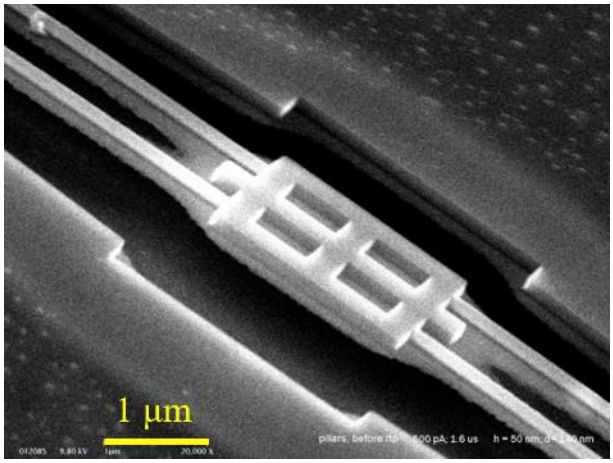

Figure 3.9 SEM image of a failed device due to being un-fully etched.

HF vapor release is another difficult process. The key in this process is temperature control. HF release is a chemical process and liquid phase water is involved and necessary in this reaction. The amount of water condensed on the chip surface depends on the temperature and partial pressure of water vapor in the environment. Yet only the temperature can be controlled. The chemical etching rate is proportional to the amount of liquid water condensed. If the temperature is too low, the amount of liquid water would exceed a critical value, in which case the structure will stick to the substrate due to liquid surface tension, as shown in Fig. 3.10.

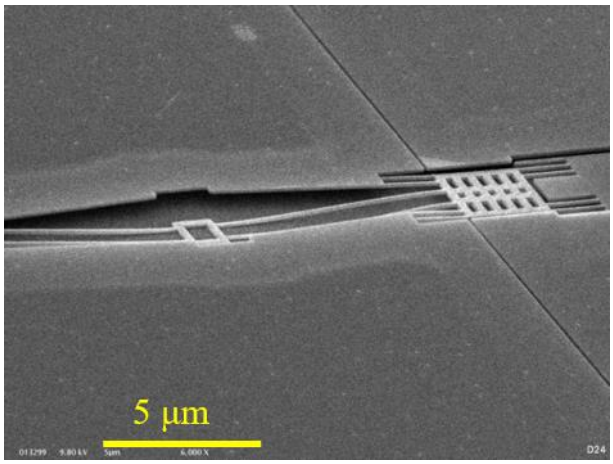

Figure 3.10 SEM image of a failed device due to stiction to the substrate.

HF release requires much experience and Fig. 3.11 shows an example of a successfully released device with similar structure configuration. The long thin beam is of about 20 μm in length, 180 nm in width and 260 nm in thickness.

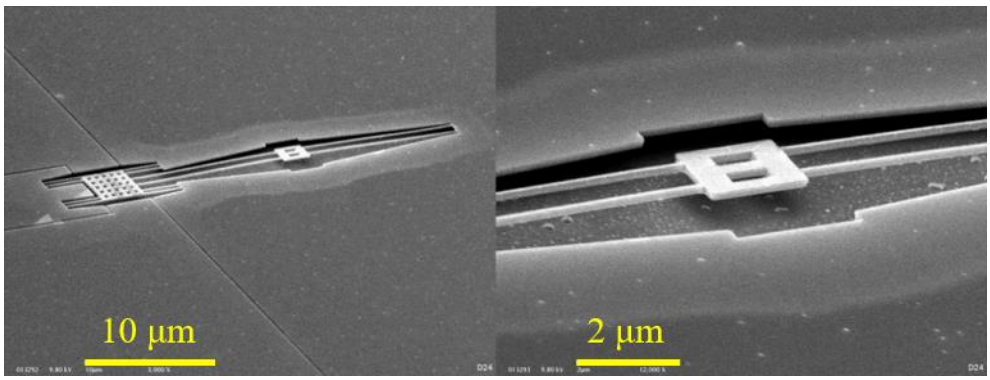

Figure 3.11 SEM images of successfully released structures with long thin beams.

Besides the sticking to the substrate, long thin beams without support and placed closed to each other will also stick together. The sticking together may happen at the initial stage of the release, as shown in Fig. 3.12.

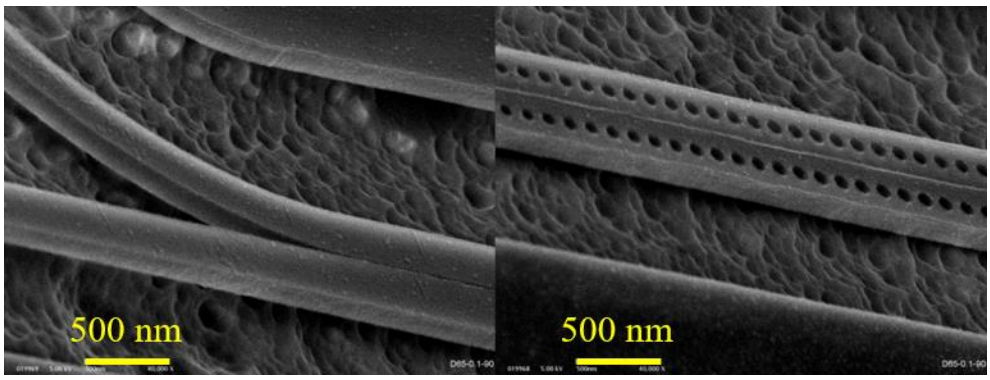

Figure 3.12 SEM images of a failed device due to stiction between long thin beams.

The structure shown in the above figures is the coupled cavities, which is a key structure of the devices studied in this thesis. With careful temperature control, release of this kind of structures can be achieved and Fig. 3.13 shows a successful example.

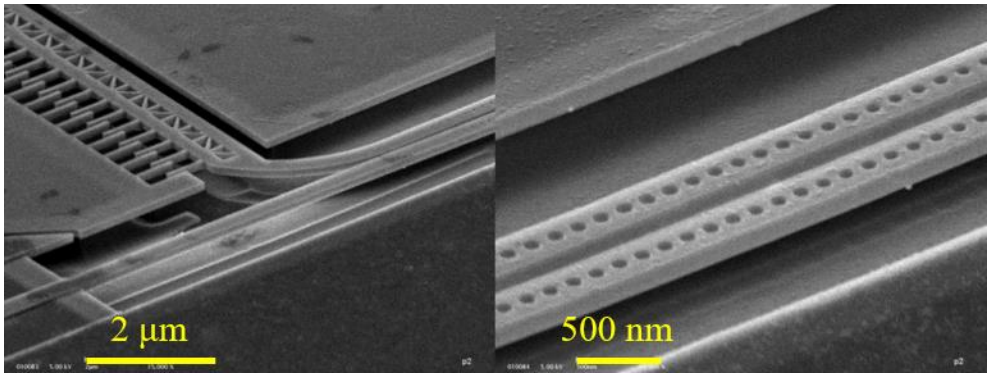

Figure 3.13 SEM images of a successfully released coupled cavities structure.

3.2. Testing Setup

As introduced, the devices investigated in this thesis will be optically characterized with electrical tuning. Thus the devices should be tested as generally illustrated by the schematic in Fig. 3.14.

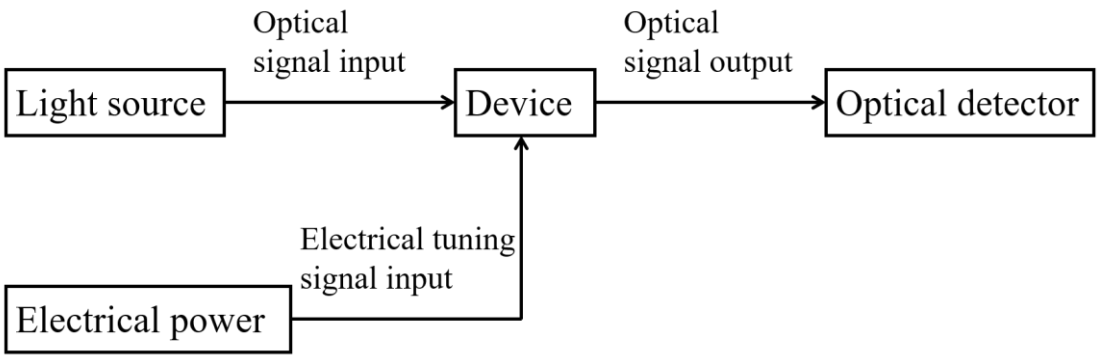

Figure 3.14 Schematic of the general testing setup configuration.

3.2.1. Electrical configuration

The devices studied in this thesis all require electrostatic tuning, and thus they have to be electrically functionalized.

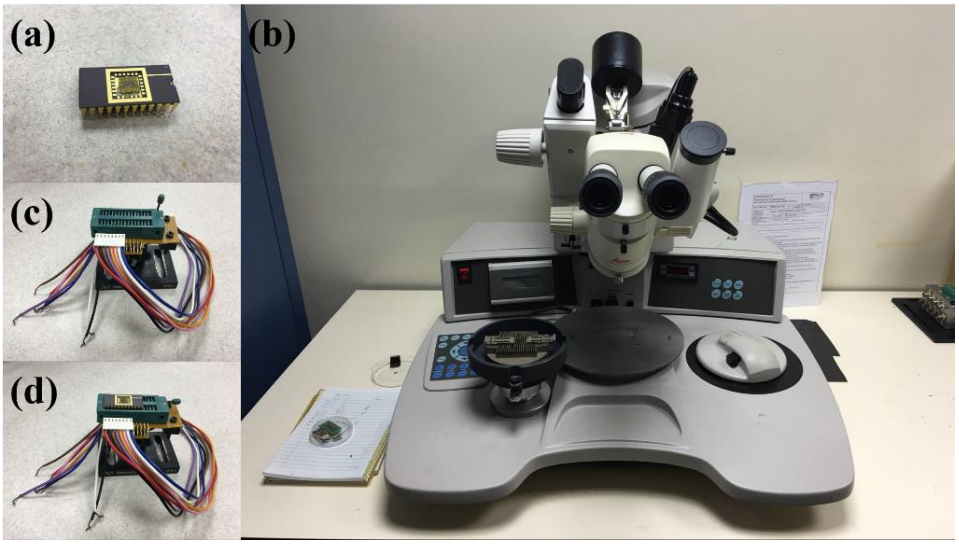

Figure 3.15 Pictures of (a) sample chip packaged with DIP, (b) wire bonder, (c) home-made socket stage with electrical connections, and (d) DIP assembled on the socket.

Firstly, the sample chip is packaged with a dual in-line package (DIP) as shown in Fig. 3.15(a). Then the on-chip gold electrodes are connected with the package pins through wire bonding with the wire bonder (KNS 4523A Digital) shown in Fig. 3.15(b). A home-made socket stage with electrical connections (see Fig. 3.15(c)) is used to hold the package and after assembling the setup is shown in Fig. 3.15(d). Thus, the electrical signal can be applied to the on-chip device.

3.2.2. Optical configuration

As mentioned in Section 3.1.2, the devices are on-chip integrated with grating couplers. The light signal will be launched into or out from the device through the coupling between the grating coupler and a single- or multi-mode fiber, the configuration of which is illustrated in Fig. 3.16. As shown, the fiber is pointed to the grating coupler with a 10 degree offset against the vertical plane. The SEM image of the grating coupler

is shown in Fig. 3.17(a), which has an area of about 12 μm ×12 μm. The grating coupler is connected with a rib waveguide, the width of which is tapered from 12 μm to 700 nm. The tapered rib waveguide is connected with the suspended feeding waveguide at either side of the PhC cavity; Fig. 3.17(b) presents a SEM image of the connection of the rib waveguide and the feeding waveguide.

Light from the laser source is coupled to the single-mode fiber and then to the on-chip device by the grating coupler. The light is then guided by the tapered rib waveguide to the suspended feeding waveguide and subsequently launched into the cavities. The transmitted light from the cavities is then guided by similar waveguide structures and coupled out from the sample chip through another identical grating coupler to the multi-mode fiber and finally collected by detectors.

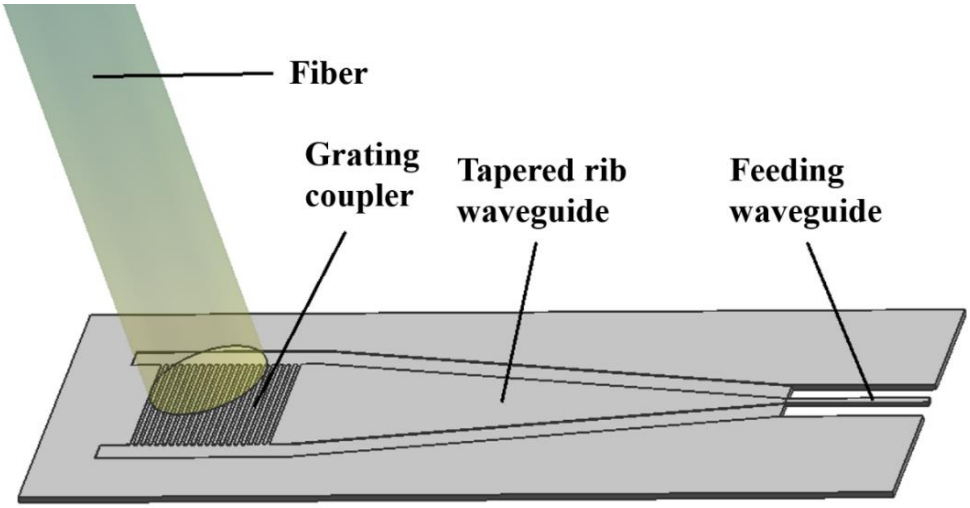

Figure 3.16 Configuration of the coupling between fiber and grating coupler and the connection between grating coupler, tapered rib waveguide and suspended feeding waveguide.

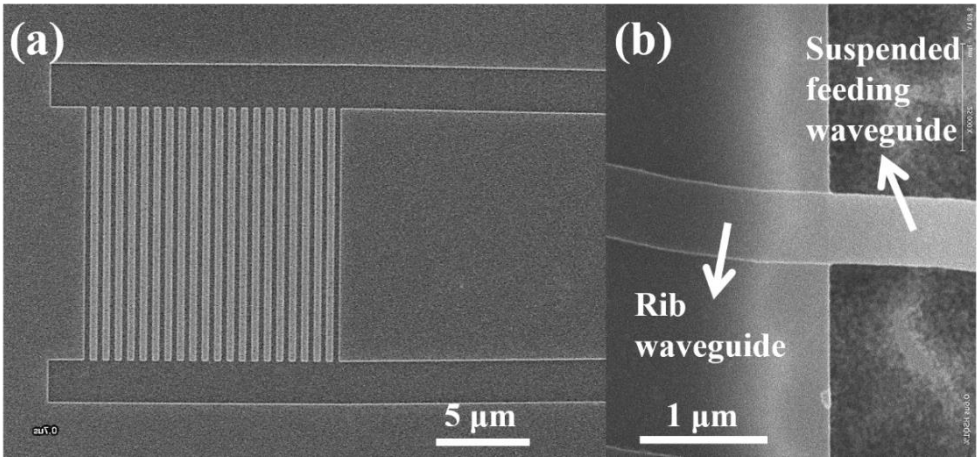

Figure 3.17 SEM images of (a) the grating coupler and (b) the connection between the tapered rib waveguide and the suspended feeding waveguide.

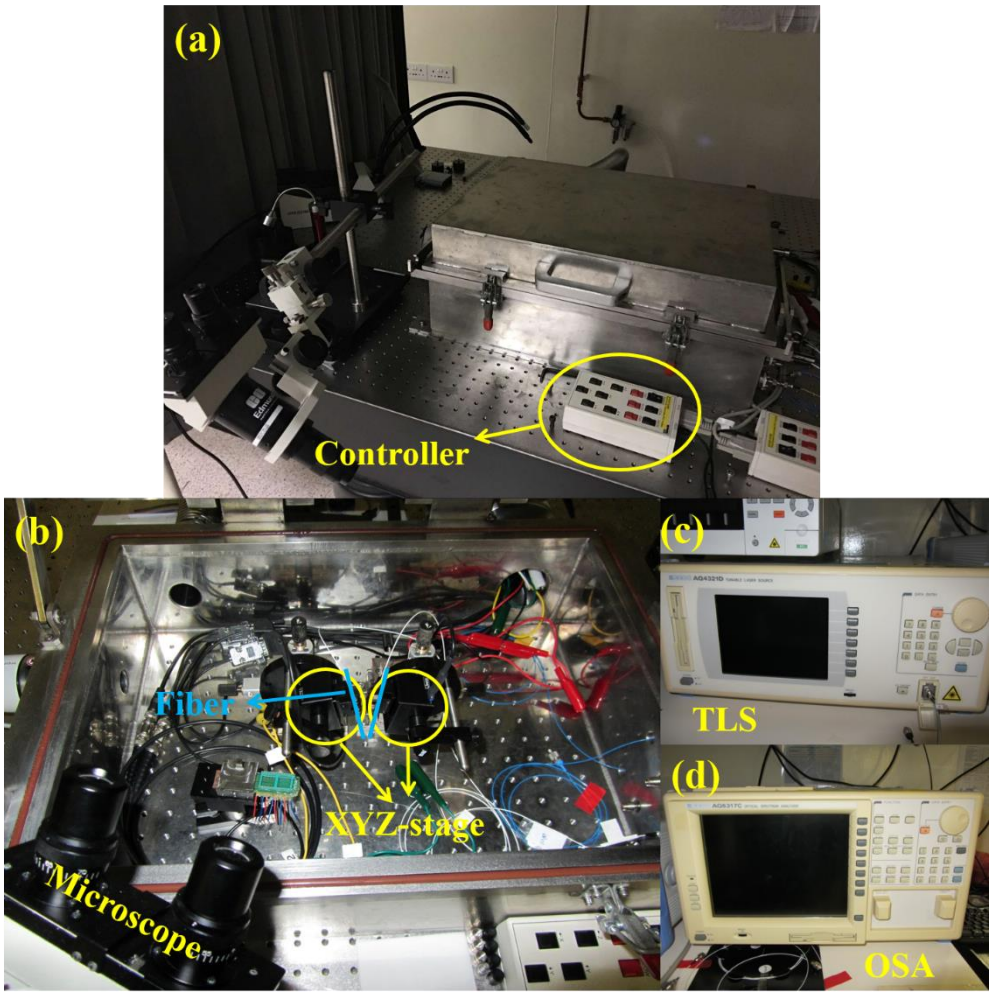

Figure 3.18 Pictures of (a) vacuum chamber (closed) on an optical table with vibration isolators, (b) fiber alignment platform in the vacuum chamber (c) main TLS, and (d) OSA.

The fiber alignment platform is located in a vacuum chamber placed on an optical table with vibration isolators as shown in Figs. 18(a) and (b). As can be seen, the single-mode and multi-mode fibers are fixed on two piezo-actuated XYZ-stages separately and the stages are controlled with their individual controller outside the chamber, the white box at the right bottom of Figs. 3.18(a) and (b). There is also a multi-degree optical microscope (at the left bottom of the figures) for the alignment.

Figures 3.18(c) and (d) show the main tunable laser source (TLS) (AQ4321D from ANDO, with a wavelength range of from 1520 nm to 1620 nm) and the optical spectrum analyzer (OSA) (6317C from ANDO), which can be synchronized together for wavelength scanning and they are the key equipment to characterize the optical properties of the device. Other testing equipment are given in Figs. 3.19(a-h); they are DC power supply (E3631A from Agilent), network analyzer (4395A from Agilent), another TLS (TLS-510 from Sentac, with a wavelength range of from 1500 nm to 1630 nm), erbium doped fiber amplifier (EDFA), high speed oscilloscope (DSO90404A from Agilent), dynamic signal analyzer (N9020A from Agilent), function generator (33220A from Agilent) and InGaAs photodetector (1592NF from Newport), the use of which will be elaborated upon in the following chapters.

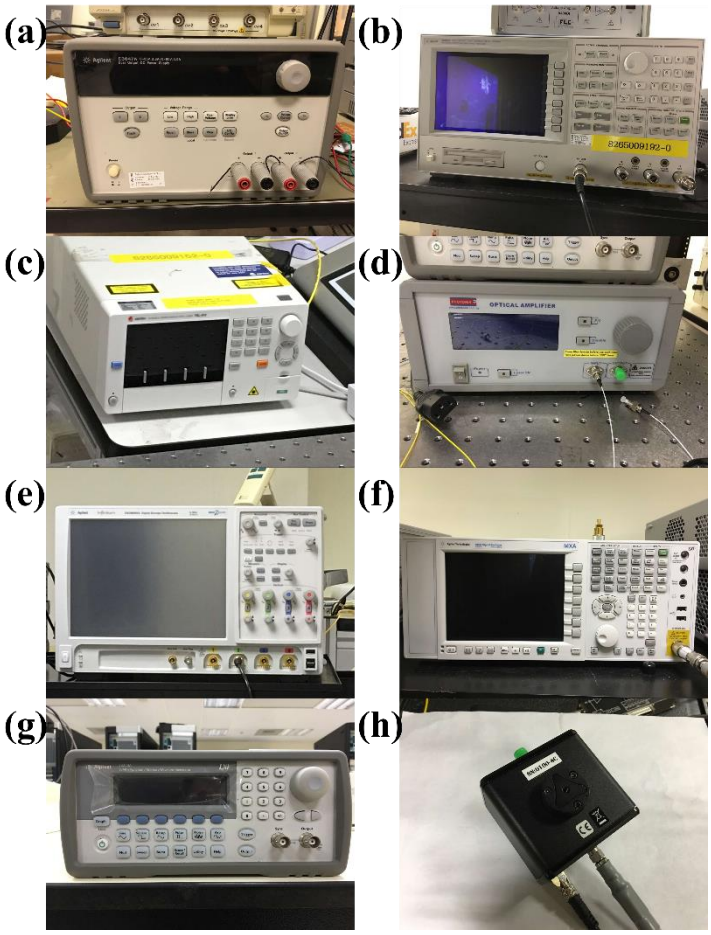

Figure 3.19 Pictures of (a) DC power supply, (b) network analyzer, (c) TLS, (d) EDFA, (e) oscilloscope, (f) dynamic signal analyzer, (g) function generator, and (h) InGaAs photodetector.

Chapter 4. Lateral Tuning of Dual-coupled Photonic Crystal Nanobeam Cavities

In this chapter, the author studies a resonance tuning in dual-coupled PhC nanobeam cavities by laterally shifting the movable cavities with integrated NEMS comb drive actuators. The photonic crystal cavity design is firstly introduced and then the coupled mode theory is discussed as the basic theory of the study of this chapter. Next, the device design is introduced. The analytical and numerical results are sequentially presented. At the end, experimental results are elaborated upon and discussed. The proposed tuning method is proven to have high tuning performance compared with conventional coupling gap tuning. Coupling strength tuning with wide tuning range and high accuracy is realized in experiments. The repeatability and dynamic tuning are also demonstrated. The study in this chapter provides a new way to optimize the coupling strength of the photonic molecules (PhC cavities) and has great potentials in the study of cavity quantum electrodynamics and the development of efficient quantum information devices.

4.1. Design of Photonic Crystal Nanobeam Cavities

4.4.1. Resonator coupled with feeding waveguide

As introduced, the PhC nanobeam cavities investigated are designed to be coupled with feeding waveguides for light input and output as illustrated in Fig. 4.1.

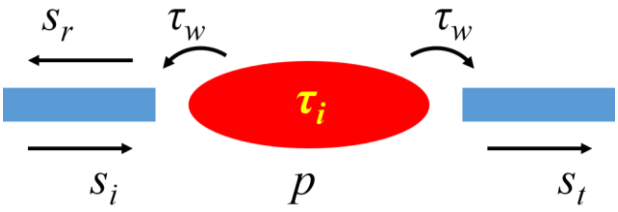

Figure 4.1 Schematic of a resonator coupled with feeding waveguides. The blue parts denote the feeding waveguides, while the red part denotes the cavity.

Assume that the cavity has a resonance mode with amplitude p and resonance frequency ω_0 and $s_i/s_t/s_r$ denote incident/transmitted/reflected waveguide mode amplitudes, respectively. $1/\tau_w$ is employed to denote the decay rate due to feeding waveguide coupling loss and $1/\tau_i$ is employed to denote the intrinsic loss of the cavity. The equations relating these quantities can be given as

$$\frac{d}{dt}p = i\cdot\omega_0 p - \frac{2}{\tau_w}p + \alpha s_i \tag{4.1}$$

$$s_r = \sigma s_i + \xi p \tag{4.2}$$

$$s_t = \xi p \tag{4.3}$$

where constants α and ξ represent the strength of the waveguide coupling and σ is a reflection coefficient. These constants can be determined with methods of energy conservation and time-reversal symmetry and the results are $\alpha = \xi = \sqrt{\frac{2}{\tau_w}}$ and $\sigma = -1$ [186]. Besides, if we further take into consideration of the intrinsic loss of the cavity ($1/\tau_i$), the mode equation can be rewritten into

$$\frac{d}{dt}p = i\cdot\omega_0 p - (\frac{1}{\tau_i}+\frac{2}{\tau_w})p + \sqrt{\frac{2}{\tau_w}}s_i \tag{4.4}$$

By solving this equation, it can be found that

$$|p| = \frac{\sqrt{2/\tau_w}}{(1/\tau_i + 2/\tau_w)}|s_i| \tag{4.5}$$

Combining this result and the constants solved above, the normalized on-resonance amplitude transmission t (= $|s_t|/|s_i|$) is given as

$$t = \frac{2/\tau_w}{(1/\tau_i + 2/\tau_w)} \tag{4.6}$$

One can induce constants Q_i (= $\tau_i\omega_0/2$) and Q_w (= $(\tau_w/2)\omega_0/2$) to denote the cavity quality factor related to intrinsic loss and feeding waveguide coupling loss. Then the total quality factor Q_t can be given as

$$Q_t = \frac{1}{1/Q_w + 1/Q_i} \tag{4.7}$$

and the normalized on-resonance energy transmission T (= $|s_t|^2/|s_i|^2$) can be given as

$$T = \left(\frac{Q_i}{Q_i + Q_w}\right)^2 \tag{4.8}$$

4.4.2. Design principle

As can be seen from Eq. (4.7) and Eq. (4.8), a high waveguide coupling quality factor (Q_w) will result in a high total quality factor (Q_t) but a low transmission (T). In other words, there is a trade-off between the cavity quality factor and transmission. Here in

this section, the design principle of PhC nanobeam cavity in this thesis study for both high quality factor and high transmission is introduced. The principle is developed by Loncar's group at Harvard University [187, 188]. The key factors of the design in achieving high *Q* factors and transmissions at the same time are: (i) zero cavity length, (ii) constant lattice period, and (iii) a Gaussian-like field attenuation profile.

Such cavities can be designed by the following steps:

(1) Determine a target resonance frequency and increase the frequency slightly (by roughly 1%), because the cavity resonance frequency is a little below the lower bandgap edge of the central segment. Given that the wavelength scanning range of our main TLS and OSA is from 1520 nm to 1620 nm, the first order resonance wavelength can be set to be around 1570 nm. It is also noted that the mode polarization is chosen to be transverse electric (TE).

(2) Set the thickness of the cavity beam, which is the thickness of the top single crystal silicon layer of the SOI wafers used, i.e., 260 nm in this case.

(3) Determine the cavity beam width. Cavity with wider beams has higher effective index n_{eff}, which pushes the mode away from the light line, resulting in reduced radiation loss. However, wider cavity beams allow for unwanted multi-mode waves. Here in this thesis, a beam width of about 700 nm is chosen.

(4) Decide the cavity lattice period (cavity hole period) *a* based on $a = \lambda_0/(2n_{eff})$, where

λ_0 is the determined resonance wavelength and n_{eff} is the effective mode index, which can be roughly estimated by numerically modeling a rectangular waveguide with the same cross-section as that of the cavity beam.

(5) Determine the filling factors for each of the PhC lattice. The filling factors arrangement should result in a highest mirror strength (considering it as a Bragg mirror) for the target resonance frequency. In addition, there should be enough segment mirrors to construct a Bragg mirror.

(6) Achieve a Gaussian-like field attenuation profile in the mirror region by linearly tapering the mirror strength, which can be realized by linearly tuning the filling factors.

(7) Finally the cavity can be formed by putting two piece of such Bragg mirrors back to back. Thus the cavity length is zero, resulting in reduced radiation loss and small mode volume.

Generally, in a Bragg mirror, the evanescent field in the mirror region can be given as $\sin(\beta_{Bragg}x)\exp(-\rho x)$, where β_{Bragg} is the propagation constant in the mirror region and ρ is the attenuation constant. The scattering loss in the mirror can be minimized by making $\beta_{Bragg} = \pi/a$. The mode in the cavity region (oscillation region) can be given as $\sin(\beta_{mode}x)$. By making $\beta_{Bragg} = \beta_{mode}$, the scattering loss at the cavity-mirror interface can be minimized.

It is noted that the lattice period is not crucial as long as a bandgap can be formed. The

design also can survive large fabrication tolerances, such as variation in cavity beam cross-section and segment holes diameters. The detailed cavity design will be elaborated in the following sections and chapters together with the entire device design. To reduce the segment scattering loss, a nearly constant propagation constant β_{mode} is required in the oscillation region, which is obtained by the constant lattice period (hole segment period).

Cavities designed with the above principles usually have multi-orders of TE mode. The resonance mode order can be determined by the number of antinodes in the modal field envelope. For example, the mode with one antinode in the modal field envelope is the first order mode. Similarly, the mode with two and three antinodes in its wave field envelope are the second and third order modes, respectively. The first, second and third order TE resonance modes in a single cavity are illustrated by the mode profiles in Figs. 4.2(a-c). It is noted that the mode profiles are described by their individual transverse electrical field distributions.

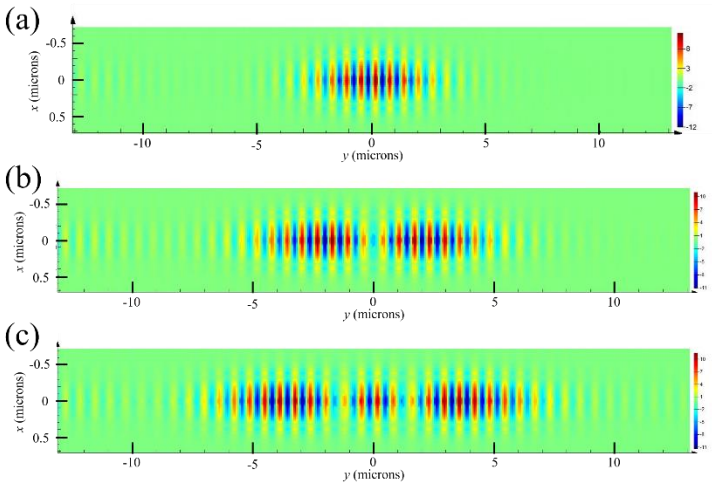

Figure 4.2 Mode profiles of the (a) first order, (b) second order, and (c) third order TE modes in a single cavity.

When two such identical cavities are coupled together, the mode profiles of their first to fourth order even and odd TE modes are as shown in Figs. 4.3(a-h). These mode profiles are obtained by finite-difference time-domain (FDTD) simulation.

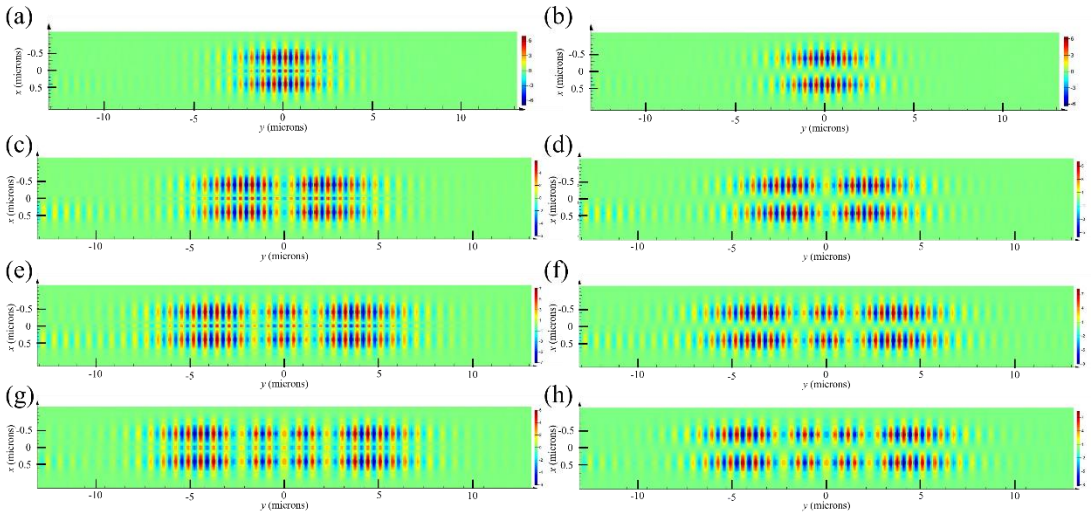

Figure 4.3 Mode profiles of the (a, b) first order even and odd, (c, d) second order even and odd, (e, f) third order eve and odd, and (g, h) fourth order eve and odd TE mode in dual-coupled cavities.

4.2. Coupled Mode Theory

Coupling of optical modes is widely involved in photonic devices, which can be analyzed by the well-established coupled mode theory (CMT) [189-194]. The theory generally includes two portions, spatial CMT and temporal CMT. Spatial CMT is widely used to describe the coupling between propagation modes on two waveguides, placed parallel and close to each other [190-193], while temporal CMT is extensively employed to analyze coupled resonant modes on coupled optical resonators [189, 194]. Here, temporal CMT is discussed as it is the basic theory of the study in this chapter.

If the two resonant modes p_1 and p_2 on the two identical resonators are given as

$$p_1(t,z) = P_1 \mathrm{e}^{i\cdot\omega_0 t} \quad \text{and} \quad p_2(t,z) = P_2 \mathrm{e}^{i\cdot\omega_0 t} \tag{4.9}$$

where ω_0 is the nature frequency of a single resonator, the temporal coupled mode equations can be given as

$$\frac{d}{dt} p_1 = i\cdot\omega_0 p_1 + i\cdot\kappa_{21} p_2 \tag{4.10}$$

$$\frac{d}{dt} p_2 = i\cdot\omega_0 p_2 + i\cdot\kappa_{12} p_1 \tag{4.11}$$

where κ_{21} and κ_{12} are the coupling strengths from mode p_2 to mode p_1 and mode p_1 to mode p_2 respectively. Consider a conservative coupling case, the coupling strength is determined by the field overlap integral of the two modes and can be defined as

$$\kappa_{ij} = -\omega\int(\varepsilon_1 - \varepsilon_2)\vec{e}_i^{*}\vec{e}_j dV, i, j = 1,2 \tag{4.12}$$

where ε_1 and ε_2 are the permittivities of the photonic material and its surrounding; $\vec{e}_1$ and $\vec{e}_2$ denote the electric field of the two modes; asterisk * symbol denotes complex conjugate. In an energy conservation system, where

$$\frac{d}{dt}(|p_1|^2 + |p_2|^2) = 0 \tag{4.13}$$

it can be obtained that

$$\kappa_{12} = \kappa_{21}{}^{*} = \kappa \tag{4.14}$$

Thus

$$\frac{d}{dt}p_1 = i\cdot\omega_0 p_1 + i\cdot\kappa p_2 \tag{4.15}$$

$$\frac{d}{dt}p_2 = i\cdot\omega_0 p_2 + i\cdot\kappa p_1 \tag{4.16}$$

Considering a coupled supermode at frequency ω_d, i.e. $P_1 = p_1 \exp(i\,\omega_d t)$ and $P_2 = p_2 \exp(i\,\omega_d t)$, we can obtain the following matrix equation

$$\begin{bmatrix} i\cdot\omega_0 & i\cdot\kappa \\ i\cdot\kappa & i\cdot\omega_0 \end{bmatrix}\begin{bmatrix} p_1 \\ p_2 \end{bmatrix} = i\cdot\omega_d \begin{bmatrix} p_1 \\ p_2 \end{bmatrix} \tag{4.17}$$

To have non-trivial solutions of p_1 and p_2, the following determinant must be zero

$$\begin{vmatrix} i\cdot\omega_0 - i\cdot\omega_d & i\cdot\kappa \\ i\cdot\kappa & i\cdot\omega_0 - i\cdot\omega_d \end{vmatrix} = 0 \tag{4.18}$$

Then the resulting resonance frequency can be solved and given as

$$\omega_d = \omega_0 \pm \kappa \tag{4.19}$$

The parities of the coupled modes can also be solved

$$\frac{p_1}{p_2} = \frac{\omega_d - \omega_0}{\kappa} \tag{4.20}$$

Here we induce the phase differences of either supermode for the mode parity determination and the phase difference can be given as

$$\Delta\varphi = \begin{cases} 0, & (\omega_d - \omega_0)/\kappa > 0 \\ \pm\pi, & (\omega_d - \omega_0)/\kappa < 0 \end{cases} \tag{4.21}$$

If the phase difference is about zero, the supermode is even-like, while if the phase difference is about ±π, the supermode is odd-like. If the two coupled resonators are not exactly identical, the temporal coupled mode equations become

$$\frac{d}{dt} p_1 = i \cdot \omega_1 p_1 + i \cdot \kappa p_2 \tag{4.22}$$

$$\frac{d}{dt} p_2 = i \cdot \omega_2 p_2 + i \cdot \kappa p_1 \tag{4.23}$$

where ω_1 and ω_2 are the individual nature resonance frequencies of the two resonators. In this case, the resulting resonance frequencies become

$$\omega_d = \frac{\omega_1 + \omega_2}{2} \pm \sqrt{\frac{1}{4}\Delta\omega^2 + \kappa^2} \tag{4.24}$$

where $\Delta\omega$ denotes the resonance frequency detuning ($\Delta\omega = |\omega_1 - \omega_2|$). If the energy decay of the resonators is further taken into consideration, the general case of the coupled equations can be given as

$$\frac{d}{dt} p_1 = i \cdot \omega_1 p_1 - \frac{1}{\tau_1} p_1 + i \cdot \kappa p_2 \tag{4.25}$$

$$\frac{d}{dt} p_2 = i \cdot \omega_2 p_2 - \frac{1}{\tau_2} p_2 + i \cdot \kappa p_1 \tag{4.26}$$

where τ_1 and τ_2 are the respective photon lifetimes in the two resonators. The eigenvalue

can be solved as

$$\chi = \frac{\omega_1 + \omega_2}{2} + i \cdot \frac{1}{2}\left(\frac{1}{\tau_1} + \frac{1}{\tau_2}\right) \pm \sqrt{\frac{1}{4}\left(\omega_1 - \omega_2 + i \cdot \left(\frac{1}{\tau_1} - \frac{1}{\tau_2}\right)\right)^2 + \kappa^2} \tag{4.27}$$

The real part of the eigenvalue (Re(χ)) denotes the resulting resonance frequency (ω_d), while the imaginary part of the eigenvalue (Img(χ)) denotes the resulting decay rate ($1/\tau_d$). In this case, the mode parities and phase differences can be given as

$$\frac{p_1}{p_2} = \frac{\omega_d - \omega_2}{\kappa} + i \cdot \frac{\frac{1}{\tau_d} - \frac{1}{\tau_2}}{\kappa} \tag{4.28}$$

$$\Delta\varphi = \begin{cases} \tan^{-1}\dfrac{y}{x}, & x > 0 \\ \tan^{-1}\dfrac{y}{x} + \pi, & x < 0 \text{ and } y \geq 0 \\ \tan^{-1}\dfrac{y}{x} - \pi, & x < 0 \text{ and } y < 0 \end{cases} \tag{4.29}$$

where $x = \dfrac{\omega_d - \omega_2}{\kappa}$ and $y = \dfrac{\frac{1}{\tau_d} - \frac{1}{\tau_2}}{\kappa}$.

4.3. Device Design

Existing studies of resonance tuning in a dual-coupled PhC nanobeam cavities are mainly focused on the resonance tuning through coupling gap variation between the cavities [93, 95, 97]. Here, by laterally shifting the center-to-center offset of coupled photonic crystal nanobeam cavities while maintaining a constant coupling gap, the author demonstrates a method to precisely and dynamically control the coupling

strength of coupled photonic crystal cavities through integrated NEMS actuators with a precision of a few GHz over a range of several THz without modifying the nature of their constituent resonators. Furthermore, the coupling strength can be tuned continuously from negative (strong coupling regime) to zero (weak coupling regime) and further to positive (strong coupling regime) and vice versa.

Figure 4.4 shows the SEM image of the NEMS tunable coupled PhC nanobeam cavities. As can be seen, one of the cavity beam is fixed and light is launched into and coupled out from this cavity through suspended Si nanowire feeding waveguides. The other cavity is movable and integrated with NEMS comb drive actuators that are supported by four folded beam suspensions. Thus, the movable cavity can move in the lateral direction, while the coupling gap keeps constant.

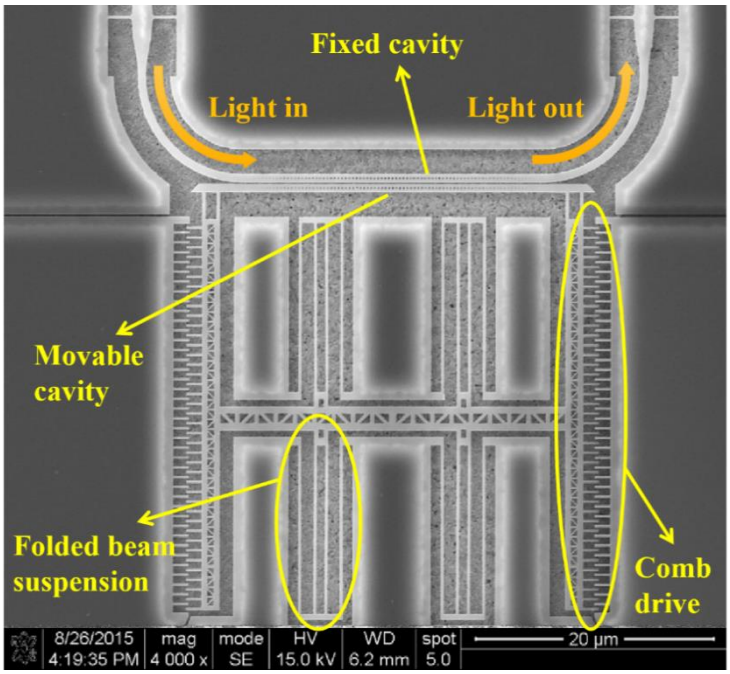

Figure 4.4 SEM image of the device NEMS controlled dual-coupled PhC nanobeam cavities.

The comb drive actuation force can be estimated as [55]

$$F = m\frac{\varepsilon t V^2}{g_c} \tag{4.30}$$

where m is the number of movable fingers; ε is the ambient permittivity; t and g_c are the finger thickness and finger gap spacing of the comb drive, respectively and V is the applied voltage. The total spring constant of the four sets of the folded beam suspension can be given by [55]

$$k = 4\frac{b^3 t}{l^3}E \tag{4.31}$$

where b, and l are the flexural beam width and length respectively, and E is the Young's Modulus of the beam material.

Both cavity beams are designed to be of 700 nm in width. There are 79 holes etched in each beam with a constant period of 310 nm, forming a PhC cavity. The diameters of the holes are quadratically tuned from 190 nm at the center to 40 nm at both ends. More specifically, the radius of the air-holes r_m, (m changes from 1 to 40, denoting the number of holes from the center to either end of the cavity) is given as: $r_m = r_1 \times (1-(r_1-r_{40})/r_1 \times ((m-1)/39)^2)$, where r_1 is 190 nm and r_{40} is 40 nm.

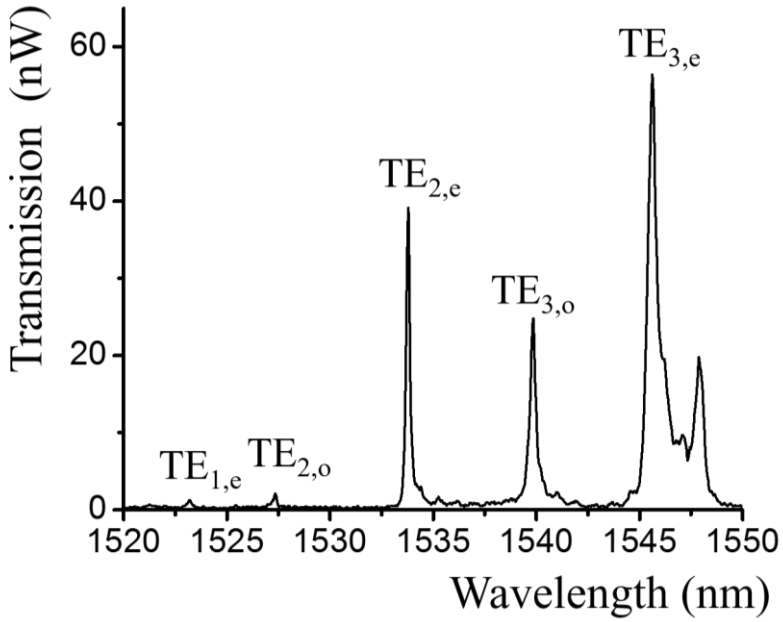

Figure 4.5 The transmission spectra of dual-coupled PhC nanobeam cavities. Five modes are observed, namely $TE_{1,e}$, $TE_{2,o}$, $TE_{2,e}$, $TE_{3,o}$, $TE_{3,e}$, corresponding to the 1st even-like mode, the 2nd odd-like mode, the 2nd even-like mode, the 3rd odd-like mode and the 3rd even-like mode. (FDTD simulations are used to identify the modes.)

The measured transmission spectrum of a typical dual-coupled PhC nanobeam cavities when two cavities are perfectly aligned without lateral offset is shown in Fig. 4.5, where the resonance peaks of the TE-like modes are marked. The results are measured by wavelength scanning by the main TLS and OSA which are synchronized together.

The interaction of the two cavities causes a splitting of their original uncoupled modes into corresponding pairs of even-like and odd-like supermodes. (If the two nanobeam cavities are not exactly identical due to fabrication imperfections, the supermodes are not perfectly symmetric or anti-symmetric) The splitting is analogous to that of the electron states in diatomic molecules, where the degenerate atomic levels split into bonding and anti-bonding orbitals as a result of the strong coupling of two atoms. In

coupled PhC cavities, the coupling strength of the modes is determined by the mode overlapping of the two uncoupled cavities, which is sensitive to the relative displacement between them. In this work, when the movable cavity is displaced laterally, the coupling strength can be varied drastically from a negative to the positive sense and vice versa, resulting in the variation of the mode splitting width (see Fig. 4.6).

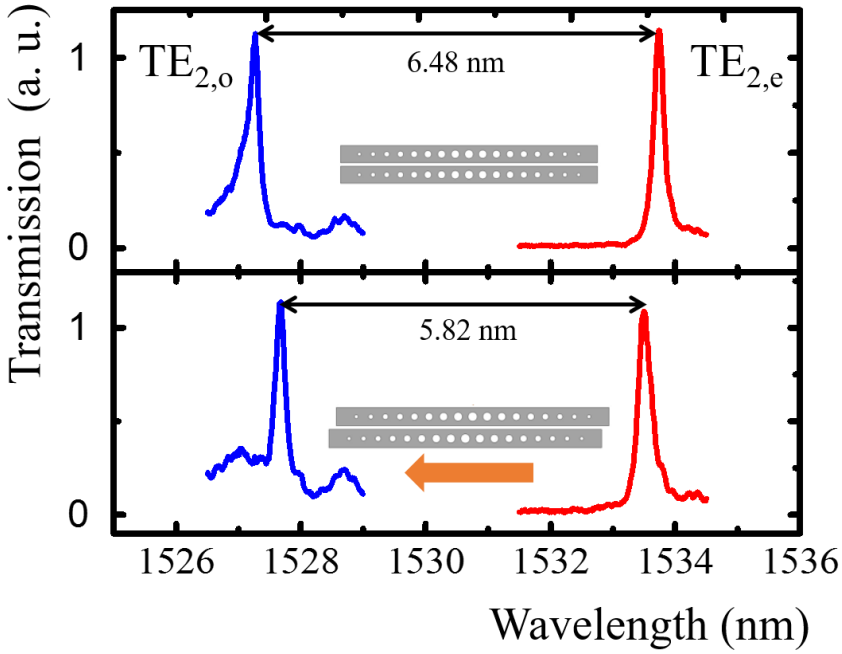

Figure 4.6 Illustration of mode splitting width change of the coupled cavities due to a lateral displacement of the movable cavity.

4.4. Results and Discussion

4.4.1. Analytical and numerical results

The mode coupling between PhC nanobeam cavities (with individual resonance frequency of ω_1 and ω_2) can be described by the coupled mode theory introduced in Section 4.2. The resultant supermodes resonance frequencies can be predicted by Eq. (4.19) or Eq. (4.24), depending on whether the two cavities are identical. The phase

difference and the supermode symmetry can be determined by Eq. (4.21).

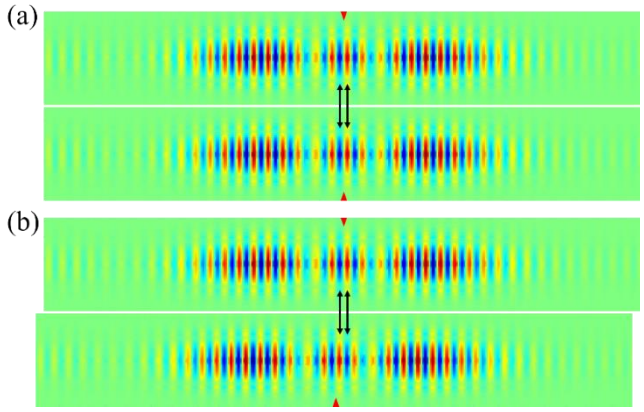

Figure 4.7 (a) At initial condition when the cavity holes are perfectly aligned, the overlapping electric fields of two single PhC nanobeam cavity modes are in-phase (the red arrow indicates the cavity center). Note: The mode profile shows the in-plane electric field component (in the direction perpendicular to the nanobeam) in a horizontal plane at half the silicon nanobeam height, and the resonance wavelength is around 1600.5 nm. (b) When the movable PhC nanobeam cavity is laterally shifted by one lattice, the overlapping electric fields of two single cavity modes are out-of-phase (the red arrow indicates the cavity center).

In the coupled PhC nanobeam cavities system, as shown in Fig. 4.7(a), the mode distributions of the two uncoupled cavities are originally symmetric about the perpendicular bisector plane of the line segment that connects the centers of the coupled cavities. Hence, the electric fields of both uncoupled cavities in the overlapping integration area have the same sign. It is noted that according to Eq. (4.12), the coupling strength at the initial condition is negative. When the movable cavity is laterally shifted by one lattice, the signs of the electric fields of the two uncoupled cavities in the overlapping integration area are opposite to each other (as shown in Fig. 4.7(b)). Therefore, the coupling strength becomes positive. It is this unique integrated NEMS tuning mechanism that allows the coupling strength to vary precisely from negative strong coupling to zero (weak coupling) and further to positive strong coupling with a

lateral displacement of about one PhC lattice.

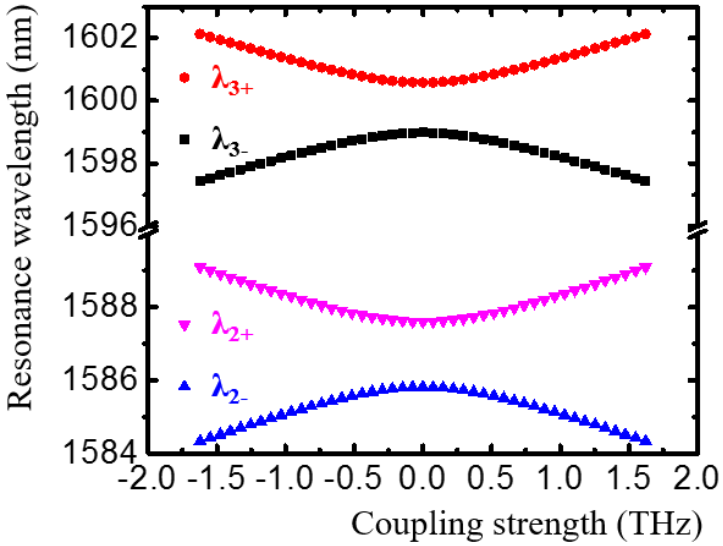

Figure 4.8 Relationship between the second and third supermode resonance wavelength and coupling strength κ for non-zero detuning case.

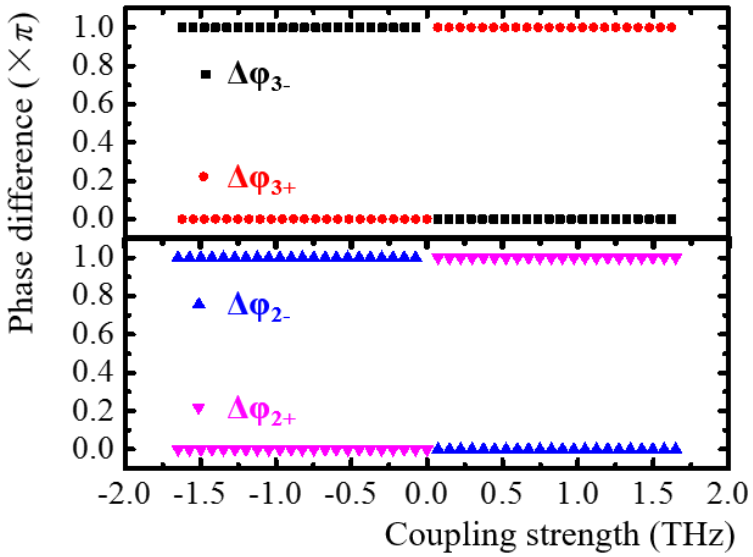

Figure 4.9 Relationship between the second and third order supermode phase difference $\Delta\varphi$ and coupling strength κ for non-zero detuning case.

The eigenwavelengths $\lambda_{\pm}$ (λ_{+} denotes the mode with a longer wavelength, while λ_{-} denotes the mode with a shorter wavelength) of a pair of coupled supermodes are calculated as the coupling strength changes from a negative to a positive value. For non-

zero detuning ($\Delta\omega = |\omega_1 - \omega_2| \neq 0$), when κ is negative and increases towards zero, λ_+ decreases and λ_- increases, resulting in reduced mode splitting width as shown in Fig. 4.8 for the selected second and third order modes.

Their respective phase differences $\Delta\varphi$ are calculated and shown in Fig. 4.9. It is observed that when κ is negative, the supermodes corresponding to λ_+ and λ_- have even-like and odd-like parities, respectively. When κ becomes zero, the mode splitting width is equal to the initial detuning. As κ continues to increase from zero to a positive value, λ_+ increases while λ_- decreases, and the mode splitting width increases. In addition, the supermode corresponding to λ_+ now becomes an odd-like mode, whereas that corresponding to λ_- becomes an even-like mode, which can be concluded from the mode phase differences shown in Fig. 4.9.

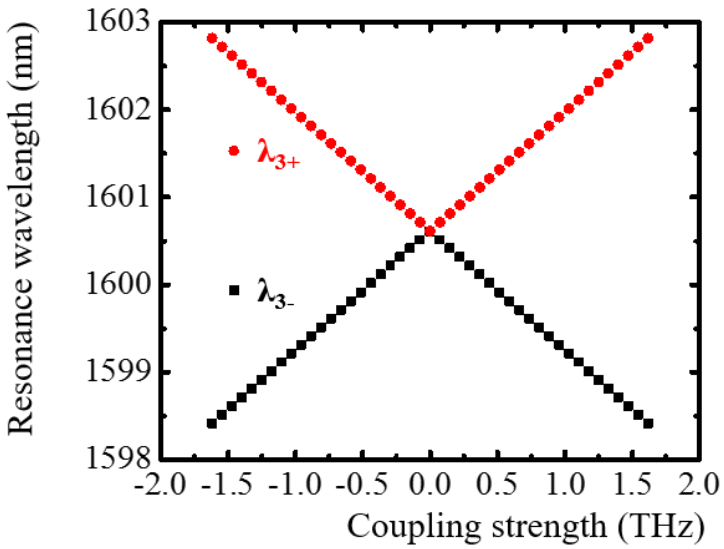

Figure 4.10 Relationship between the third order supermode resonance wavelength and coupling strength κ for zero detuning case.

The mode parity inversion is due to oscillation of the evanescent field along the lateral

tuning direction that leads to the sign inversion of the coupling strength. In the case of zero detuning ($\omega_1 = \omega_2$), the variation trends of λ_+ and λ_- are similar to that of non-zero detuning, but the mode splitting vanishes when κ is zero, as shown in Fig. 4.10 for the selected third order supermodes. As κ increases from a negative value to a positive value, the supermode corresponding to λ_+ (λ_-) also changes from even-like (odd-like) mode to odd-like (even-like) mode, as indicated in Fig. 4.11.

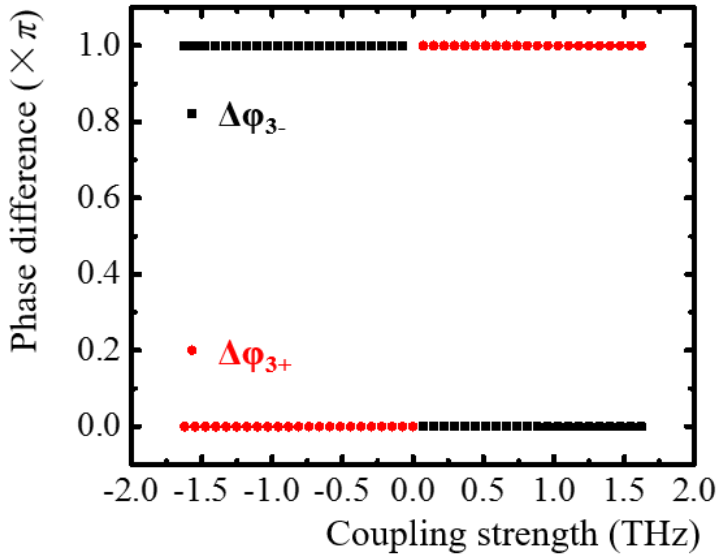

Figure 4.11 Relationship between the third supermode phase difference $\Delta\varphi$ and coupling strength κ for zero detuning case.

3D FDTD simulations were performed to calculate the supermode wavelength shifts and mode field distributions of the coupled PhC nanobeam cavities when the movable cavity is set at different lateral displacements. The FDTD method generates a time-domain pulse as the excitation source to the feeding waveguide. According to the Fourier transform theory, a time-domain confined signal spreads over a broad frequency range in the frequency-domain. The transmitted electromagnetic field in the time-domain is recorded. Subsequently, a Fourier transform reveals the frequency-

domain response of the input pulse, which corresponds to the device transmission spectrum. The peaks within the forbidden band denote the supermodes, whose mode profiles, orders, and symmetries are then determined at their respective frequencies. Also note that the governing equation is Maxwell's equations in the FDTD solution.

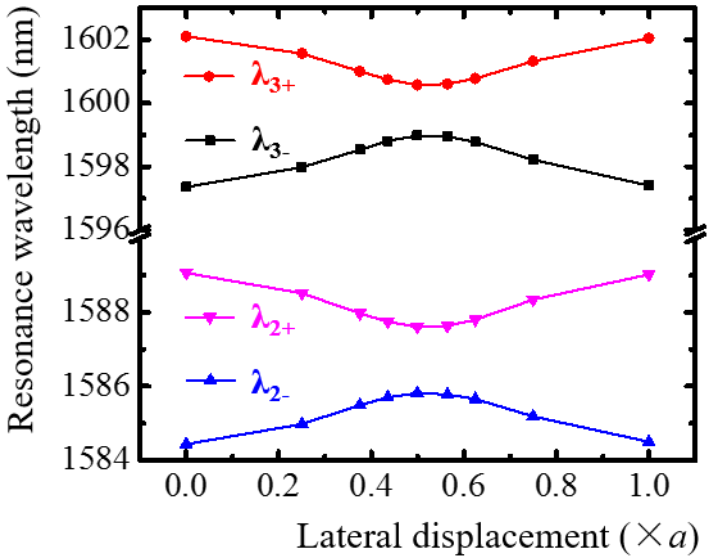

Figure 4.12 FDTD simulated relationship between the second and third order supermode resonance wavelength and lateral displacement *d* for non-zero detuning case. *a* denotes the cavity lattice period.

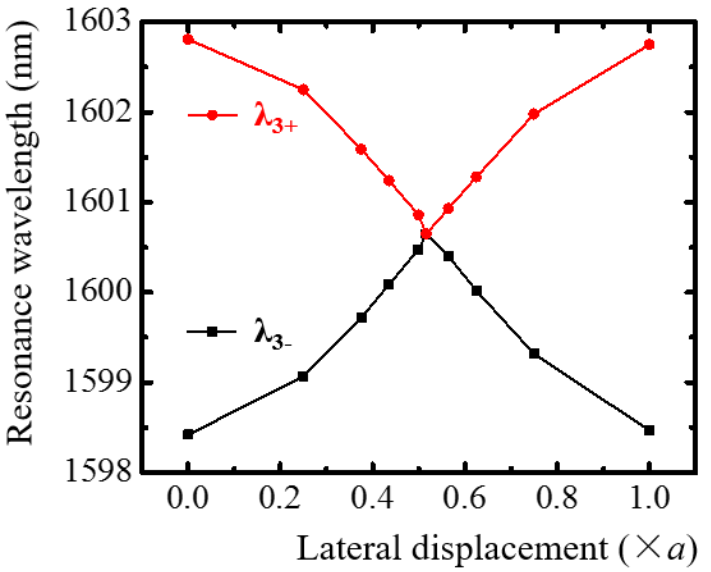

Figure 4.13 FDTD simulated relationship between the third order supermode resonance wavelengths and lateral displacement *d* for zero detuning case.

The zero detuning case is simulated with two identical cavities, while the non-zero detuning case is simulated with two cavities having slightly different nanobeam widths. The simulation results are summarized in Fig.4.12 and Fig. 4.13. When the movable cavity is laterally shifted (see the schematics in Fig. 4.7), the coupling strength increases from an initial negative value to zero at about half PhC lattice offset and then further increases to a positive value for one lattice offset. The FDTD simulated wavelength shifts of the selected supermodes, shown in Fig. 4.12 and Fig. 4.13 respectively for both non-zero detuning and zero detuning cases, are in good agreement with the results predicted with the coupled mode theory shown in Fig. 4.8 and Fig. 4.10. The relationships between the supermode resonance wavelength and coupling strength corresponding to Fig. 4.12 and Fig. 4.13 are shown in Fig. 4.14 and Fig. 4.15, respectively.

The coupling strength can be calculated with Eq. (4.19) and Eq. (4.24). More specifically, for zero detuning case, the coupling strength can be given as

$$\kappa = \begin{cases} -\frac{1}{2}\left(\omega_{d,+} - \omega_{d,-}\right), & d < \frac{1}{2}a \\ 0, & d = \frac{1}{2}a \\ \frac{1}{2}\left(\omega_{d,+} - \omega_{d,-}\right), & d > \frac{1}{2}a \end{cases} \tag{4.32}$$

while for the non-zero detuning case, the coupling strength can be given as

$$\kappa = \begin{cases} -\frac{1}{2}\sqrt{\left(\omega_{d,+} - \omega_{d,-}\right)^2 - \Delta\omega^2}, & d < \frac{1}{2}a \\ 0, & d = \frac{1}{2}a \\ \frac{1}{2}\sqrt{\left(\omega_{d,+} - \omega_{d,-}\right)^2 - \Delta\omega^2}, & d > \frac{1}{2}a \end{cases} \tag{4.33}$$

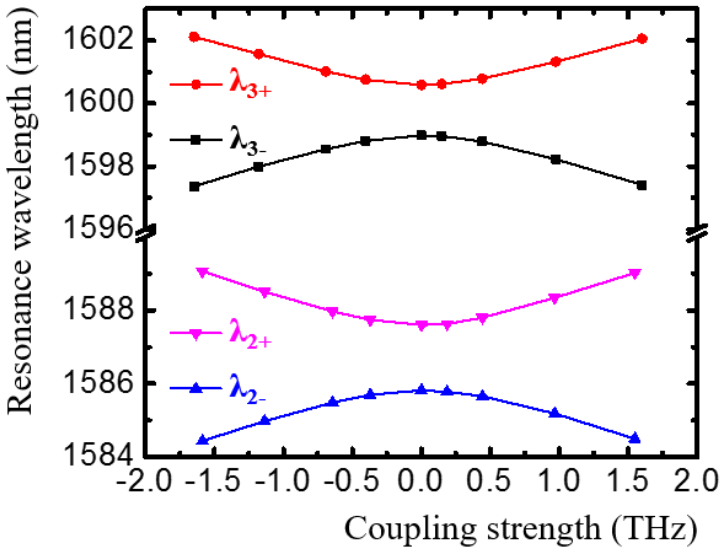

Figure 4.14 FDTD simulated relationship between the second and third order supermode resonance wavelength and coupling strength κ for non-zero detuning case.

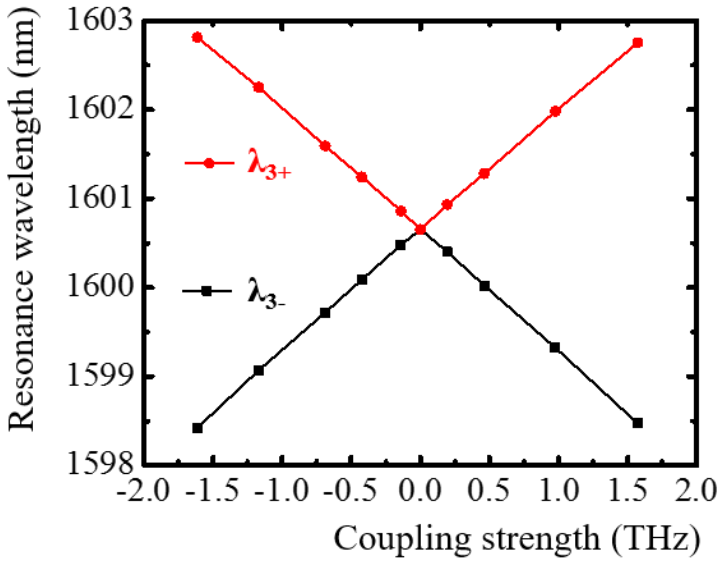

Figure 4.15 FDTD simulated relationship between the third order supermode resonance wavelength and coupling strength κ for zero detuning case.

Figure 4.16 further highlights the mode field distributions obtained from FDTD simulations for various cavity-coupling configurations with different lateral offsets *d*. For clarity, only a central part of the field distribution is shown for each supermode with two red triangles indicating the two cavity centers.

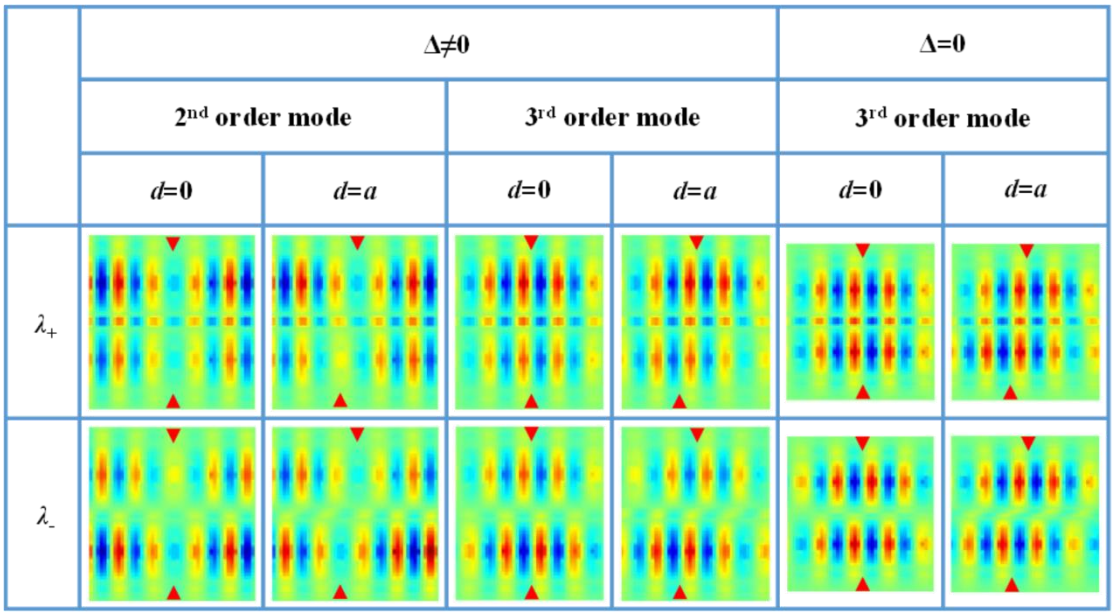

Figure 4.16 Mode profile variations for both non-zero detuning ($\Delta\omega \neq 0$) and zero detuning cases ($\Delta\omega = 0$) with red arrows indicating cavity centers. Note: The lattice period of the two coupled PhC nanobeam cavities is fixed at 310 nm (a = 310 nm) for both non-zero and zero detuning cases. The mode profile indicates the in-plane electric field component (in the direction perpendicular to the nanobeam) in a horizontal plane at half the silicon nanobeam height.

These mode profiles shown in Fig. 4.16 also support the mode parity predictions obtained from the coupled mode theory. To illustrate this clearly, one can take the zero detuning case ($\omega_1 = \omega_2 = \omega_0$) as an example and consider two uncoupled third order modes from two identical single cavities that are put close to each other with zero center-to-center lateral offset (d = 0 nm), as shown schematically in Fig. 4.17(a). The coupling strength is determined to be negative ($\kappa < 0$) from Eq. (4.12). Subsequently,

(ω_d-ω_0)/κ is positive for the supermode with a longer wavelength (λ_+), and thus according to Eq. (4.21), the phase difference $\Delta\varphi$ is zero and the mode is even-like. On the contrary, the supermode having a shorter wavelength (λ_-) has an odd-like parity with a phase difference $\Delta\varphi$ equal to π.

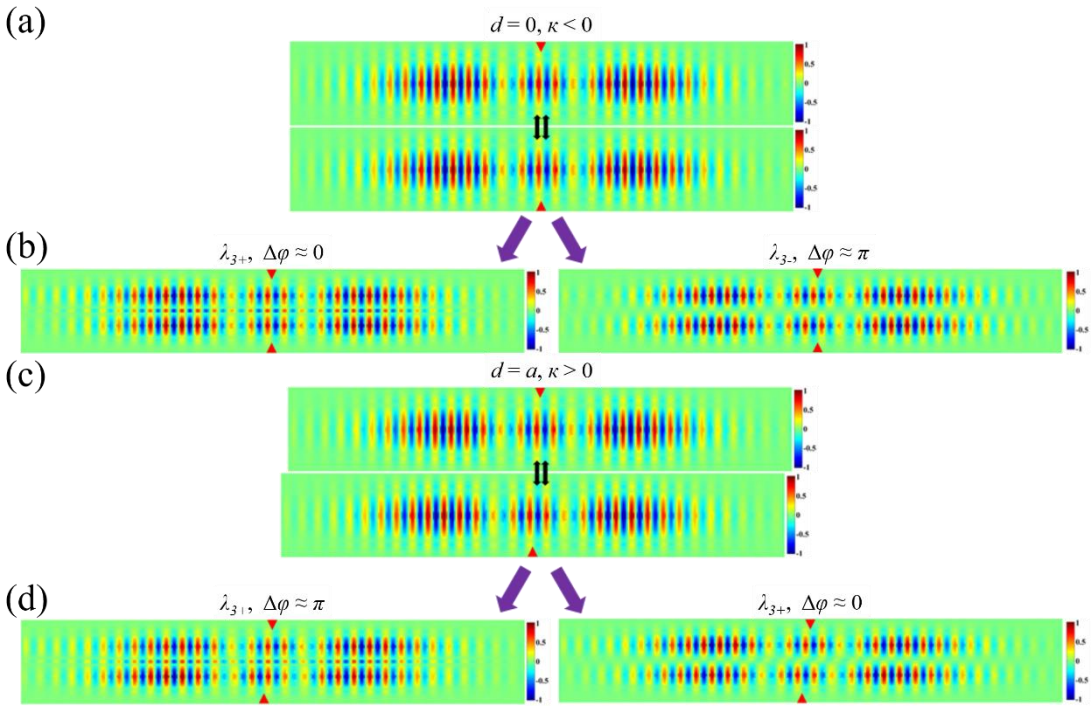

Figure 4.17 (a) The mode profiles of two uncoupled PhC nanobeam cavities with zero center-to-center lateral offset; (b) the FDTD simulated supermode profiles of PhC nanobeam cavity with no center-to-center lateral offset between two nanobeams; (c) the mode profiles of two uncoupled PhC nanobeam cavities with a lateral offset of one PhC lattice period a (a = 310 nm); (d) the FDTD simulated supermode profiles of coupled PhC nanobeam cavities with a lateral center-to-center offset of 310 nm; Notes: the mode profile indicates the in-plane electric field component (in the direction perpendicular to the nanobeam) in a horizontal plane at half the silicon nanobeam height, and the resonance wavelength of each single cavity is around 1600.5 nm.

Taking the original uncoupled mode profiles and their phase differences into consideration, the resulting supermode field distributions of the coupled cavities can be predicted conceptually by superposition and are confirmed by the FDTD simulated third order supermodes shown in Fig. 4.17(b). Similarly, one can consider the

configuration where two cavities have a lateral center-to-center offset of one PhC lattice period ($d = a$ = 310 nm). The uncoupled third order mode profiles and their relative positions are illustrated in Fig. 4.17(c). Clearly, the coupling strength is now positive ($\kappa > 0$), and the mode parities are inversed. The supermode with a longer wavelength (λ_+), having $(\omega_d-\omega_0)/\kappa < 0$ (refer to Eq. (4.21)) and thus $\Delta\varphi = \pi$, becomes odd-like, whereas the supermode having a shorter wavelength (λ_-) becomes even-like. Again taken the original uncoupled mode profiles shown in Fig. 4.17(c) and their phase differences in supermodes into consideration, the resulting field distributions of the coupled cavities can be deduced and they match well with the FDTD simulated third order supermodes shown in Fig. 4.17(d). The parity of a supermode can also be determined by comparing the signs of the electric fields at identical locations in two coupled cavities (see Fig. 4.16). Taking the second order supermodes for example, at d = 0 nm, the sign of the electric field at each cavity center is the same for λ_+ mode and different for λ_- mode, indicating their even-like and odd-like parity respectively. At d = 310 nm however, the sign of the electric field at each cavity center becomes different for λ_+ mode and the same for λ_- mode instead, which clearly indicates a mode parity inversion.

4.4.2. Experimental results

In experiments, the lateral displacement of the movable nanobeam cavity is precisely controlled by the integrated NEMS comb drive actuators. Through gradually raising the

applied DC voltage, the lateral displacement is increased stepwise, 1~16 nm per step. The relationship between the center-to-center lateral offsets and applied voltages is presented in Table 4.1. Two samples were tested; sample A represents a non-zero detuning case, while Sample B represents a zero detuning case. The lattice period (cavity holes period) *a* of both Sample A and Sample B is 310 nm.

Table 4.1 The cavity center-to-center lateral offsets of various applied voltages

Sample A (Δ≠0)			**Sample B (Δ≈0)**		
Voltage squared (V^2)	**Cavity center-to-center lateral offset (nm)**	**Cavity center-to-center lateral offset (×*a*)**	**Voltage squared (V^2)**	**Cavity center-to-center lateral offset (nm)**	**Cavity center-to-center lateral offset (×*a*)**
0	-25.48	-0.08219	**0**	0	0
5.76	-13.50	-0.04355	**5.76**	9.94	0.03208
12.25*	0*	0*	**12.25**	21.15	0.06822
17.64	11.21	0.03616	**17.64**	30.45	0.09824
24.01	24.46	0.07890	**24.01**	41.45	0.13372
30.25	37.44	0.12077	**30.25**	52.22	0.16847
36	49.40	0.15935	**36.00**	62.15	0.20049
42.25	62.40	0.20129	**42.25**	72.94	0.23530
47.61	73.55	0.23725	**44.89**	77.50	0.25000
53.29	85.36	0.27536	**46.24**	79.83	0.25752
59.29	97.84	0.31562	**47.61**	82.20	0.26515
65.61	110.99	0.35802	**49.00**	84.60	0.27289
72.25	124.80	0.40258	**53.29**	92.00	0.29678
77.44	135.59	0.43740	**59.29**	102.36	0.33020
84.64	150.57	0.48571	**65.61**	113.27	0.36539
90.25	162.24	0.52335	**72.25**	124.74	0.40237
96.04	174.28	0.56220	**77.44**	133.70	0.43128
102.01	186.70	0.60225	**79.21**	136.75	0.44113
108.16	199.49	0.64352	**84.64**	146.13	0.47137
114.49	212.66	0.68599	**90.25**	155.81	0.50262
121	226.20	0.72967	**91.2025**	157.46	0.50792
125.44	235.43	0.75946	**92.16**	159.11	0.51325
132.25	249.60	0.80515	**94.09**	162.44	0.52400
136.89	259.25	0.83629	**96.04**	165.81	0.53486
144	274.04	0.88399	**102.01**	176.11	0.56811

148.84	284.10	0.91647	**108.16**	186.73	0.60236
156.25	299.52	0.96618	**114.49**	197.66	0.63761
161.29	310	1	**121.00**	208.90	0.67387
169	326.04	1.05173	**125.44**	216.56	0.69860
174.24	336.94	1.08689	**132.25**	228.32	0.73652
			136.89	236.33	0.76236
			144.00	248.61	0.80196
			148.84	256.96	0.82892
			156.25	269.76	0.87018
			161.29	278.46	0.89825
			169.00	291.77	0.94119
			174.24	300.82	0.97037
			179.56	310	1
			184.96	319.32	1.03007

*Due to fabrication imperfections, the movable cavity of Sample A has an initial lateral offset (see Figs. 4.18(b) and (c)). The cavity center-to-center lateral offset is zero when the voltage squared is 12.25 V^2.

The transmission spectra of the coupled PhC nanobeam cavities under different cavity center-to-center lateral offsets are obtained. For non-zero detuning as shown in Fig. 4.18(a) (Sample A), the widths of the two PhC nanobeam cavities are measured under SEM to be around 594 nm and 600 nm, respectively. The resonance wavelengths of the second and third order supermodes at different cavity center-to-center lateral offsets are illustrated in Figs. 4.18(b) and (c), respectively. Clearly, the mode splitting width decreases with increment in lateral offset until the mode splitting width reaches a minimum value, which is related to the initial frequency detuning of the two uncoupled cavities. As the lateral offset continues to increase, the mode splitting width increases again. Compared with the third order supermodes, the second order supermodes have a larger mode splitting minimum, which indicates a larger initial frequency detuning. In this unique NEMS lateral tuning design described here, the mode frequencies (ω_1, ω_2)

of the uncoupled PhC nanobeam cavities can be obtained by Lorentzian fitting the measured resonance peaks at near-zero coupling strength at a lateral offset of around half of a PhC lattice where the mode splitting width reaches a minimum.

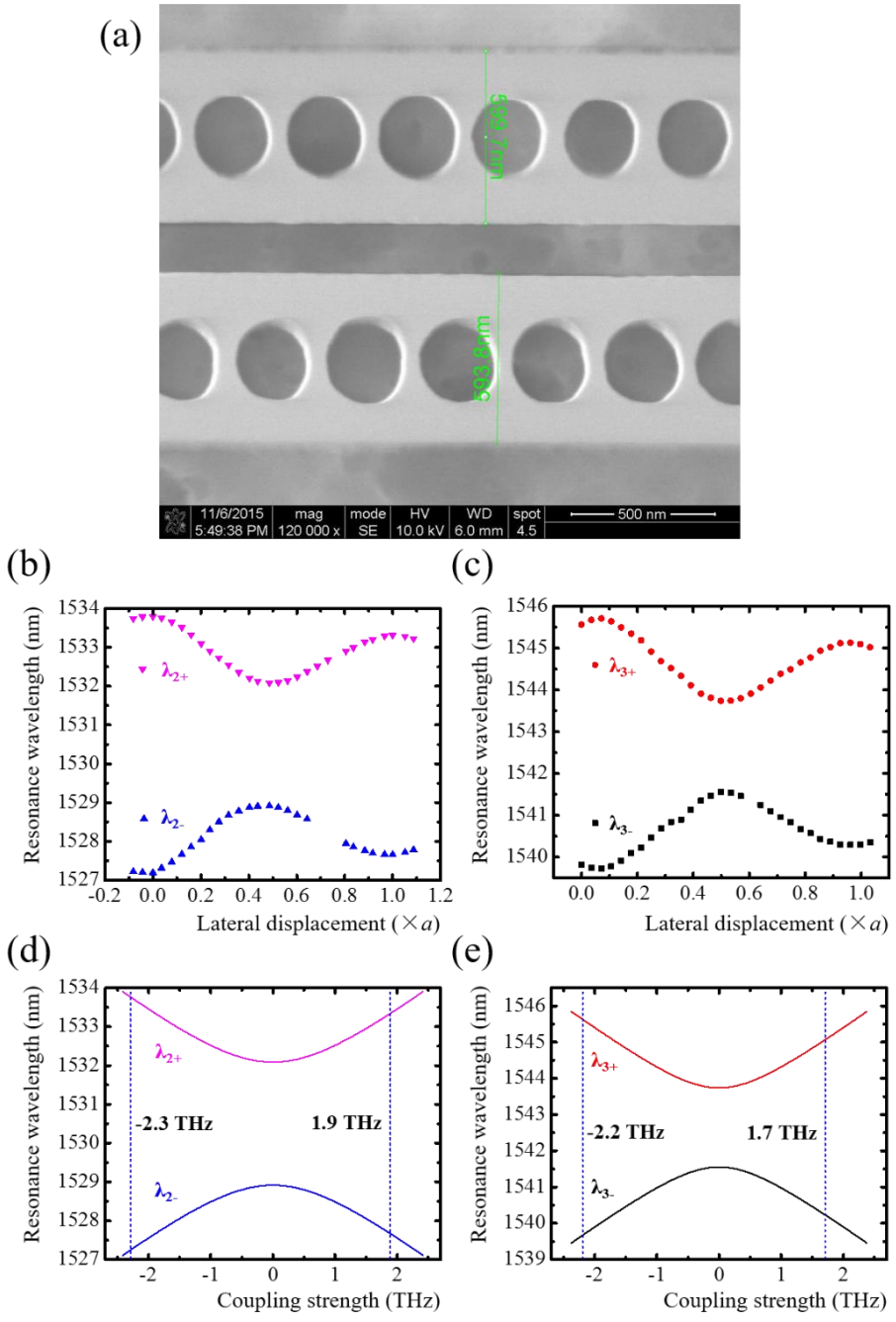

Figure 4.18 (a) SEM image showing the central part of a non-zero detuned coupled PhC nanobeam cavities (Sample A) with measured widths of the nanobeams annotated. (b, c) Measured resonance wavelengths of the second order and third order supermodes as functions of the cavity center-to-center lateral offset for Sample A. (d, e) Calculated

relationship between the second order and third order resonance wavelength and the coupling strength for Sample A.

With ω_1, and ω_2, known, the wavelengths of the coupled cavities supermodes at various coupling strength are calculated using Eq. (4.33) and plotted in Figs. 4.18(d) and (e). Comparing the mode splitting widths in Fig. 4.18(d) with those in Fig. 4.18(b), it can be concluded that the coupling strength κ is continuously tuned from -2.3 THz to 1.9 THz for the second order supermodes. Similarly, the experimental coupling strength tuning range is from -2.2 THz to 1.7 THz for the third order supermodes by comparing Fig 4.18(e) with Fig. 4.18(c).

Figure 4.19(a) presents a nearly zero detuning case (Sample B), where both of the nanobeams are measured to be around 658 nm in width. Similar to Sample A, when the cavity center-to-center lateral offset increases, the mode splitting width decreases to a minimum and then increases again as predicted (see Figs. 4.19(b) and (d)). In this case, the minimum mode splitting width, which is equal to the initial mode detuning between the two uncoupled PhC nanobeam cavities, is only 80 GHz ($\Delta\lambda \approx 106$ pm). Again, with the mode frequencies (ω_1, ω_2) of the uncoupled PhC nanobeam cavities obtained, the resonance wavelengths of the coupled cavities supermodes are computed as functions of the coupling strength (using Eq. (4.32)) and plotted in Fig. 4.19(c). Comparing it with the experimental results in Fig. 4.19(b), it is observed that the coupling strength κ is continuously tuned from -1.7 THz to 1.6 THz.

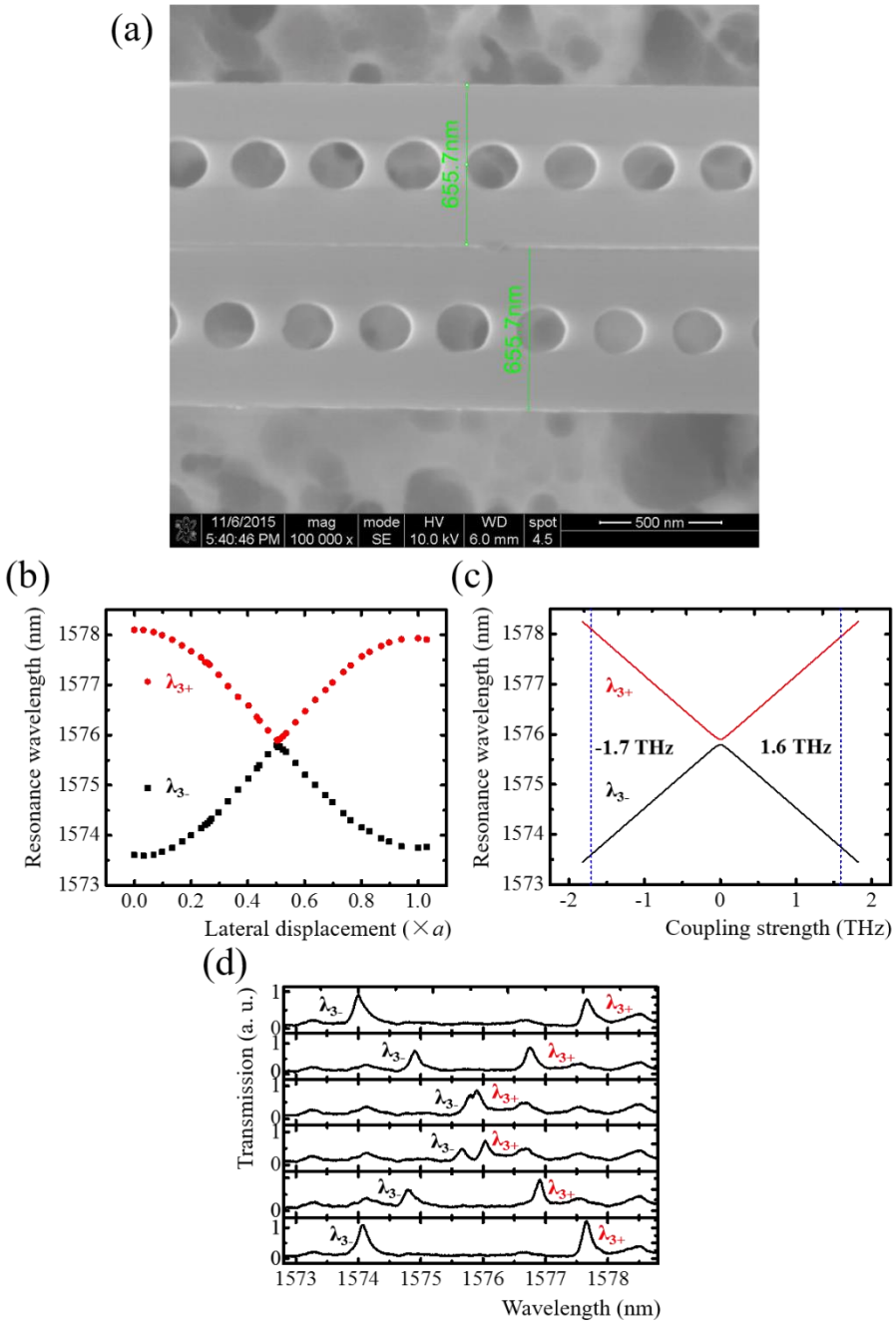

Figure 4.19 (a) SEM image showing the central part of a nearly zero detuned coupled PhC nanobeam cavities (Sample B) with measured widths of the nanobeams annotated. (Note: The movable nanobeam cavity accidentally collapsed to the fixed one after the experiment, causing an irreversible stiction of the two cavities) (b) Measured wavelengths of the third order supermodes as functions of the cavity center-to-center lateral offset for Sample B. (c) Calculated relationship between the third order resonance wavelength and the coupling strength for Sample B. (d) Corresponding transmission spectra recorded at different cavity center-to-center lateral offsets (d = 62 nm, 113 nm, 156 nm, 166 nm, 209 nm, and 257 nm, respectively from top to bottom) of Sample B.

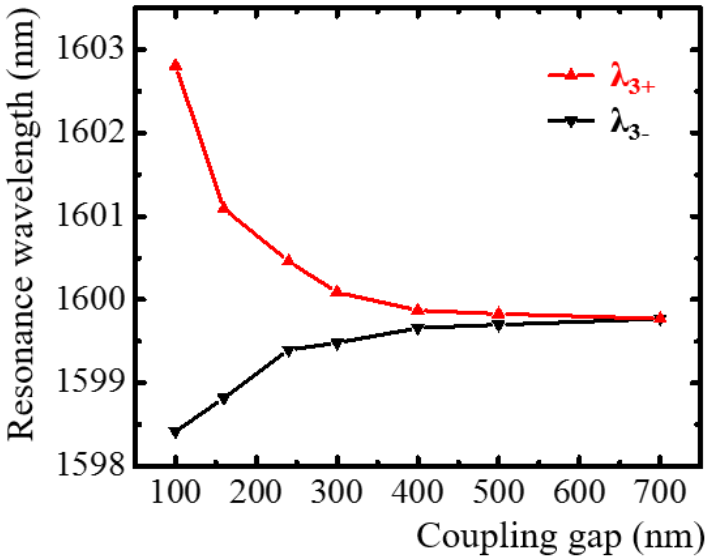

Figure 4.20 FDTD simulation results of coupling gap tuning of coupled PhC nanobeam cavities: resonance wavelength variations of a pair of supermodes as functions of the coupling gap.

For comparison, it should be noted that, by comparison, it is not possible to change the sign of the coupling strength with the traditional coupling gap tuning approach [92, 95, 195]. For traditional coupling gap tuning of coupled PhC nanobeam cavities, the cavities' center-to-center lateral offset is kept at zero, while the gap between the two cavities varies. The resonance wavelength shifts and mode field distribution variations of a pair of supermodes of the coupled PhC nanobeam cavities are calculated when the coupling gap increases using 3D FDTD simulations. As shown in Fig. 4.20, the strong coupling between the two PhC nanobeam cavities leads to mode splitting and the splitting width decreases as the gap increases. When the gap is large enough (> 500 nm), the mode splitting disappears, corresponding to the weak coupling regime. During the coupling gap tuning process, the even mode always has a longer wavelength while the odd mode always has a shorter wavelength, which indicates that the sign of the coupling

strength and mode parity do not inverse (see Fig. 4.21). Furthermore, in order to tune the coupling strength to zero, the coupling gap has to increase by more than 400 nm, which requires a much larger displacement compared with the lateral tuning method described in this thesis (~155 nm).

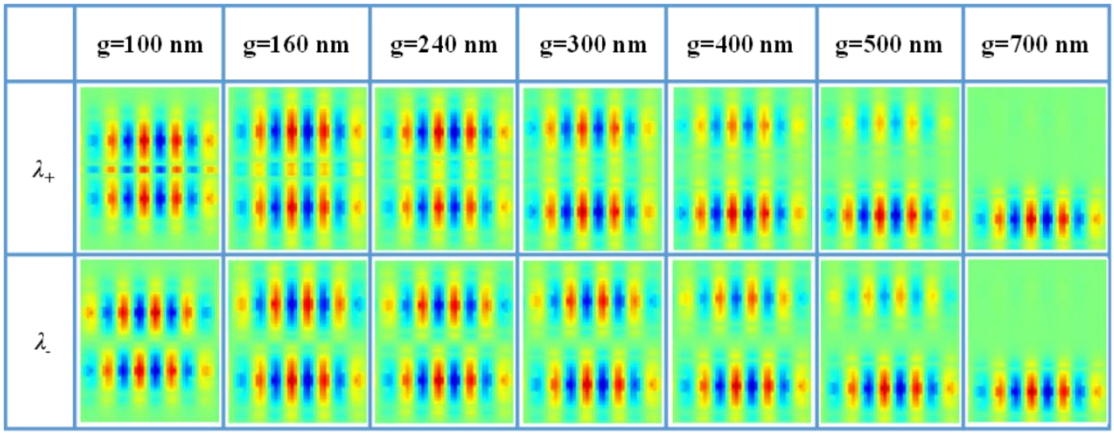

Figure 4.21 FDTD simulation results of coupling gap tuning of coupled PhC nanobeam cavities: supermode profiles at different coupling gaps corresponding to the data in Fig. 4.20.

Besides having a relatively large range from negative to zero and further to positive, the tuning of the coupling strength in this proposed device is also reversible. To demonstrate this, the applied voltage on the NEMS actuator is repeatedly tuned upwards and downwards and the corresponding resonance wavelength shifts are obtained. As shown in Fig. 4.22, the wavelength of the second order λ_- supermode for example exhibits first a red shift when the applied voltage is increasd, and returns to the initial value when the voltage reverts to zero. The maximum wavelength standard deviation recorded at each voltage is less than 4.8 pm (i.e. the standard deviation of mode splitting width $\Delta\omega$ is less than 3.8 GHz), which indicates that the coupling strength standard deviation is less than 1.9 GHz ($|\kappa| \approx \Delta\omega/2$). Therefore, the integrated NEMS actuator is

able to control the coupling strength of the coupled PhC nanobeam cavities with a precision of smaller than 2 GHz over a range of several THz.

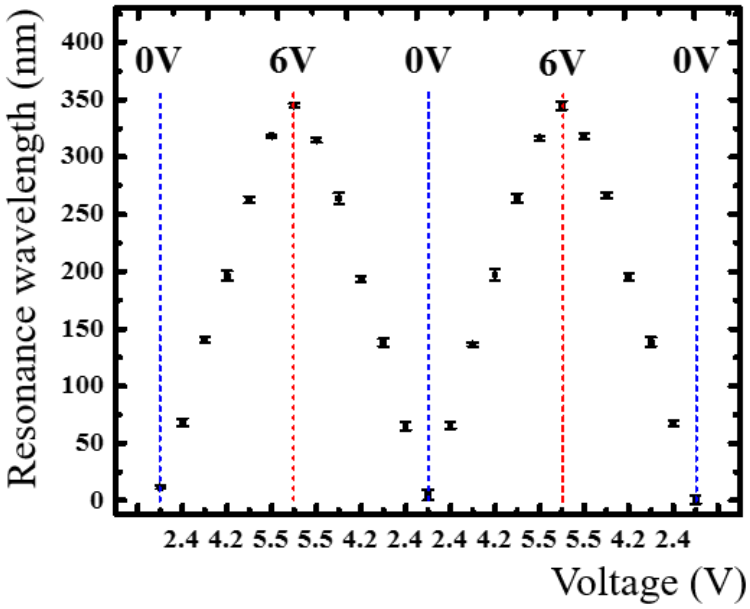

Figure 4.22 Mode wavelength shifts with repeated variations of applied voltage on the NEMS actuator. The error bar at every voltage value indicates the standard deviations of mode wavelength, obtained by repeating measurements for four times.

Dynamic performance of the proposed coupling strength control of the coupled PhC nanobeam cavities is determined by its integrated NEMS actuator, whose frequency response is measured and shown in Fig. 4.23(a). To measure the frequency response of the integrated NEMS actuator, a network analyzer is employed to scan the frequency of an AC voltage of fixed amplitude that is applied to the NEMS actuator. The laser wavelength is fixed at the half maximum position of a selected resonance mode of the coupled cavities. The transmitted light intensity is detected by the photodetector and its electric output signal is monitored by the network analyzer. The amplitude results are normalized by the maximum value.

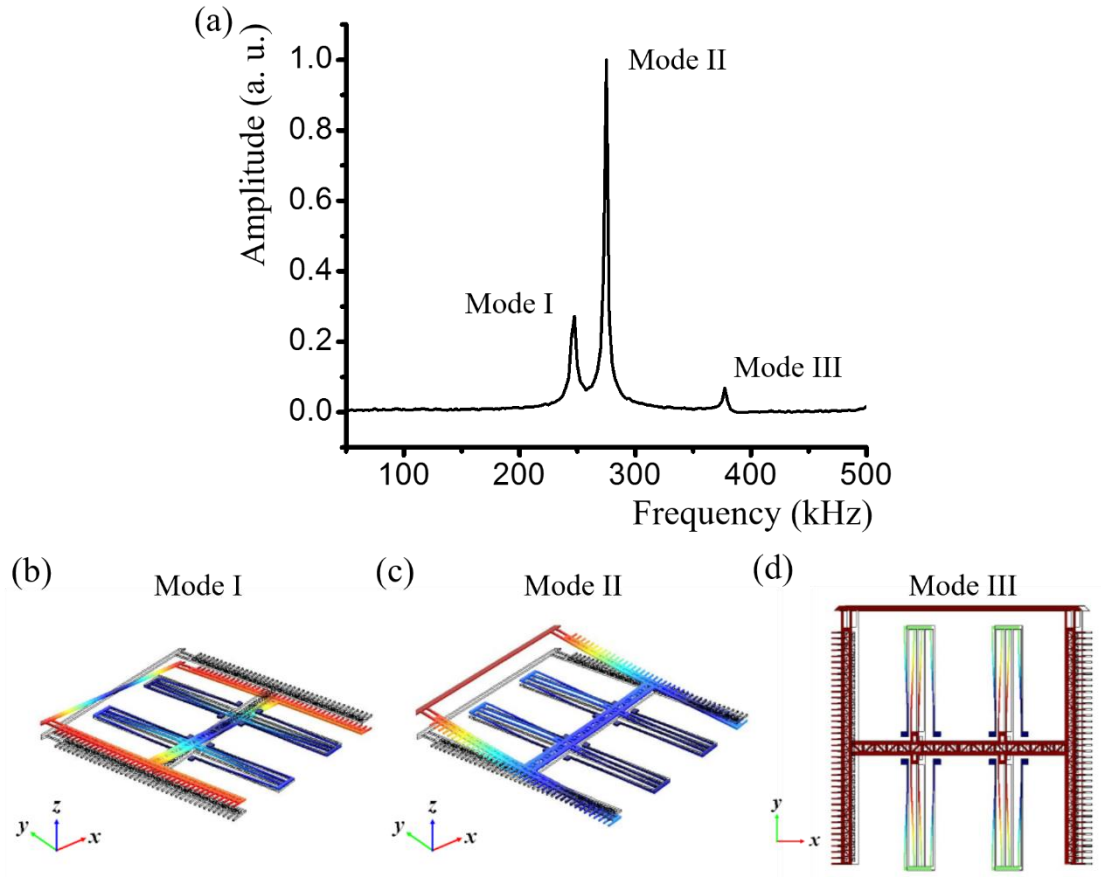

Figure 4.23 (a) Measured frequency response of the NEMS actuator. The lowest three mechanical vibration modes are observed, which are respectively denoted by Mode I (248 kHz), Mode II (275 kHz), and Mode III (378 kHz). The simulated mode shapes using FEM are shown in (b) for Mode I, (c) for Mode II, and (d) for Mode III, respectively.

Three lowest mechanical vibration modes of the actuator are experimentally recorded in the frequency range from 200 kHz to 400 kHz. They are identified and match well with the simulation results obtained from the finite element method (FEM). According to the simulated mode shapes shown in Figs. 4.23(b), (c), and (d), Mode I is the fundamental vibration mode of the NEMS actuator at 248 kHz and Mode II is the second order mode at 275 kHz. They are out-of-plane twisting modes about the *y*- and *x*-axes, respectively. Mode III is the third order vibration mode at 378 kHz and is an in-

plane translational mode that leads to the lateral displacement of the movable cavity along the *x*-axis. These results indicate that the coupling strength of the coupled PhC naobeam cavities can be dynamically controlled with a fast response time, at the microsecond level. Further reduction of the response time is possible through NEMS structural designs, for example, by decreasing the actuator size and increasing the suspension spring constant.

4.4.3 Discussion

This study investigated the lateral shearing tuning of dual-coupled PhC nanobeam cavities and experimentally demonstrated the precise control of the coupling strength between photon molecules (PhC cavities) using integrated NEMS. The coupling strength can be dynamically adjusted with a precision of a few GHz over a range of several THz without altering the nature of their constituent cavities. Moreover, both negative and positive coupling strengths are experimentally realized. The control of coupling strength in photonic molecules is crucial both in the fundamental study of cavity quantum electrodynamics and the development of efficient quantum information devices [196]. This work paves a way to optimize the coupling strength in photonic molecules *in situ*, which provides a feasible platform for the study of the strong interaction in quantum emitter-embedded photonic molecule systems [197]. By precisely tuning the coupling strength between photonic molecules, one is able to control the interaction between the quantum emitters that are individually embedded in

the two nanocavities of the photonic molecule and thus the entanglement generation [198-200]. In single photon devices that are based on photonic molecules, the single photon statistics can be improven by tailoring the coupling strength [114]. The spontaneous symmetry breaking in photonic molecules, which is quite sensitive to the coupling strength, can also be achieved with the proposed method [115]. Moreover, the fine tuning of coupling strength may also facilitate the study of Josephson physics in a photonic molecule [116, 201].

Chapter 5. Lateral Shearing Optical Gradient Force in Coupled Photonic Crystal Nanobeam Cavities

This chapter studies a novel lateral shearing optical gradient force in coupled photonic crystal nanobeam cavities. The study is proposed based on the results introduced in Chapter 4. Such force is measured in static mode and a special measuring method is proposed and employed here. The theory of optical force is first briefly discussed and then the device design is introduced. At the end, experimental results are presented and discussed. The demonstrated optical force has potential applications in, for example, nanooptoelectromechanical systems (NOEMS).

5.1. On-chip Optical Gradient Force

The previous chapter discusses the resonance tuning by relative displacing of coupled PhC nanobeam cavities. One can find that the resonance frequency varies with mechanical movement of one of the cavities. It is also noted that the on resonance light potential energy in the coupled resonators system is proportional to the resonance frequency. In this way, the system energy will vary with respect to mechanical displacement, and thus optical force can be predicted. Note that generally

$$F = -\frac{dU}{dx} \tag{5.1}$$

where dU and dx denotes the system potential energy change and mechanical

displacement in differential form, respectively; and *F* denotes the resultant force. In an optical resonant system, the optical gradient force can be written as [202]

$$F_{opt} = -\frac{dU_{opt}}{dx}\bigg|_{\mathbf{k}} = -\frac{d(N\hbar\omega)}{dx}\bigg|_{\mathbf{k}} = -N\hbar\frac{d\omega}{dx}\bigg|_{\mathbf{k}} = -\frac{1}{\omega}\frac{d\omega}{dx}\bigg|_{\mathbf{k}} U_{opt} \tag{5.2}$$

where U_{opt} denotes the light energy in system; **k** is the wave vector; *N* is the photon number; ω denotes the pumping frequency; $\hbar$ is the Planck constant. It is noted that the term $d\omega/dx$ is the optomechanical coupling coefficient g_{om}. Therefore, the equation can be expressed as

$$F_{opt} = -U_{opt} g_{om} / \omega \tag{5.3}$$

Such optical gradient forces have already been demonstrated on coupled waveguides and proven to be bipolar [24, 25]. The direction of the force depends on the mode symmetry and thus for a coupled waveguides system the mode symmetry has to be manipulated, for example, by controlling the input phase difference with a Mach–Zehnder interferometer (MZI) [24]. Yet, in a dual-coupled PhC nanobeam cavities system with inherent even-like and odd-like supermodes, the mode symmetry is easy to control by selectively pumping on one of the supermodes.

Conventional studies of the optical gradient force generated by coupled PhC nanobeam cavities mainly focus on the force with its direction perpendicular to the cavity beam [131, 202]. The resonance tuning based on the variation of the coupling gap in such

coupled cavities system has been discussed and it is reasonable to predict the optical gradient force in the direction of the gap variation. However, as can be seen from the results of the previous chapter, the lateral tuning also results in resonance frequency shift. Thus, there should be an optical force in the lateral direction as well.

In this chapter, the shearing optical gradient forces in the lateral direction are investigated. Such forces are achieved in a NEMS-controlled dual-coupled PhC nanobeam cavities system.

5.2. Device Design and Testing

The device designed and developed for the study described in this chapter is similar to those in Chapter 4. An SEM image of the device is given in Fig. 5.1(a).

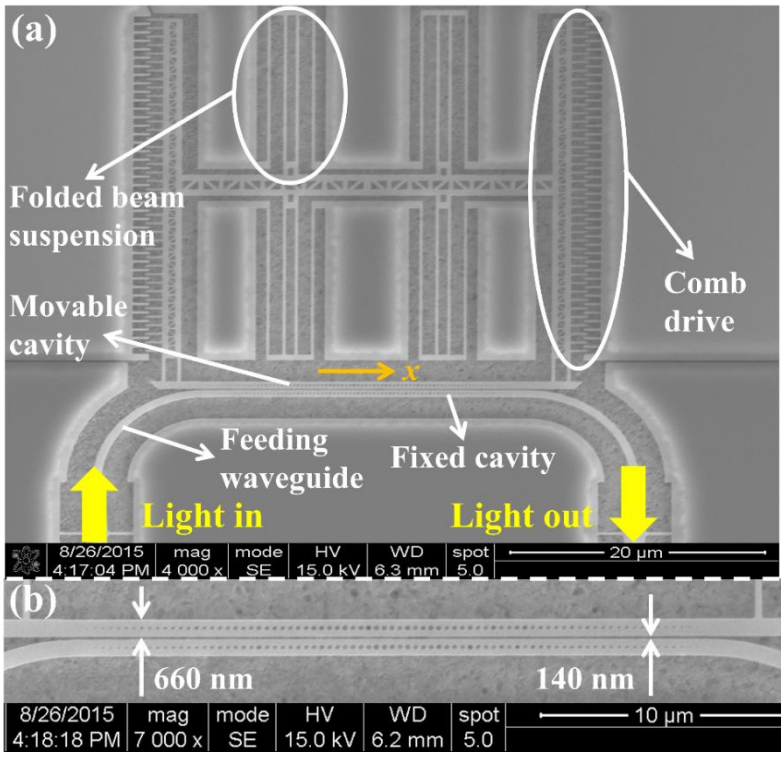

Figure 5.1 (a) Global-view SEM image of the device and (b) local close-up view showing dual-coupled PhC nanobeam cavities.

As shown, one of the dual-coupled PhC nanobeam cavities is fixed and connected with the silicon nanowire feeding waveguides. The other cavity is supported by four folded-beam suspensions and is movable with the integrated NEMS comb drive along the lateral direction (*x* direction as indicated). With a voltage applied across the movable and fixed fingers, the electrostatic force generated by the NEMS comb drive shifts the movable cavity to a position where the electrostatic force is balanced by the mechanical restoring force generated from the folded-beam suspensions. The cavity nanobeam measures 660 nm in width and the gap between the coupled cavities is about 140 nm, as shown in Fig. 5.1(b). The PhC lattice period keeps constant at 310 nm and the air-hole diameters are quadratically tuned from 210 nm at the center to 60 nm at either end after 39 holes. More specifically, the radius of the air-holes r_n, (n changes from 1 to 40, denoting the number of holes from the center to either end of the cavity) is given by: $r_n=r_1\times(1-(r_1-r_{40})/r_1\times((n-1)/39)^2)$, where r_1 is 210 nm and r_{40} is 60 nm.

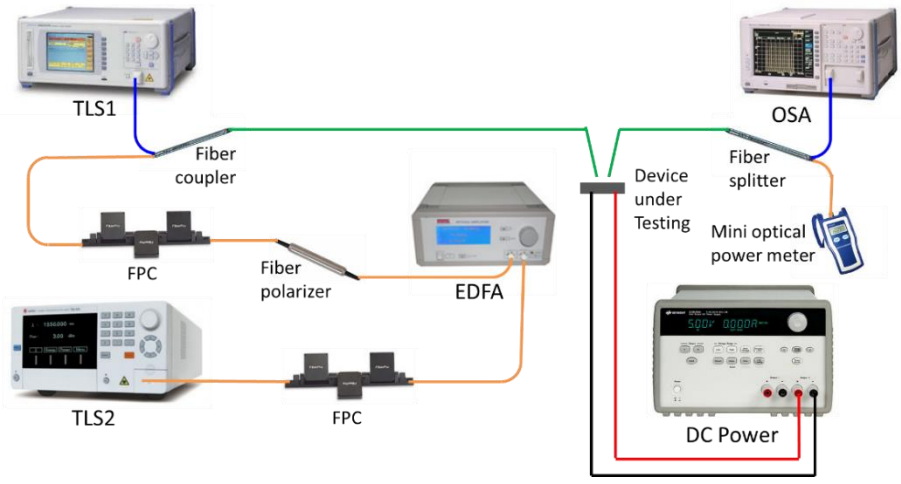

Figure 5.2 Schematic of the testing setup to measure the lateral shearing optical gradient force.

The testing setup is illustrated in Fig. 5.2. Two tunable laser sources TLS1 and TLS2

are utilized, with light generated from TLS2 amplified by an erbium doped fiber amplifier (EDFA) used for pumping the lateral shearing forces. The polarization of the pumping laser beam is controlled by a fiber polarizer (FP) and two fiber polarization controllers (FPC) to excite the transverse electric (TE)-like modes in the device. TLS1 provides the probing light for force detection and is synchronized with an optical spectrum analyzer (OSA) to scan over a specific wavelength range. A very small probing laser power (about three orders of magnitude smaller than that of the pumping light) is used such that both its thermo-optical and optomechanical effects can be ignored. Before launching into the device, the probing and pumping light are combined using a fiber coupler. The device output signals are monitored by both an OSA and an optical power meter. A DC power supply is used to drive the integrated NEMS comb drive to mechanically adjust the movable cavity laterally for calibration purpose as well as for setting up the initial cavity center-to-center offset for lateral optical force experiments.

5.3. Results and Discussion

5.3.1. Experimental results

The measured optical spectrum at the initial condition without any cavity center-to-center lateral offset is plotted as the black curve in Fig. 5.3.

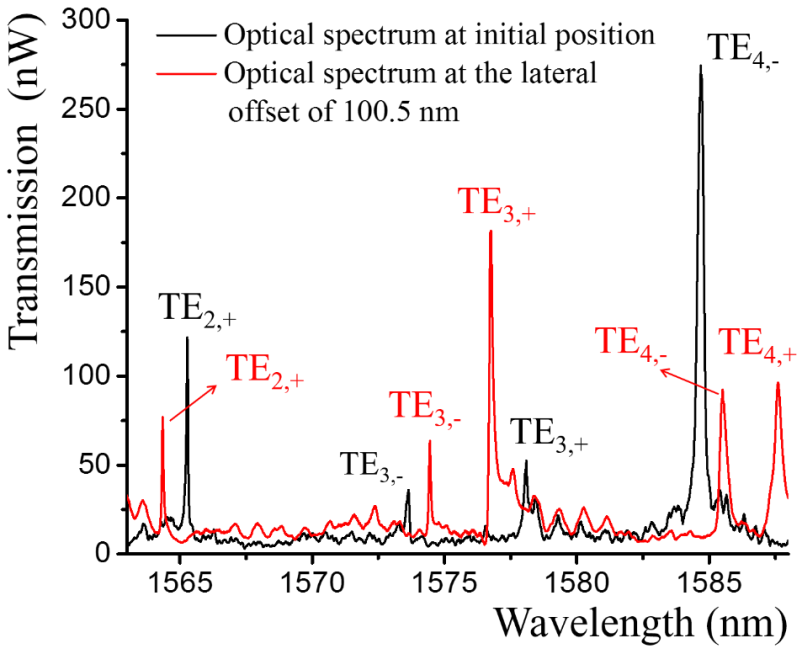

Figure 5.3 Measured optical spectra of the device at initial position with zero cavity center-to-center offset (black curve) and at the offset of 100.5 nm (red curve), where resonance modes are marked.

As shown, four resonance peaks are recorded and they are the second order λ_+ mode ($TE_{2,+}$), third order λ_- ($TE_{3,-}$) mode, third order λ_+ mode ($TE_{3,+}$), and fourth order λ_- ($TE_{4,-}$) mode (λ_+ and λ_- respectively denote the longer and shorter wavelength modes in a split pair due to mode coupling). They are located at 1565.272 nm, 1573.603 nm 1578.096 nm, and 1584.726 nm with their Q factors of about 22100, 8600, 8900, and 3800, respectively. 3D FDTD simulation based on the SEM-measured coupled cavities dimensions is conducted to help the identification of the measured resonance modes. The simulation results show that the $TE_{2,+}$ mode locates at 1558.84 nm with a Q factor of 10800, $TE_{3,-}$ locates at 1571.54 nm with a Q factor of 15000, $TE_{3,+}$ locates at 1575.08 nm with a Q factor of 15500, $TE_{4,-}$ locates at 1585.22 nm with a Q factor of 14700, $TE_{4,+}$ locates at 1588.87 nm with a Q factor of 15000. Slight mismatches between the

experimental and simulation results might be due to the measurement errors and numerical inaccuracies. The simulated electric field profiles of the $TE_{4,-}$ and $TE_{4,+}$ modes at the initial zero cavity center-to-center offset are plotted in Figs. 5.4(a) and (c), respectively.

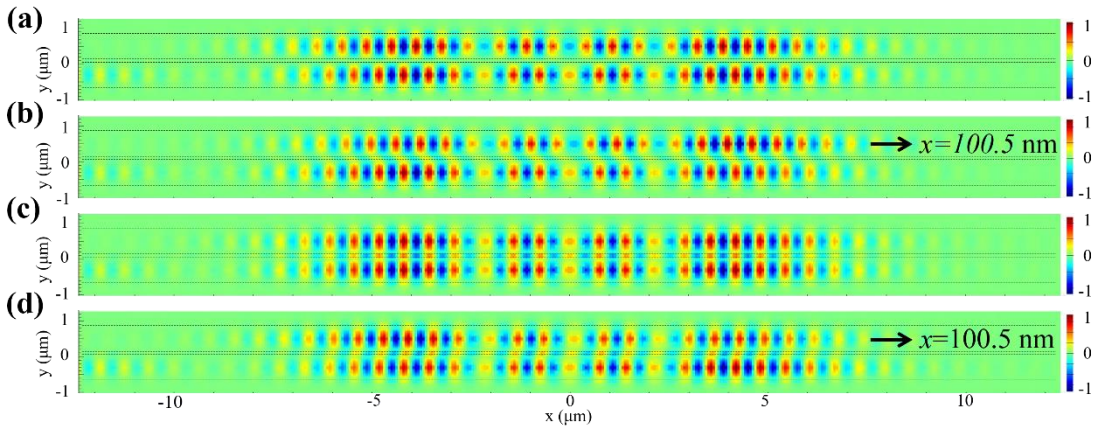

Figure 5.4 3D FDTD-simulated mode profiles of the (a) $TE_{4,-}$ and (c) $TE_{4,+}$ mode at zero center-to-center offset and mode profiles of the (b) $TE_{4,-}$ and (d) $TE_{4,+}$ mode at 100.5 nm offset.

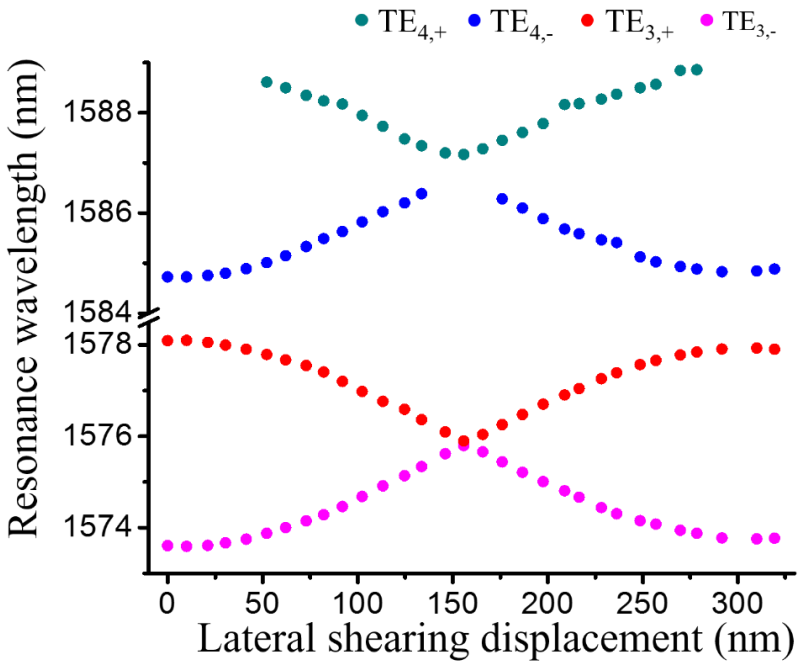

Figure 5.5 $TE_{3,-}$, $TE_{3,+}$, $TE_{4,-}$, and $TE_{4,+}$ mode resonance wavelength tuning results by laterally shifting the movable cavity.

In experiments, the resonance tuning characteristics are firstly calibrated by laterally shifting the movable cavity with the integrated NEMS comb drive actuator. The results are given in Fig. 5.5. Despite a few missing data points due to the failure to detect the resonance at some displacements, which may be due to some unknown factors in our experimental system that affect the light coupling efficiencies and cavity losses at those lateral displacements, the mode splitting generally demonstrates a periodic pattern as a function of the lateral displacement. One can refer to Chapter 4 to get a better understanding of the resonance characterization. Considering a coupled system consisting of two identical resonators, the resonance frequencies of a split pair of modes are given by $\omega_0 \pm |\kappa|$, where ω_0 is the natural frequency of the individual resonator and κ denotes the coupling strength between them. The lateral displacement of one cavity with respect to the other changes the mode field overlap integral of the two cavities and thus varies the coupling strength between them. At initial condition when the two cavity centers and optical modes are perfectly aligned, the absolute value of the coupling strength is the largest and consequently, the width of mode splitting is at its maximum. The coupling strength decreases gradually when the movable cavity is displaced laterally by the NEMS comb drive. When it shifts for half a PhC lattice period, the optical mode field overlap integral is at the minimum and so do the coupling strength and mode splitting width. In experiments, the measured minimum mode splitting of the third-order modes is only about 100 pm at a lateral shift of a half PhC period (~155 nm). With continued shifting and increasing of the cavity center-to-center lateral offset, the

coupling strength and mode splitting width increase again. The mode splitting width reaches a local maximum when the lateral shift of one cavity is about a PhC lattice period with respect to the other.

In experiments, the DC voltage applied to the NEMS comb drive was gradually increased to shift the movable cavity laterally and the resonance wavelength of the coupled cavities recorded at each applied voltage. It is known that the relation between the displacement of the NEMS comb drive and voltage applied is $x = c \times V^2$ where c is a constant determined by the actuator design (see Eq. (4.30) and Eq. (4.31)). Here, a voltage of 13.4 V is required to change the mode splitting width from the initial maximum to the next local maximum, which indicates that the NEMS comb drive moves about a PhC lattice period of 310 nm. In this way, the comb drive is precisely calibrated, i.e. $x = 1.726 \times V^2$ with x being the lateral displacement in nm and V being the voltage in Volts. The lateral displacement values for the horizontal axis in Fig. 5.5 are then accurately obtained from the NEMS driving voltages.

From Fig. 5.5, the optomechanical coupling coefficients g_{om} ($g_{om} = d\omega/dx$) can be estimated, which is defined as the derivative of the cavity resonant frequency with respect to mechanical deformation (lateral mechanical displacement of the movable cavity in this study). It is also noted that the optical gradient force can be estimated by Eq. (5.3). Hence, lateral shearing optical gradient forces are expected to exist in the proposed device. As can also be seen from Fig. 5.5, the slopes of the curve at the initial condition ($x = 0$ nm) are close to zero

indicating the near-zero optomechanical coupling coefficients g_{om} at this position and hence no lateral shearing forces exist when optically pumped. In experiments to generate the lateral shearing forces, the movable cavity is adjusted to a center-to-center offset of 100.5 nm, where the slopes of the wavelength-displacement curves are relatively steep, resulting in relatively high g_{om}. The experimental spectrum at the 100.5 nm offset is given by the red curve in Fig. 5.3. Five resonance modes are detected and marked. They are located at 1564.354 nm ($TE_{2,+}$), 1574.449 nm ($TE_{3,-}$), 1576.758 nm ($TE_{3,+}$), 1585.524 nm ($TE_{4,-}$), and 1587.617 ($TE_{4,+}$), with their *Q* factors measured to be about 24400, 17400, 8000, 5100 and 4800, respectively. The $TE_{4,-}$ and $TE_{4,+}$ modes are selected as the pumping modes, while the $TE_{3,-}$ and $TE_{3,+}$ modes are selected as the probe modes due to their high *Q* factors. At this offset configuration, the mode field profiles of the $TE_{4,-}$ and $TE_{4,+}$ modes used for pumping the optical forces are simulated with 3D FDTD and plotted in Figs. 5.4(b) and (d) respectively, in which the shearing of the optical mode fields can also be observed.

The total resonance wavelength detuning of the coupled cavities due to mechanical deformation by optical gradient force and thermo-optical effect by absorption-induced temperature change can be written as

$$\Delta\lambda = d_{om}F_{opt} / k + d_{to}\Delta T \tag{5.4}$$

where k is the total spring constant of the folded beam suspensions in the x direction, $d_{om}=d\lambda/dx$ denotes the opto-mechanical wavelength detuning coefficient ($d_{om}/\lambda = -g_{om}/\omega$), $d_{to}=d\lambda/dT$ denotes the thermo-optical wavelength detuning coefficient, and ΔT is the temperature change.

To decouple the thermo-optical effect from the optomechanical effect, the author considers the mode splitting width of a pair of split modes from the same order

$$\Delta\lambda^{+} - \Delta\lambda^{-} = (d_{om}^{+} - d_{om}^{-})F_{opt} / k + (d_{to}^{+} - d_{to}^{-})\Delta T \tag{5.5}$$

Assuming that the thermo-optical effects of the λ_{+} and λ_{-} modes are the same [195] ($d^{+}_{to} = d^{-}_{to}$), Eq. (5.5) can be rewritten as

$$\Delta(\lambda^{+} - \lambda^{-}) = (d_{om}^{+} - d_{om}^{-})F_{opt} / k \tag{5.6}$$

$$F_{opt} = \Delta(\lambda^{+} - \lambda^{-})k / (d_{om}^{+} - d_{om}^{-}) \tag{5.7}$$

Hence, with the coefficients d^{+}_{om} and d^{-}_{om} known experimentally from the resonance tuning results using the integrated NEMS and spring constant calculated using FEM, the lateral shearing optical forces can be detected by monitoring the split width variation of the probe modes when the device is optically driven by the pumping modes. It is also noted that there may exist other resonance detuning effects, for example, Kerr effect and effective index perturbation. However, they are usually relatively small as compared with the opto-mechanical and thermo-optical effects. Furthermore, they can also be decoupled from the optical force induced opto-mechanical effect by measuring the split width of a pair of supermodes if their effects on these modes are identical.

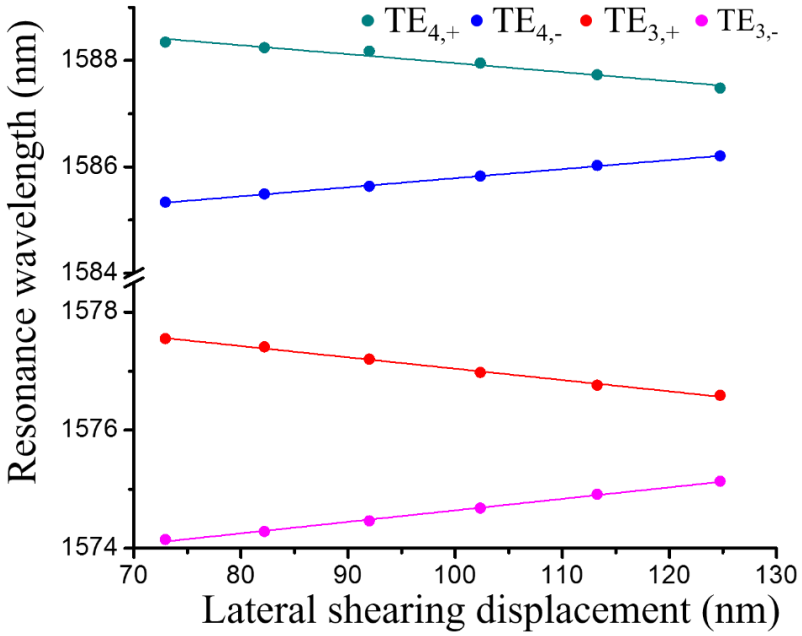

Figure 5.6 $TE_{3,-}$, $TE_{3,+}$, $TE_{4,-}$, and $TE_{4,+}$ resonance wavelength tuning results near the offset of 100.5 nm. The dots are measured data and the lines are their individual linear fitting.

The resonance wavelength tuning results near the 100.5 nm offset are plotted in Fig. 5.6. The opto-mechanical wavelength detuning coefficients d_{om} of these four resonances are obtained by linearly fitting the results and their slopes are 0.01947 ($TE_{3,-}$), -0.01917 ($TE_{3,+}$), 0.01701 ($TE_{4,-}$), and -0.01688 ($TE_{4,+}$), respectively. These data are measured with an extremely low input laser power to ensure that the thermo-optical and opto-mechanical effects are negligible.

$TE_{4,+}$ and $TE_{4,-}$ modes are then pumped respectively with a constant laser power of 135 mW output from the EDFA. Taking the losses in the setup and coupling efficiencies of the grating couplers into consideration, the launching laser power in the waveguide just before the cavities is estimated to be less than 1 mW. At the selected cavity center-to-center offset of 100.5 nm, their measured transmission spectra are obtained and plotted in the insets in Fig. 5.7 and Fig. 5.8, respectively.

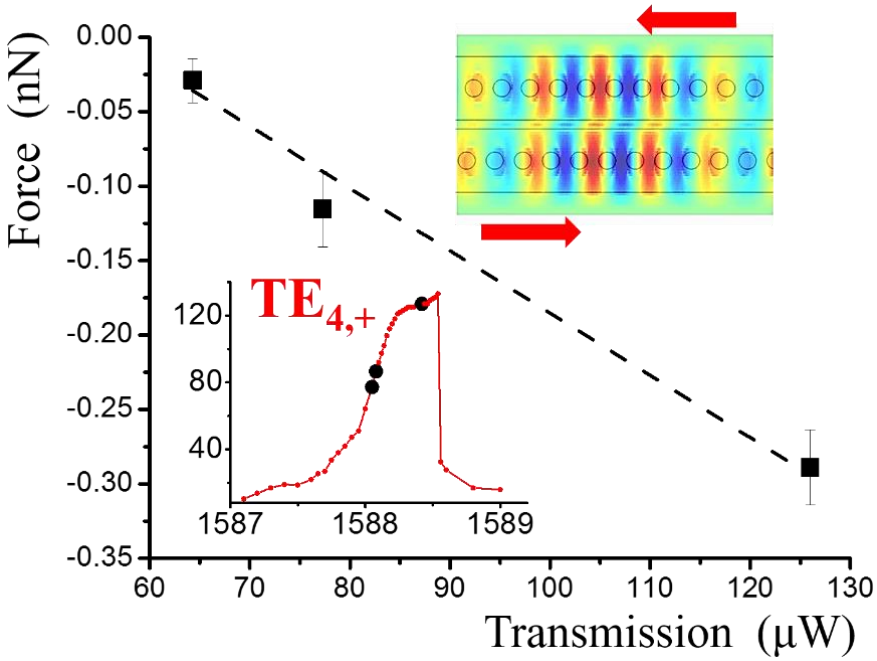

Figure 5.7 Measured lateral shearing optical gradient force pumped by $TE_{4,+}$ modes with different recorded transmission powers. The insets show their respective transmission spectra (*x*-axis denotes wavelength in nm and *y*-axis denotes transmission in μW) used for pumping.

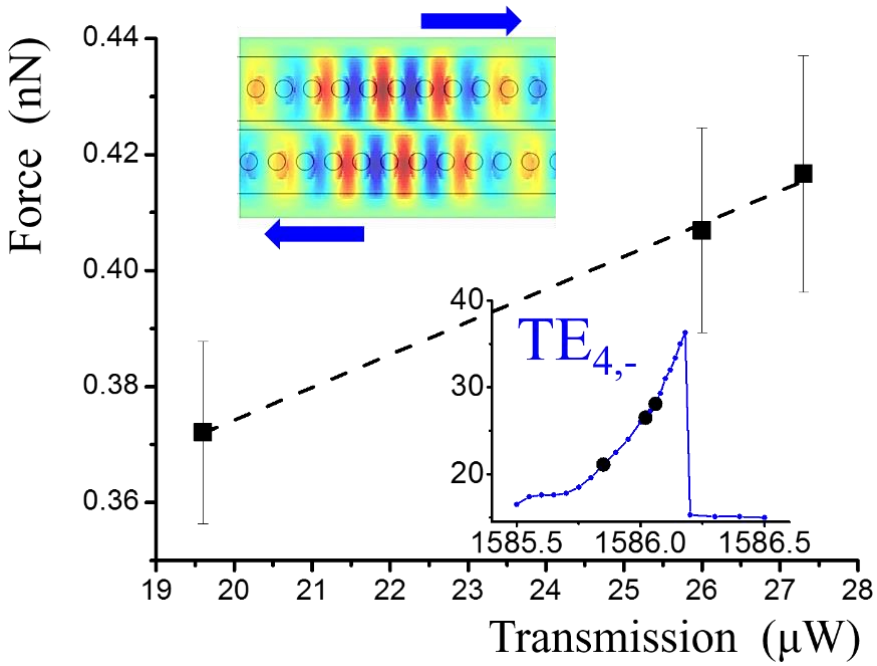

Figure 5.8 Measured lateral shearing optical gradient force pumped by $TE_{4,-}$ modes with different recorded transmission powers. The insets show their respective transmission spectra (*x*-axis denotes wavelength in nm and *y*-axis denotes transmission in μW) used for pumping.

Strong nonlinearities are observed, which are attributed to both thermo-optical and opto-mechanical effects at high pumping powers [203]. Several near-resonance wavelengths (marked as black dots on the two resonance curves) are selected as the pumping wavelengths. At the same time, a low power probe laser beam from TLS1 synchronized with the OSA scans a spectral range that covers the $TE_{3,-}$ and $TE_{3,+}$ resonances and the spectrum is recorded over ten times for each pumping condition. The variations of the mode splitting width are then detected and the lateral shearing optical forces are estimated with Eq. (5.7) and plotted in Fig. 5.7 and Fig. 5.8, respectively for $TE_{4,+}$ and $TE_{4,-}$ modes. The shearing force directions are also illustrated in their respective insets together with the central part of the mode profiles. For $TE_{4,+}$ pumping, the g_{om} is positive and the force is negative pulling the two cavity centers together, whereas the g_{om} is negative and the force is positive pushing the centers apart for $TE_{4,-}$ pumping. In addition, the force magnitude increases as the light energy inside the coupled cavities rises (as indicated by increasing transmission) as expected.

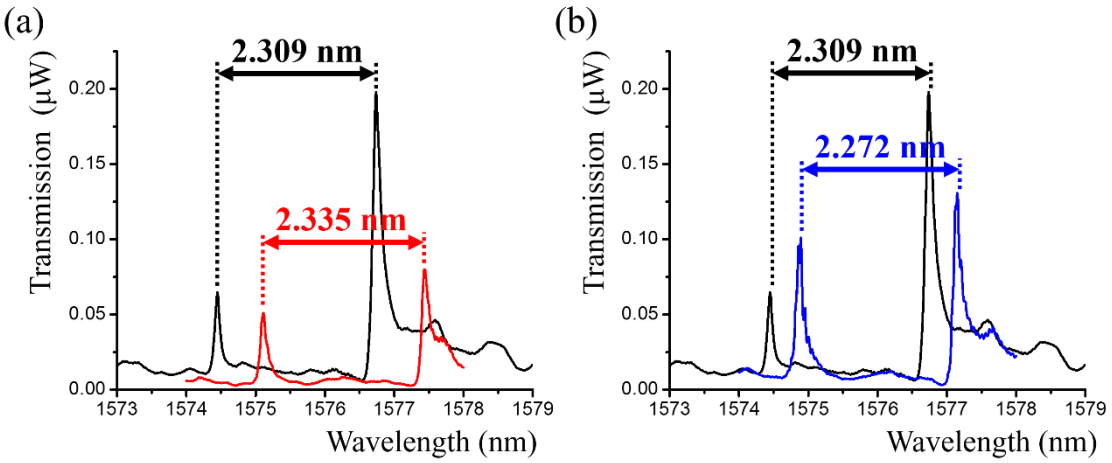

Figure 5.9 The variation of the mode splitting width of the probing $TE_{3,-}$ and $TE_{3,+}$ modes when pumped by (a) $TE_{4,+}$ and (b) $TE_{4,-}$ modes. The black curves show the reference resonances without pumping while the color ones show the resonances

obtained under pumping effect.

Typical mode split width variations are elaborated in Figs. 5.9(a) and (b), where the black curves represent the initial $TE_{3,-}$ and $TE_{3,+}$ modes without pumping as references while the color curves show the same modes when the pump laser beam is turned on. Pumped by $TE_{4,+}$ mode at 1588.4 nm wavelength (laser power transmitted through the device is measured at 126 μW), the resonance peaks of the probing $TE_{3,-}$ and $TE_{3,+}$ modes are shown by the red curve in Fig. 5.9(a). As can be seen, both resonances redshift about 650 pm, indicating that the thermo-optical effect dominates when pumped. It is also observed that the mode split width changes to 2.335 nm from the initial 2.309 nm without the pump beam. This increase of the mode split width is caused by the negative shearing optical gradient force pulling the centers of the two cavities laterally towards each other. The force magnitude is estimated to be 0.29 nN from Eq. (5.7). Similarly, the blue curve in Fig. 5.9(b) shows the $TE_{3,-}$ and $TE_{3,+}$ modes when pumped by the $TE_{4,-}$ mode at 1586.04 nm wavelength (transmitted laser power measured at 27.3 μW). The mode split width decreases by 37 pm from 2.309 nm to 2.272 nm, indicating that a positive shearing optical gradient force of 0.42 nN is pushing the two cavity centers apart laterally.

5.3.2. Discussion

In summary, the lateral shearing optical gradient force in a NEMS-controlled dual-coupled PhC nanobeam cavities system is experimentally demonstrated. The coupled cavities are tuned to a selected lateral center-to-center offset for force generation. Through measurement of the

variations in the resonance wavelength split width, the opto-mechanical effect is decoupled from the thermo-optical effect and thus the optical forces are quantified. The detected shearing optical forces are at the scale of sub-nano Newtons, which is relatively small compared with the electrostatic forces generated from the on-chip integrated NEMS comb drives (~ 40 nN at 10 V). However, such optical forces require a much smaller device footprint, are bipolar in nature and can be significantly enhanced through increase in incident laser power. Such lateral shearing optical forces may further increase the potential applications of nano optomechanics and may be useful in future NOEMS systems, such as optically-driven tunable filters, all-optical switches, and optically-reconfigurable photonic circuits.

Chapter 6. Tunable Cavity Optomechanics in Dual-coupled Photonic Crystal Nanobeam Cavities

In this chapter, an optomechanics tuning method is proposed and experimentally demonstrated in dual-coupled photonic crystal nanobeam cavities. The tuning is based on the coupling gap variation of the coupled cavities. The theory of cavity optomechanics is briefed at the beginning. Then the tuning method and device design are introduced. At the end, the experimental results are elaborated upon and discussed. The study in this chapter fills the gap of tunable cavity optomechanics among published literatures and paves a way for potential applications of mechanical motion controlling and measurement based on cavity optomechanics.

6.1. Cavity Optomechanics and Proposed Tuning Method

As introduced in Chapter 1 and Chapter 2, optical force has the capability to amplify or suppress mechanical oscillation derived from optomechanical coupling. Additionally, mechanical resonance frequency can be shifted due to the optical spring effect [132, 204]. As reviewed in Chapter 2, numerous studies related to optomechanics have been reported, but among them, those on the tuning of optomechanics are scarce. In this chapter, optomechanics based on dual-coupled PhC nanobeam cavities is demonstrated and a tuning method, based on coupling gap variation, is proposed and experimentally investigated to fill the gap in the field of tunable optomechanics.

The author would like to start with a brief introduction to the theory of cavity optomechanics, which has been established for years [141, 142, 153]. The coupled equations to describe the coupling between mechanical degree of freedom and optical degree of freedom can be written as

$$\frac{d}{dt}p = -(i\cdot(\delta\omega - g_{om}x) + \Gamma/2)p + \sqrt{\frac{1}{\tau_w}\left|s_i^2\right|} \tag{6.1}$$

$$\frac{d^2}{dt^2}x = -\gamma_M\frac{d}{dt}x - \Omega_M^2 x - \frac{\left|p^2\right|g_{om}}{\omega_0 m_{eff}} \tag{6.2}$$

where $\delta\omega$ ($=\omega_l - \omega_0$) is the laser frequency detuning; Γ is the optical mode decay rate; $1/\tau_w$ denotes the optical input coupling rate; $|s_i|^2$ denotes the optical input energy; γ_M is the bare mechanical damping factor; Ω_M is the bare mechanical resonance frequency; m_{eff} denotes the effective mass of the mechanical resonator.

However, in practice, a thermo-optical effect is always involved. Thus a third equation should be added to describe the thermo-optical tuning of the optical resonator by introducing a new parameter ΔT, denoting the temperature change, i.e.

$$\frac{d}{dt}p = -(i\cdot(\delta\omega - (g_{om}x + g_{to}\Delta T) + \Gamma/2)p + \sqrt{\frac{1}{\tau_w}\left|s_i^2\right|} \tag{6.3}$$

$$\frac{d^2}{dt^2}x = -\gamma_M\frac{d}{dt}x - \Omega_M^2 x - \frac{\left|p^2\right|g_{om}}{\omega_0 m_{eff}} \tag{6.4}$$

$$\frac{d}{dt}\Delta T = -\gamma_{th}\Delta T + \Gamma_{abs}\left|p^2\right|c_{th} \tag{6.5}$$

where g_{to} denotes the thermo-optical detuning coefficient; Γ_{abs} is the optical decay rate due to material absorption; c_{th} is denotes the thermal heat capacity of the resonator and γ_{th} is the temperature decay rate. Using the perturbation method, the tri-coupled equations can be solved and the following results can be obtained [153].

$$(\Omega_M')^2 \approx \Omega_M^2 + \left(\frac{2|p_0|^2 g_{om}^2 \delta\omega_0}{\Lambda^2 \omega_0 m_{eff}}\right)\left[\frac{1+W}{1+s}\right] \tag{6.6}$$

$$\gamma_M' \approx \gamma_M - \left(\frac{|p_0|^2 g_{om}^2 \Gamma \delta\omega_0}{\Lambda^4 \omega_0 m_{eff}}\right)\left[\frac{1+V}{1+s}\right] \tag{6.7}$$

where

$$W = -\left(\frac{2\Delta\omega_{th}}{\Gamma}\right)\left(\frac{\gamma_{th}}{\Omega_M}\right)^2\left(\frac{\Gamma\delta\omega_0}{\Lambda^2}\right) \tag{6.8}$$

$$V = \left(\frac{2\Delta\omega_{th}}{\Gamma}\right)\left(\frac{\gamma_{th}}{\Omega_M}\right)^2\left(\frac{\delta\omega_0}{\delta\omega^2}\right) \tag{6.9}$$

$$s \approx \left(\frac{2\delta\omega_0\gamma_{th}\Delta\omega_{th}|p_0|^2}{\Lambda^2\Omega_M}\right)^2 \tag{6.10}$$

where Ω'_M and γ'_M denote the effective mechanical resonance frequency and effective mechanical damping factor due to the optomechanical coupling respectively; $|p_0|^2$ is the time-averaged energy in the system; $\Delta\omega_{th}$ is the static thermal-optical frequency tuning; $\delta\omega_0$ (= $\delta\omega$-($g_{om}x_0$ + $g_{to}\Delta T_0$)) denotes the time averaged laser frequency detuning; Λ^2 =$(\delta\omega_0)^2 + (\Gamma/2)^2$.

To be more explicit, typical relationships between the effective mechanical resonance

frequency and laser wavelength detuning are plotted in Fig. 6.1.

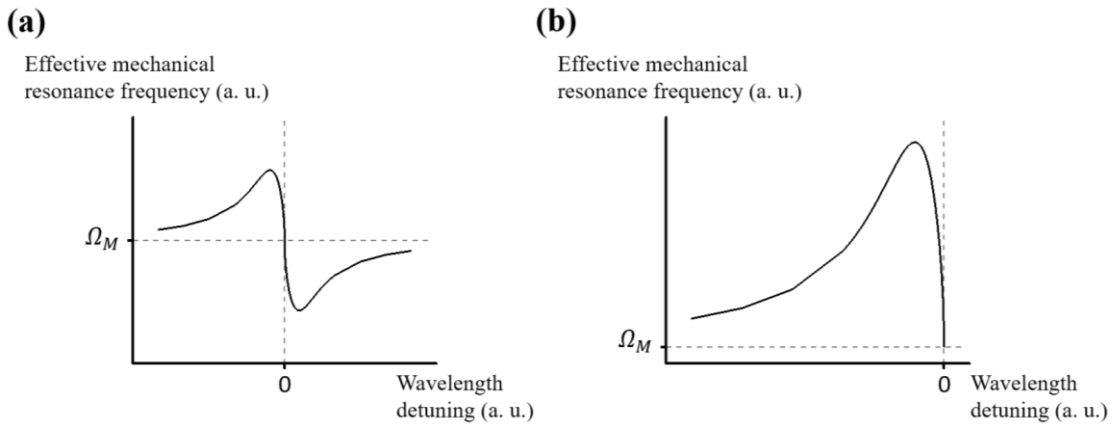

Figure 6.1 Typical relationships between the effective mechanical resonance frequency and the laser wavelength detuning: (a) the case when optical force dominates the total effect, and (b) thermo-optical effect dominates the total effect.

When the optical force dominates the total effect, the relationship will be presented as the curve in Fig. 6.1(a), whereas if the thermo-optical tuning dominates the total effect, the relationship might show up as the curve in Fig. 6.1(b).

As can be seen from Eq. (6.6) and Eq. (6.7), the mechanical oscillation parameters, resonance frequency and damping factor depend on the optical parameters, including light energy in the system, $|p_0|^2$ and optomechanical coupling coefficient, g_{om}. Thus, the optomechanics in the system can be tuned by adjusting the light energy and/or the optomechanical coupling coefficient. The optical energy can be easily changed by varying the input power generated from the laser source. As for the optomechanical coupling coefficient, it is also tunable through the electrostatic methods introduced in Chapter 4 or in reported studies [97].

In this chapter, the coupling gap variation tuning method is employed and demonstrated

to have the capability to tune the optomechanics. Though it is demonstrated in Chapter 4 that lateral tuning has higher resonance tuning performance compared with coupling gap vibration and in Chapter 5 that there exists lateral optical force, no study of optomechanics based on the lateral optical force has been reported. Thus in this chapter, the author employs the coupling gap variation tuning method and generates the optomechanics based on the optical force perpendicular to the cavity beam for the sake of caution.

6.2. Device Design and Testing

Figure 6.2 shows the SEM image of the device, which is designed based on dual-coupled PhC nanobeam cavities for the proposed tunable optomechanics. Similar to the devices described earlier, one cavity is fixed and light is launched into and out from this cavity. The movable cavity is actuated by NEMS actuators to adjust the coupling gap.

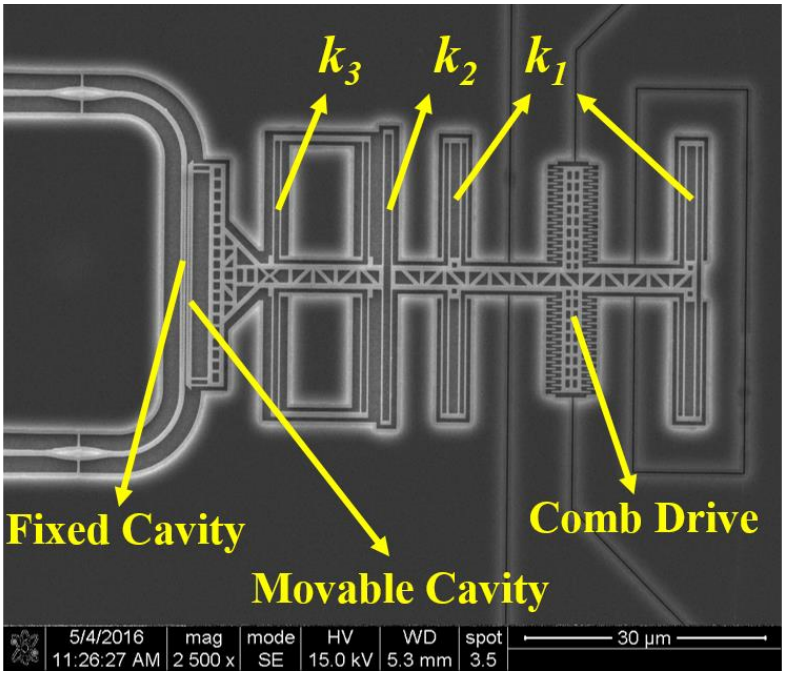

Figure 6.2 SEM image of the device to demonstrate tunable optomechanics.

There would be no actuation in the lateral direction and thus the cavity holes on the two cavity beams will be aligned throughout the experiments. It is noted that the cavities have similar dimensions to those used in Chapter 5.

It is noted that generally, the smaller the coupling gap is, the higher the optomechanical coupling coefficient g_{om} will be [95, 97, 195]. (One can also refer to the simulated results plotted in Fig. 4.20.) This is because that a smaller coupling gap results in a larger mode field overlap integral of the two cavities and thus stronger interaction between them.

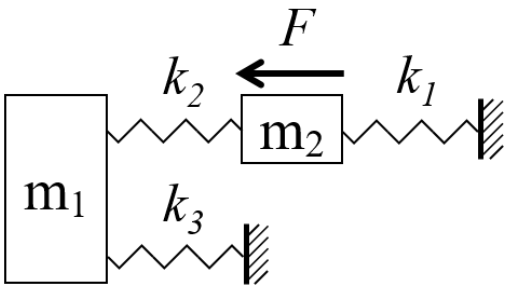

Figure 6.3 Shematic of the mechanical shrinkage mechanism.

Folded beam suspensions are also designed with a mechanical shrinkage mechanism for precise coupling gap control. As shown in Fig. 6.2, there are three components of beam suspensions, marked as k_1, k_2 and k_3. (k_1, k_2 and k_3 also denote the spring constants of these three beam suspension components.) If the movable portion of the comb drive and the movable cavity are treated as two rigid mass pieces, the equivalent mechanical configuration can be represented as in Fig. 6.3, in which the two mass pieces are denoted by m_1 and m_2, respectively. As can be seen, m_2 is connected to the fixed anchor by k_1; m_1 is connected to fixed anchor with k_3; and m_1 and m_2 are connected with each

other through k_2. In this case, when the actuation force is applied to m_2, the displacement ratio between m_1 and m_2 (d_1/d_2) can be given as

$$\frac{d_1}{d_2} = \frac{k_2}{k_2 + k_3} \tag{6.11}$$

In this device, k_2 : k_3 is designed to be 1 : 3, so the shrinkage ratio should be 1 : 4. It is noted that beams k_2 and k_3 are designed to have the same beam width, but with different lengths. In this case, even if over-etching were happened to the beams during DRIE etching, the spring constant ratio will not be affected, because the width shrinkage due to over-etch of close-spaced beams should be nearly equivalent.

6.3. Results and Discussion

6.3.1. Experimental results

An even mode of the coupled cavities is detected, as shown in Fig. 6.4. The resonance peak is fitted with a Lorentz function and is found to have a transmission of over 1.5 μW and *Q* factor of over 5000. This even mode is selected to be pumped for optomechanics. It is noted that it is usual to pump an even mode for optomechanics because compared with odd mode, an even mode has a higher optomechanical coupling coefficient and thus optical force [97, 131, 135, 136].

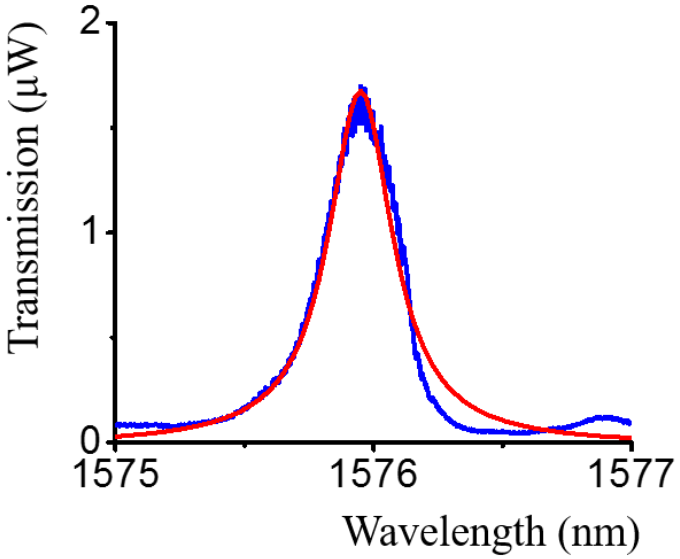

Figure 6.4 Optical spectrum (blue curve) and its Lorentz fitting (red curve) of an even mode resonance selected to be pumped for optomechanics.

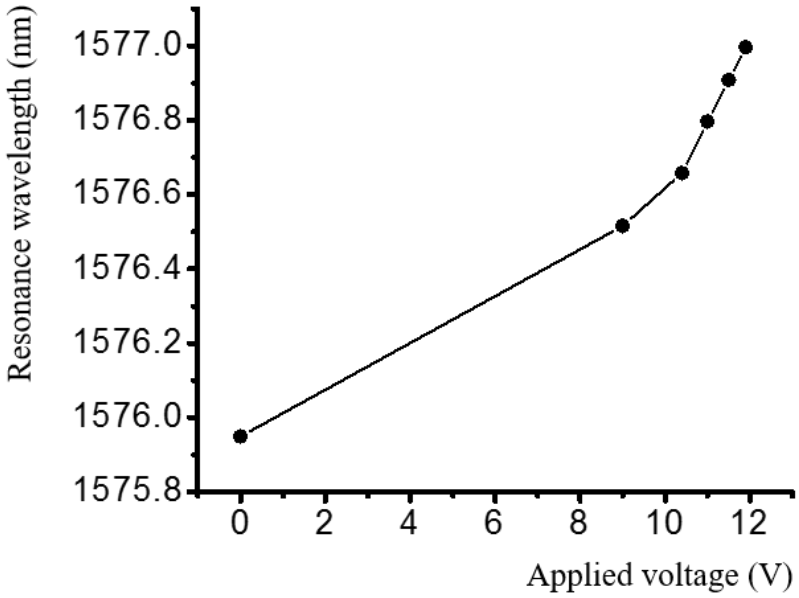

Figure 6.5 Resonance tuning results: relationship of resoance wavelength of the seleceted even mode and the voltage applied to the actuator to reduce the coupling gap.

Firstly, the resonance tuning results by reducing the coupling gap is characterized. Different driving voltages are applied to the comb drive to reduce the gap and the optical spectra are measured under different voltage steps. (The applied voltages V can be converted to coupling gaps with Eq. (4.30), Eq. (4.31) and measured initial coupling

gap (140 nm), and the coupling gap can be expressed as $g = 140 – 0.17V^2$ in nanometer.) The results are plotted in Fig. 6.5.

As for the mechanical oscillation, a mode of the fixed cavity is preferred. This is because an electrostatic force will be generated to displace the movable cavity and thus the force-induced stress may affect the mechanical resonance of the movable structures, which will be involved in the optomechanical coupling. However, the fixed cavity is immune to the electrostatic force that is applied to the movable structures. The mechanical mode selected for this study is an in-plane vibration mode, the mode shape of which is FEM simulated and plotted in Fig. 6.6 and the simulated mechanical resonance frequency is 4.08 MHz.

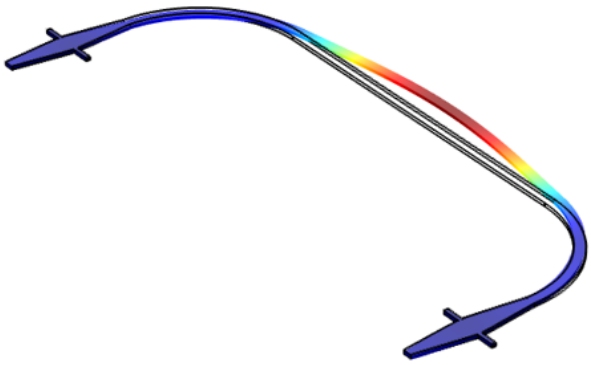

Figure 6.6 FEM-simulated mode shap of an in-plane mechanical resonance of the fixed cavity selected to characterize the tunable optomechanics.

Subsequently, the optomechanics results are measured under different applied voltages (different coupling gaps and thus different optomechanical coupling coefficients). The testing setup is illustrated in Fig. 6.7. After measuring the optical mode resonance wavelengths, the OSA is replaced by a photodetector to collect the optical output signal.

The detector converts the optical signal to electrical signal, which is finally measured by the signal analyzer. For each applied voltage step, the laser wavelength is scanned from the blue detuning side to the red detuning side of the corresponding resonance peak and at each wavelength detuning, and the mechanical vibration spectrum is acquired by the signal analyzer. The laser input serves as the optical actuation and optical read-out at the same time.

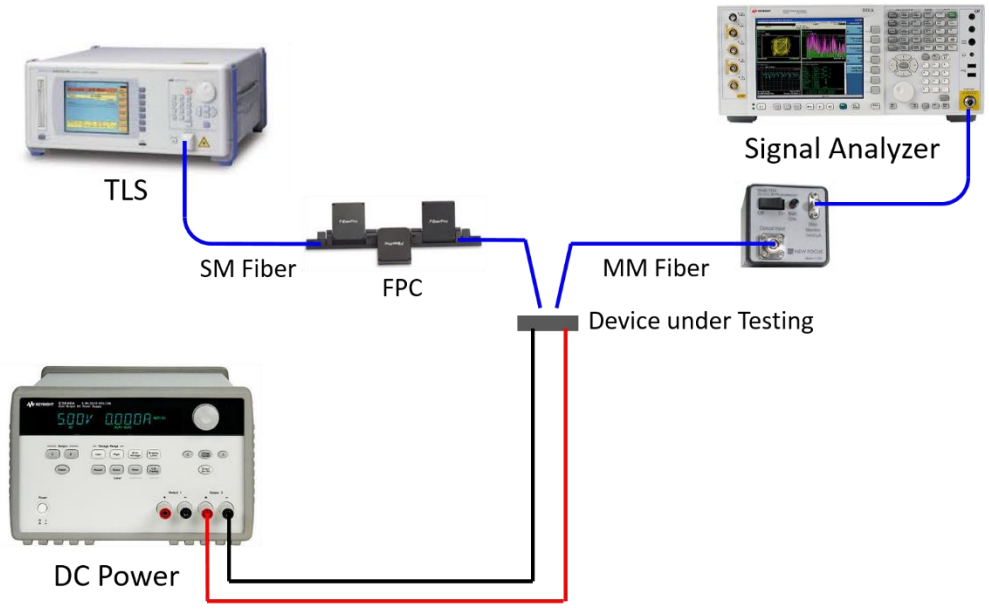

Figure 6.7 Schematic of the testing setup for optomechanics measurement.

Figure 6.8 is an example of the mechanical vibration spectrum obtained under an applied voltage of 9 V. The black curve denotes effective mechanical resonance with laser wavelength detuning of -0.716 nm. When the wavelength detuning is changed to -0.016 nm, the mechanical vibration spectrum becomes the red curve, indicating the presence of the optical spring effect. The *Q* factor of the mechanical oscillation is over 7000, indicating a mechanical amplification effect due to optomechanical coupling. (Note that the mechanical *Q* factor of a similar device is about 1000 to 2000 [135, 136].)

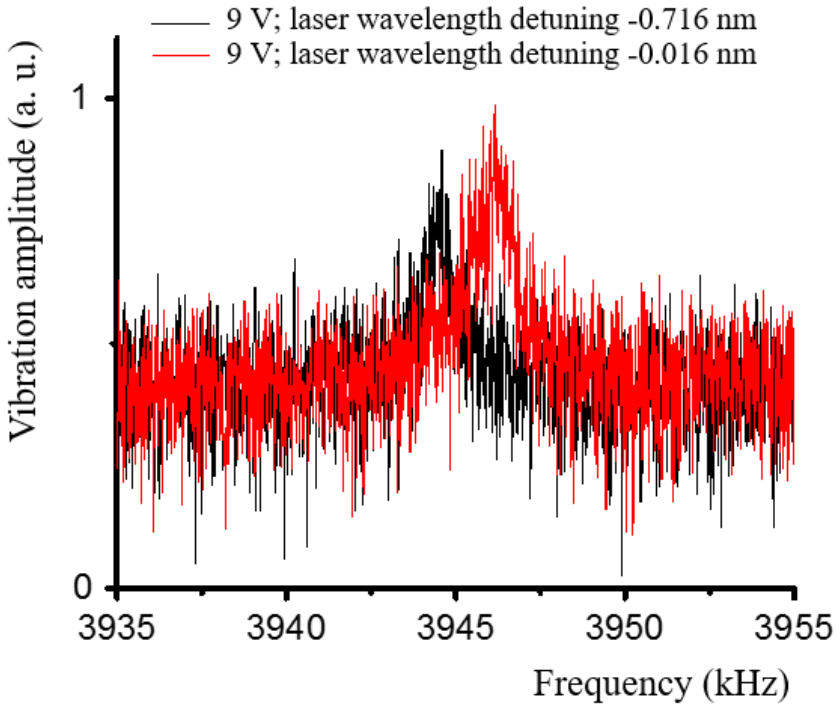

Figure 6.8 Examples of the mechanical resonance spectrum (amplitude-frequency relationship) and illustration of the effective mechanical resonance frequency tuning due to optomechanical coupling.

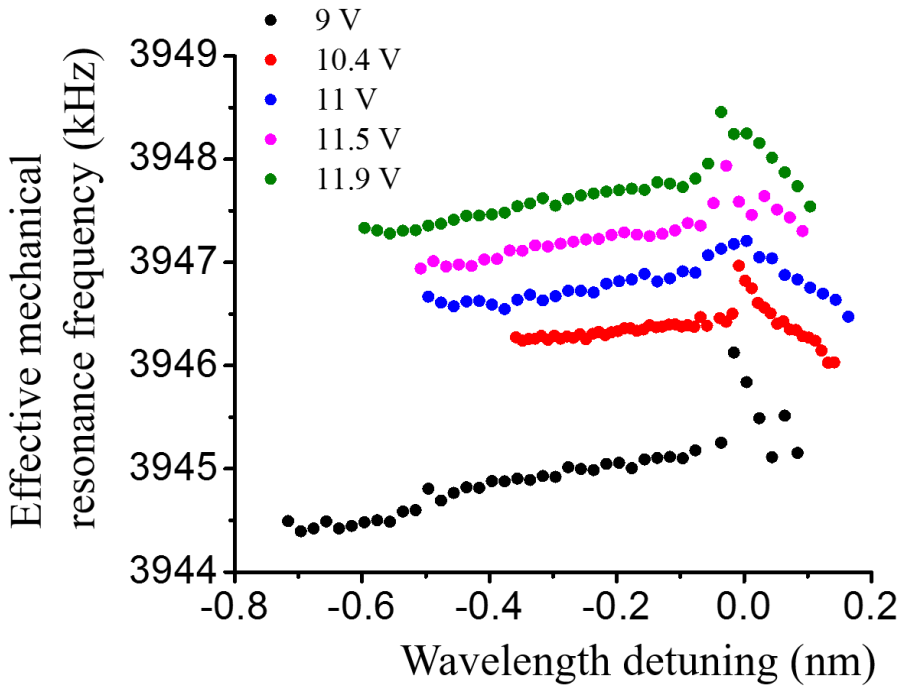

Figure 6.9 Measurement results of effective mechanical resonance frequency with respect to different pumping laser wavelength detuning under different applied voltages.

The effective mechanical resonance frequency under different applied voltages (different coupling gaps and thus different optomechanical coupling coefficients) are plotted and compared in Fig. 6.9.

As can be seen, the effective mechanical resonance frequency is higher in the red wavelength detuning range, indicating a combined effect of optical gradient force and thermo-optical tuning. It is also found that there is an upward drift of the entire effective mechanical frequency tuning range with a narrowing of the coupling gap. There would be two reasons for this phenomenon.

Firstly, there is a static component of the optical gradient force applied between the coupled cavities. Such a force is attractive because it is generated by pumping an even mode. Consequently, the force will induce a tension stress on the cavity beam and suspensions of the fixed cavity. The smaller the coupling gap is, the higher the optomechanical coupling coefficient and hence the higher optical force; thus, the tension stress induced will be greater too. As is known, increased level in tension stress in a mechanical structure will result in an increase in the mechanical resonance frequency. Thus, with a higher applied voltage (i.e. smaller coupling gap), the entire effective mechanical resonance frequency tuning range is higher. This possible reason agrees with the experimental results and analysis in Ref [195].

Secondly, different coupling gaps result in different optical resonance wavelengths and thus different total input coupling efficiencies, including those of the coupling between

the grating coupler and the feeding waveguide. Different coupling gaps may also induce different mode intensities in the two cavities, especially if the two cavities are slightly different. In other word, the light energy in the cavities may change with respect to the coupling gap. With different optical power inside, the temperature change (due to material absorption) will be different and in turn induce different thermal stress to the structure, thus varying the mechanical resonance frequency.

As to the effective mechanical resonance frequency tuning range, which can defined as $\max(\Omega'_M) - \min(\Omega'_M)$, the results under different applied voltages are plotted in Fig. 6.10.

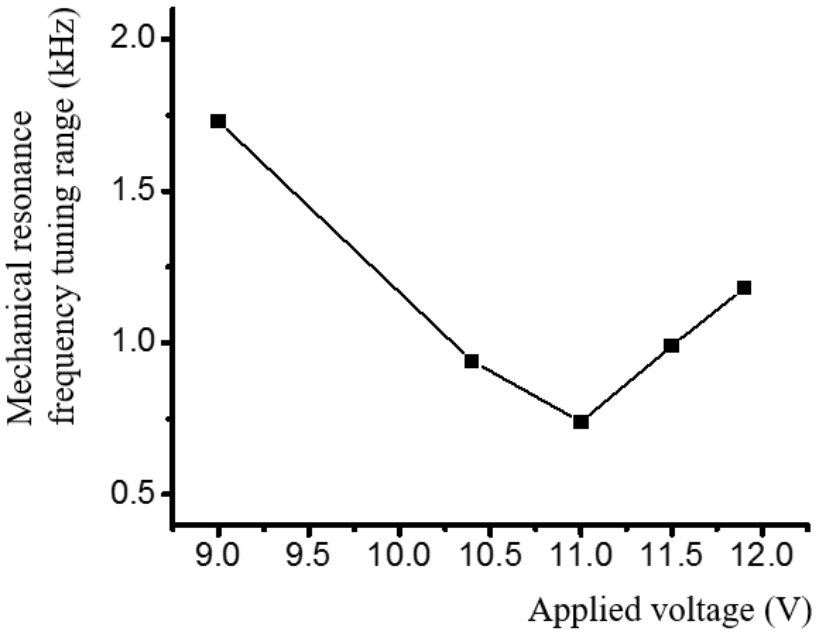

Figure 6.10 Results of mechanical resonance frequency tuning range with respect to different applied voltages.

The results clearly show the tunability of the optomechanics, although there is no clear variation trend. As discussed in the previous section, the optical spring effect depends

on both the optomechanical coupling coefficient and the light energy in the cavities. The optomechanical coupling coefficient will increase with a reduction in coupling gap. However, the light energy does not have a definite relationship with the coupling gap, the reason for which has been discussed earlier. Besides, this is hard to be characterized in experiments. Thus, due to the combined effect of optomechanical coupling coefficient and optical energy variations, the optomechanical coupling effect cannot be accurately predicted and analyzed.

6.3.2. Discussion

This chapter describes a tuning method of cavity optomechanics in dual-coupled PhC nanobeam cavities by varying the coupling gap and the experimental results obtained. Currently, cavity optomechanics is being intensively investigated and the interaction of optical mode and mechanical oscillation through optical force may result in break-through technologies to control and measure mechanical motion. The proposed tunable cavity optomechanics strengthen the control capability of optomechanics. This study paves a way for further investigations for both fundamental physics and potential applications.

Chapter 7. Conclusions and Future Work

7.1. Conclusions

The aim of this thesis is to study mechanical tuning and cavity optomechanics of photonic devices based on coupled photonic crystal nanobeam cavities. Towards this aim, the author first developed a nano fabrication process to fabricate photonic devices that are compatible with NEMS tuning and are able to generate optical force and cavity optomechanics. Most steps were conducted with standard micro and nano fabrication techniques, including various kinds of lithography, etching and deposition and there are also commercial equipment for these techniques. However, a key step, HF vapor release, has to be carried out with a home-made setup and there is no standard process and recipe. Eventually, the author succeeded in fabricating released structures, even those with long thin beams like the cavity beams. This study is presented in Chapter 3. Besides fabrication, the testing setup and equipment for the photonic devices investigated in this thesis are also introduced in the same chapter.

In Chapter 4, the author studied resonance tuning in dual-coupled PhC nanobeam cavities by laterally shifting the movable cavities with integrated NEMS comb drive actuators. This tuning method was demonstrated to possess high tuning efficiency when compared with conventional coupling gap tuning methods. More importantly, a coupling strength tuning over a range of several THz with a precision of a few GHz was realized in experiments. The coupling strength can be tuned continuously from negative

(strong coupling regime) to zero (weak coupling regime) and further to positive (strong coupling regime) and vice versa. Besides, the mode symmetry can also be inversed due to the inversion of the sign of coupling strength, which is not possible for the tuning through coupling gap variation. These results were predicted and analyzed by analytical methods based on the coupled mode theory and validated by 3D FDTD simulation. This study opens the door to the optimization of the coupling strength of the photonic molecules (PhC cavities) *in situ* for the study of cavity quantum electrodynamics and the development of efficient quantum information devices.

Based on the lateral tuning of coupled PhC cavities, lateral shearing optical gradient force generated by such coupled cavities was predicted. In particular, the lateral tuning resulted in resonance frequency shift and thus the light energy in the system. In other words, the system energy varies with respect to the lateral displacement and thus, optical force in the lateral direction should exist. In experiments, resonance tuning by laterally tuning the coupled cavities using NEMS comb drive was first characterized. and the resonance wavelength-lateral offset relationship was accurately calibrated. It was found that the absolute value of optomechanical coupling coefficient was relatively high at an lateral offset of about 100 nm. The force at this offset value was measured in the static mode using a developed measurement method. When optically pumping for optical force, the thermo-optical effects will be involved and thus the force cannot be detected by monitoring the resonance wavelength shift on a single resonance mode. However, the author proposed to detect the force by monitoring the resonance

wavelength splitting width variation of another pair of supermodes from the same order. Assuming the thermo-optical effects on the λ_+ and λ_- mode resonance from the same order are equal, by monitoring the resonance splitting width changing, the thermo-optical effect can be decoupled from the mechanical tuning effect induced by the optical force. With the spring constant of beam suspension estimated with FEM, the optical force generated can be calculated. In experiments, optical forces were generated by pumping on the fourth order even and odd modes respectively and measured by monitoring the resonance wavelength splitting of the third order supermodes. Attractive forces as high as 0.29 nN and repulsive forces as high as 0.42 nN were demonstrated in experiments. According to the author's knowledge, this is the first study of such lateral shearing optical gradient force as well as the proposed measurement method. This study may further widen the potential applications of nano optomechanics and may be useful in future nanooptoelectromechanical systems.

As discussed in Chapter 1 and Chapter 2, cavity optomechanics is more attractive compared with the study in Chapter 5, in which optical gradient force was investigated to reconfigure nano structures in static mode. Though there is numerous studies of cavity optomechanics based on on-chip photonic devices, tunable cavity optomechanics is scarcely reported. To fill this gap, in Chapter 6 the author studied the cavity optomechanics in dual-couple PhC nanobeam cavities and proposed a tuning method by varying the coupling gap between the cavities. The proposed method was successfully demonstrated in experiments. The tuning was realized by the

optomechanical coupling coefficient variation and the system light energy changing induced by the coupling gap tuning. The impact of this study lies in the strengthening of the capability of optomechanics in controlling and measurement of mechanical motions. The demonstrated tunability of the cavity optomechanics has potential in both further fundamental theory studies and possible applications.

7.2. Future Work

Due to the limited time of the author's PhD project, there are several studies that the author believes to be of impact but they have not been completed.

Firstly, the nano fabrication process developed requires two steps of EBL patterning. Thus, if there is misalignment between the two EBL steps, the optical performance would be greatly degraded. As shown in Fig. 7.1, the patterns of the tapered rib waveguide and the feeding waveguide are misaligned. In experiments, the misalignment can be as large as hundreds of nanometers and even over one micrometer, which will dramatically reduce the cavity transmissions and *Q* factors, and even result in the loss of function of the device. To address this issue, the author proposes to develop a single-EBL step method. It is suggested that the patterns of the entire device can be defined by a single EBL step. Then the developed patterns could be selectively etched by covering the patterns not to be etched with another layer of etching mask, which can be patterned with photolithography. In this way, the key patterns of the device should be free of EBL alignment problems.

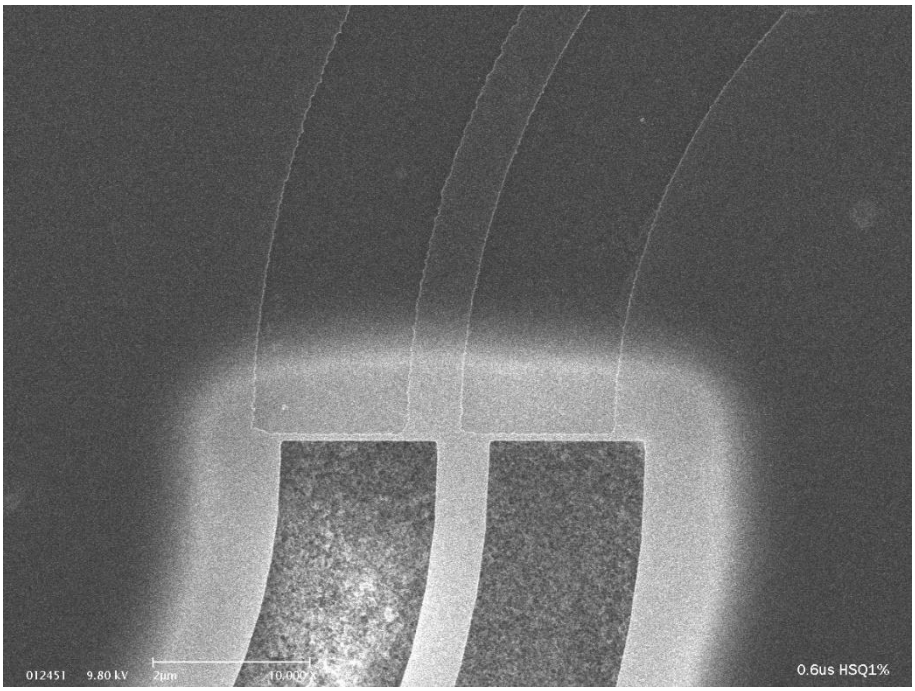

Figure 7.1 SEM image of the connection between the tapered rib waveguide and the feeding waveguide with misalignment.

Secondly, to further enhance the resonance tuning and coupling strength tuning performance, it is suggested that improvement of the optical resonator design be studied. The resonators should not be limited to be based on silicon or pure dielectric materials. Plasmonic resonators can be designed and employed for the resonance and coupling strength tuning. Furthermore, the NEMS actuators also can be improven to have reduced mass and thus higher operation speed.

Thirdly, as discussed in Chapter 6, the proposed cavity optomechanics tuning method of varying the coupling gap of coupled cavities, combines the effects of optomechanical coupling coefficient changing and light energy variation. Thus, to precisely control the optomechanics, a tuning method involving only one variable factor should be developed.

Fourthly, to push the nano photonic devices to practical applications, device packaging is a key technique. Yet, to date, there is still no established packaging technique for nano photonic devices comparable with MEMS device packaging, mainly due to the difficulties of optical input and output. Thus, for devices requiring external light sources and detectors, it is important to develop a stable and reliable light coupling method for photonic device packaging. Another solution is to develop active devices based on III-V materials, in which case external light source is not essential, making light input unnecessary. There are already numerous studies on active photonic devices based on III-V materials, however, such devices with wide tuning range are still in the stage of development.

Reference

[1] R. A. Minasian, "Photonic signal processing of microwave signals," *Ieee Transactions on Microwave Theory and Techniques,* vol. 54, pp. 832-846, Feb 2006.

[2] J. Capmany, J. Mora, I. Gasulla, J. Sancho, J. Lloret, and S. Sales, "Microwave Photonic Signal Processing," *Journal of Lightwave Technology,* vol. 31, pp. 571-586, Feb 15 2013.

[3] L. Tsybeskov, D. J. Lockwood, and M. Ichikawa, "Silicon Photonics CMOS Going Optical," *Proceedings of the IEEE,* vol. 97, pp. 1161-1165, 2009.

[4] T. Baehr-Jones, T. Pinguet, P. Lo Guo-Qiang, S. Danziger, D. Prather, and M. Hochberg, "Myths and rumours of silicon photonics," *Nature Photonics,* vol. 6, pp. 206-208, 2012.

[5] R. Soref, "The Past, Present, and Future of Silicon Photonics," *Ieee Journal of Selected Topics in Quantum Electronics,* vol. 12, pp. 1678-1687, 2006.

[6] M. Hochberg and T. Baehr-Jones, "Towards fabless silicon photonics," *Nature Photonics,* vol. 4, pp. 492-494, 2010.

[7] J. Capmany and D. Novak, "Microwave photonics combines two worlds," *Nature Photonics,* vol. 1, pp. 319-330, 2007.

[8] D. T. Neilson, "Photonics for switching and routing," *Ieee Journal of Selected Topics in Quantum Electronics,* vol. 12, pp. 669-678, 2006.

[9] B. Jalali, "Silicon Photonics," *Journal of Lightwave Technology,* vol. 24, pp. 4600-4615, 2006.

[10] G. T. Reed, G. Mashanovich, F. Y. Gardes, and D. J. Thomson, "Silicon optical modulators," *Nature Photonics,* vol. 4, pp. 518-526, 2010.

[11] M. W. Pruessner, T. H. Stievater, M. S. Ferraro, and W. S. Rabinovich, "Thermo-optic tuning and switching in SOI waveguide Fabry-Perot microcavities," *Optics Express,* vol. 15, pp. 7557-7563, Jun 11 2007.

[12] A. Guarino, G. Poberaj, D. Rezzonico, R. Degl'Innocenti, and P. Gunter, "Electro-optically tunable microring resonators in lithium niobate," *Nature Photonics,* vol. 1, pp. 407-410, Jul 2007.

[13] T. J. Wang, C. H. Chu, and C. Y. Lin, "Electro-optically tunable microring resonators on lithium niobate," *Optics Letters,* vol. 32, pp. 2777-2779, Oct 1 2007.

[14] D. Scrymgeour, N. Malkova, S. Kim, and V. Gopalan, "Electro-optic control of the superprism effect in photonic crystals," *Applied Physics Letters,* vol. 82, p. 3176, 2003.

[15] F. Chollet, "Devices Based on Co-Integrated MEMS Actuators and Optical Waveguide: A Review," *Micromachines,* vol. 7, p. 18, 2016.

[16] L.-S. Fan, Y.-C. Tai, and R. S. Muller, "IC-processed electrostatic micromotors," *Sensors and Actuators,* vol. 20, pp. 41-47, 1989.

[17] M. Bao and W. Wang, "Future of microelectromechanical systems (MEMS)," *Sensors and Actuators A: Physical*, vol. 56, pp. 135-141, 1996.

[18] J. W. Judy, "Microelectromechanical systems (MEMS) fabrication, design and applications," *Smart materials and Structures*, vol. 10, p. 1115, 2001.

[19] H. G. Craighead, "Nanoelectromechanical Systems," *Science*, vol. 290, pp. 1532-1535, 2000.

[20] K. L. Ekinci and M. L. Roukes, "Nanoelectromechanical systems," *Review of Scientific Instruments*, vol. 76, p. 061101, 2005.

[21] R. St-Gelais, B. Guha, L. X. Zhu, S. H. Fan, and M. Lipson, "Demonstration of Strong Near-Field Radiative Heat Transfer between Integrated Nanostructures," *Nano Letters*, vol. 14, pp. 6971-6975, Dec 2014.

[22] M. Loncar, T. Doll, J. Vuckovic, and A. Scherer, "Design and fabrication of silicon photonic crystal optical waveguides," *Journal of Lightwave Technology*, vol. 18, pp. 1402-1411, Oct 2000.

[23] Y. Q. Jiang, W. Jiang, L. L. Gu, X. N. Chen, and R. T. Chen, "80-micron interaction length silicon photonic crystal waveguide modulator," *Applied Physics Letters*, vol. 87, Nov 28 2005.

[24] M. Li, W. H. P. Pernice, and H. X. Tang, "Tunable bipolar optical interactions between guided lightwaves," *Nature Photonics*, vol. 3, pp. 464-468, Aug 2009.

[25] J. Roels, I. De Vlaminck, L. Lagae, B. Maes, D. Van Thourhout, and R. Baets, "Tunable optical forces between nanophotonic waveguides," *Nature Nanotechnology*, vol. 4, pp. 510-513, Aug 2009.

[26] T. J. Kippenberg and K. J. Vahala, "Cavity optomechanics: back-action at the mesoscale," *Science*, vol. 321, pp. 1172-6, Aug 29 2008.

[27] M. A. Hughes, M. A. Lourenco, J. D. Carey, B. Murdin, and K. P. Homewood, "Crystal field analysis of Dy and Tm implanted silicon for photonic and quantum technologies," *Opt Express*, vol. 22, pp. 29292-303, Dec 1 2014.

[28] D. G. Grier, "A revolution in optical manipulation," *Nature*, vol. 424, pp. 810-816, 2003.

[29] D. Psaltis, S. R. Quake, and C. Yang, "Developing optofluidic technology through the fusion of microfluidics and optics," *Nature*, vol. 442, pp. 381-6, Jul 27 2006.

[30] J. Leuthold, C. Koos, and W. Freude, "Nonlinear silicon photonics," *Nature Photonics*, vol. 4, pp. 535-544, 2010.

[31] L. Shao, X. F. Jiang, X. C. Yu, B. B. Li, W. R. Clements, F. Vollmer, *et al.*, "Detection of single nanoparticles and lentiviruses using microcavity resonance broadening," *Adv Mater*, vol. 25, pp. 5616-20, Oct 18 2013.

[32] B. B. Li, W. R. Clements, X. C. Yu, K. Shi, Q. Gong, and Y. F. Xiao, "Single nanoparticle detection using split-mode microcavity Raman lasers," *Proc Natl Acad Sci U S A*, vol. 111, pp. 14657-62, Oct 14 2014.

[33] J. M. Geremia, J. Williams, and H. Mabuchi, "Inverse-problem approach to designing photonic crystals for cavity QED experiments," *Phys Rev E Stat Nonlin Soft Matter Phys*, vol. 66, p. 066606, Dec 2002.

[34] E. Kuramochi, M. Notomi, S. Mitsugi, A. Shinya, T. Tanabe, and T. Watanabe, "Ultrahigh-Q photonic crystal nanocavities realized by the local width modulation of a line defect," *Applied Physics Letters,* vol. 88, p. 041112, 2006.

[35] B. S. Song, S. Noda, T. Asano, and Y. Akahane, "Ultra-high-Q photonic double-heterostructure nanocavity," *Nature Materials,* vol. 4, pp. 207-210, Mar 2005.

[36] B.-S. Song, S. Noda, T. Asano, and Y. Akahane, "Ultra-high-Q photonic double-heterostructure nanocavity," *Nature Materials,* vol. 4, pp. 207-210, 2005.

[37] E. Yablonovitch, "Inhibited spontaneous emission in solid-state physics and electronics," *Phys Rev Lett,* vol. 58, pp. 2059-2062, May 18 1987.

[38] S. John, "Strong localization of photons in certain disordered dielectric superlattices," *Phys Rev Lett,* vol. 58, pp. 2486-2489, Jun 8 1987.

[39] M. Thorhauge, L. H. Frandsen, and P. I. Borel, "Efficient photonic crystal directional couplers," *Optics Letters,* vol. 28, pp. 1525-1527, Sep 1 2003.

[40] Y. Akahane, T. Asano, B. S. Song, and S. Noda, "High-Q photonic nanocavity in a two-dimensional photonic crystal," *Nature,* vol. 425, pp. 944-947, Oct 30 2003.

[41] M. Notomi, E. Kuramochi, and H. Taniyama, "Ultrahigh-Q nanocavity with 1D photonic gap," *Opt Express,* vol. 16, pp. 11095-102, Jul 21 2008.

[42] P. B. Deotare, M. W. McCutcheon, I. W. Frank, M. Khan, and M. Lončar, "High quality factor photonic crystal nanobeam cavities," *Applied Physics Letters,* vol. 94, p. 121106, 2009.

[43] A. R. M. Zain, N. P. Johnson, M. Sorel, and R. M. D. L. Rue, "Ultra high quality factor one dimensional photonic crystal_photonic wire micro-cavities in silicon-on-insulator (SOI)," *Optics Express,* vol. 16, pp. 12084-12089, 2008.

[44] T. Tanabe, M. Notomi, S. Mitsugi, A. Shinya, and E. Kuramochi, "All-optical switches on a silicon chip realized using photonic crystal nanocavities," *Applied Physics Letters,* vol. 87, p. 151112, 2005.

[45] D. Englund, A. Faraon, I. Fushman, N. Stoltz, P. Petroff, and J. Vuckovic, "Controlling cavity reflectivity with a single quantum dot," *Nature,* vol. 450, pp. 857-61, Dec 6 2007.

[46] K. Hennessy, A. Badolato, M. Winger, D. Gerace, M. Atature, S. Gulde, *et al.*, "Quantum nature of a strongly coupled single quantum dot-cavity system," *Nature,* vol. 445, pp. 896-9, Feb 22 2007.

[47] J. P. Reithmaier, G. Sek, A. Loffler, C. Hofmann, S. Kuhn, S. Reitzenstein, *et al.*, "Strong coupling in a single quantum dot-semiconductor microcavity system," *Nature,* vol. 432, pp. 197-200, Nov 11 2004.

[48] K. Srinivasan and O. Painter, "Linear and nonlinear optical spectroscopy of a strongly coupled microdisk-quantum dot system," *Nature,* vol. 450, pp. 862-5, Dec 6 2007.

[49] M. Lončar, T. Yoshie, A. Scherer, P. Gogna, and Y. Qiu, "Low-threshold photonic crystal laser," *Applied Physics Letters,* vol. 81, p. 2680, 2002.

[50] M. Lončar, A. Scherer, and Y. Qiu, "Photonic crystal laser sources for chemical detection," *Applied Physics Letters,* vol. 82, p. 4648, 2003.

[51] D. Erickson, S. Mandal, A. H. Yang, and B. Cordovez, "Nanobiosensors: optofluidic, electrical and mechanical approaches to biomolecular detection at the nanoscale," *Microfluid Nanofluidics,* vol. 4, pp. 33-52, 2008.

[52] E. Bulgan, Y. Kanamori, and K. Hane, "Submicron silicon waveguide optical switch driven by microelectromechanical actuator," *Applied Physics Letters,* vol. 92, Mar 10 2008.

[53] W. C. Tang, T. C. H. Nguyen, M. W. Judy, and R. T. Howe, "Electrostatic-comb drive of lateral polysilicon resonators," *Sensors and Actuators a-Physical,* vol. 21, pp. 328-331, 1990.

[54] W. C. Tang, T. C. H. Nguyen, and R. T. Howe, "Laterally Driven Polysilicon Resonant Microstructures," *Sensors and Actuators,* vol. 20, pp. 25-32, Nov 15 1989.

[55] R. Legtenberg, A. W. Groeneveld, and M. Elwenspoek, "Comb-drive actuators for large displacements," *Journal of Micromechanics and Microengineering,* vol. 6, pp. 320-329, Sep 1996.

[56] M. Li, W. H. P. Pernice, and H. X. Tang, "Broadband all-photonic transduction of nanocantilevers," *Nature Nanotechnology,* vol. 4, pp. 377-382, Jun 2009.

[57] H. B. Yu, G. Y. Zhou, X. Y. Chew, S. K. Sinha, and F. S. Chau, "Nano-tribometer integrated with a nano-photonic displacement-sensing mechanism," *Journal of Micromechanics and Microengineering,* vol. 21, Jun 2011.

[58] M. C. M. Lee, D. Y. Hah, E. K. Lau, H. Toshiyoshi, and M. Wu, "MEMS-actuated photonic crystal switches," *Ieee Photonics Technology Letters,* vol. 18, pp. 358-360, Jan-Feb 2006.

[59] R. Mudachathi and P. Nair, "Low-Voltage Widely Tunable Photonic Crystal Channel Drop Filter in SOI Wafer," *Journal of Microelectromechanical Systems,* vol. 21, pp. 190-197, Feb 2012.

[60] S. Abe and K. Hane, "Variable-Gap Silicon Photonic Waveguide Coupler Switch With a Nanolatch Mechanism," *Ieee Photonics Technology Letters,* vol. 25, pp. 675-677, Apr 1 2013.

[61] Y. Akihama, Y. Kanamori, and K. Hane, "Ultra-small silicon waveguide coupler switch using gap-variable mechanism," *Optics Express,* vol. 19, pp. 23658-23663, Nov 21 2011.

[62] S. Abe, M. H. Chu, T. Sasaki, and K. Hane, "Time Response of a Microelectromechanical Silicon Photonic Waveguide Coupler Switch," *Ieee Photonics Technology Letters,* vol. 26, pp. 1553-1556, Aug 1 2014.

[63] Y. Akihama and K. Hane, "Single and multiple optical switches that use freestanding silicon nanowire waveguide couplers," *Light-Science & Applications,* vol. 1, Jun 2012.

[64] Y. Akihama and K. Hane, "An analytical coupling coefficient for MEMS tunable silicon nanowire waveguide coupler devices," *Microsystem Technologies-Micro-and Nanosystems-Information Storage and Processing Systems,* vol. 19, pp. 583-589, Apr 2013.

[65] Y. Munemasay and K. Hane, "A Compact 1 x 3 Silicon Photonic Waveguide

Switch Based on Precise Investigation of Coupling Characteristics of Variable-Gap Coupler," *Japanese Journal of Applied Physics,* vol. 52, Jun 2013.

[66] S. Han, T. J. Seok, N. Quack, B. W. Yoo, and M. C. Wu, "Large-scale silicon photonic switches with movable directional couplers," *Optica,* vol. 2, pp. 370-375, Apr 20 2015.

[67] T. J. Seok, N. Quack, S. Han, R. S. Muller, and M. C. Wu, "Large-scale broadband digital silicon photonic switches with vertical adiabatic couplers," *Optica,* vol. 3, p. 64, 2016.

[68] K. Van Acoleyen, J. Roels, P. Mechet, T. Claes, D. Van Thourhout, and R. Baets, "Ultracompact Phase Modulator Based on a Cascade of NEMS-Operated Slot Waveguides Fabricated in Silicon-on-Insulator," *Ieee Photonics Journal,* vol. 4, pp. 779-788, Jun 2012.

[69] T. Ikeda, K. Takahashi, Y. Kanamori, and K. Hane, "Phase-shifter using submicron silicon waveguide couplers with ultra-small electro-mechanical actuator," *Optics Express,* vol. 18, pp. 7031-7037, Mar 29 2010.

[70] T. Ikeda and K. Hane, "A microelectromechanically tunable microring resonator composed of freestanding silicon photonic waveguide couplers," *Applied Physics Letters,* vol. 102, Jun 3 2013.

[71] H. M. Chu and K. Hane, "A Wide-Tuning Silicon Ring-Resonator Composed of Coupled Freestanding Waveguides," *Ieee Photonics Technology Letters,* vol. 26, pp. 1411-1413, Jul 15 2014.

[72] T. Ikeda and K. Hane, "A tunable notch filter using microelectromechanical microring with gap-variable busline coupler," *Optics Express,* vol. 21, pp. 22034-22042, Sep 23 2013.

[73] K. J. Vahala, "Optical microcavities," *Nature,* vol. 424, pp. 839-846, Aug 14 2003.

[74] S. Abe and K. Hane, "A silicon microring resonator with a nanolatch mechanism," *Microsystem Technologies-Micro-and Nanosystems-Information Storage and Processing Systems,* vol. 21, pp. 2019-2024, Sep 2015.

[75] Y. Kanamori, Y. Sato, and K. Hane, "Fabrication of Silicon Microdisk Resonators with Movable Waveguides for Control of Power Coupling Ratio," *Japanese Journal of Applied Physics,* vol. 52, Jun 2013.

[76] M. Ordu and K. Hane, "Transmission-Width-Tunable Silicon-Photonic Microelectromechanical Ring Resonator," *Ieee Photonics Technology Letters,* vol. 25, Nov 15 2013.

[77] K. Takahashi, Y. Kanamori, Y. Kokubun, and K. Hane, "A wavelength-selective add-drop switch using silicon microring resonator with a submicron-comb electrostatic actuator," *Optics Express,* vol. 16, pp. 14421-14428, Sep 15 2008.

[78] M. C. M. Lee and M. C. Wu, "MEMS-Actuated microdisk resonators with variable power coupling ratios," *Ieee Photonics Technology Letters,* vol. 17, pp. 1034-1036, May 2005.

[79] J. Yao, D. Leuenberger, M. C. M. Lee, and M. C. Wu, "Silicon microtoroidal resonators with integrated MEMS tunable coupler," *Ieee Journal of Selected*

Topics in Quantum Electronics, vol. 13, pp. 202-208, Mar-Apr 2007.

[80] M. C. M. Lee and M. C. Wu, "Tunable coupling regimes of silicon microdisk resonators using MEMS actuators," *Optics Express,* vol. 14, pp. 4703-4712, May 29 2006.

[81] M. C. M. Lee and M. C. Wu, "Variable bandwidth of dynamic add-drop filters based on coupling-controlled microdisk resonators," *Optics Letters,* vol. 31, pp. 2444-2446, Aug 15 2006.

[82] B. Zhang, D. Leuenberger, M. C. M. Lee, A. E. Willner, and M. C. Wu, "Experimental demonstration of dynamic bandwidth allocation using a MEMS-Actuated bandwidth-tunable microdisk resonator filter," *Ieee Photonics Technology Letters,* vol. 19, pp. 1508-1510, Sep-Oct 2007.

[83] S. Sridaran and S. A. Bhave, "Electrostatic actuation of silicon optomechanical resonators," *Optics Express,* vol. 19, pp. 9020-9026, May 9 2011.

[84] Y. Kanamori, K. Takahashi, and K. Hane, "An ultrasmall wavelength-selective channel drop switch using a nanomechanical photonic crystal nanocavity," *Applied Physics Letters,* vol. 95, Oct 26 2009.

[85] M. F. Yanik and S. Fan, "Stopping light all optically," *Phys Rev Lett,* vol. 92, p. 083901, Feb 27 2004.

[86] S. Mahnkopf, R. Marz, M. Kamp, G.-H. Duan, F. Lelarge, and A. Forchel, "Tunable photonic crystal coupled-cavity laser," *IEEE journal of quantum electronics,* vol. 40, pp. 1306-1314, 2004.

[87] S. M. C. Abdulla, L. J. Kauppinen, G. J. M. Krijnen, and R. M. d. Ridder, "Mechano-optical wavelength tuning in a photonic crystal microcavity with sub-1 V drive voltage," *Optics Letters* vol. 37, pp. 2010-2012, 2012.

[88] S. M. C. Abdulla, L. J. Kauppinen, M. Dijkstra, E. Berenschot, M. J. de Boer, R. M. de Ridder, *et al.,* "Mechano-Optical Switching in a Mems Integrated Photonic Crystal Slab Waveguide," *2011 Ieee 24th International Conference on Micro Electro Mechanical Systems (Mems),* pp. 9-12, 2011.

[89] G. N. Nielson, D. Seneviratne, F. Lopez-Royo, P. T. Rakich, Y. Avrahami, M. R. Watts, *et al.,* "Integrated wavelength-selective optical MEMS switching using ring resonator filters," *Ieee Photonics Technology Letters,* vol. 17, pp. 1190-1192, Jun 2005.

[90] S. M. C. Abdulla, L. J. Kauppinen, M. Dijkstra, M. J. de Boer, E. Berenschot, H. V. Jansen, *et al.,* "Tuning a racetrack ring resonator by an integrated dielectric MEMS cantilever," *Optics Express,* vol. 19, pp. 15864-15878, Aug 15 2011.

[91] X. Y. Chew, G. Y. Zhou, F. S. Chau, and J. Deng, "Enhanced resonance tuning of photonic crystal nanocavities by integration of optimized near-field multitip nanoprobes," *Journal of Nanophotonics,* vol. 5, Apr 21 2011.

[92] X. Y. Chew, G. Y. Zhou, H. B. Yu, F. S. Chau, J. Deng, Y. C. Loke, *et al.,* "An in-plane nano-mechanics approach to achieve reversible resonance control of photonic crystal nanocavities," *Optics Express,* vol. 18, pp. 22232-22244, Oct 11 2010.

[93] I. W. Frank, P. B. Deotare, M. W. McCutcheon, and M. Loncar, "Programmable

photonic crystal nanobeam cavities," *Optics Express*, vol. 18, pp. 8705-8712, Apr 12 2010.

[94] L. Midolo, S. N. Yoon, F. Pagliano, T. Xia, F. W. M. van Otten, M. Lermer, *et al.*, "Electromechanical tuning of vertically-coupled photonic crystal nanobeams," *Optics Express*, vol. 20, pp. 19255-19263, Aug 13 2012.

[95] X. Y. Chew, G. Y. Zhou, F. S. Chau, J. Deng, X. S. Tang, and Y. C. Loke, "Dynamic tuning of an optical resonator through MEMS-driven coupled photonic crystal nanocavities," *Optics Letters*, vol. 35, pp. 2517-2519, Aug 1 2010.

[96] X. Chew, G. Y. Zhou, F. S. Chau, and J. Deng, "Nanomechanically Tunable Photonic Crystal Resonators Utilizing Triple-Beam Coupled Nanocavities," *Ieee Photonics Technology Letters*, vol. 23, pp. 1310-1312, Sep 15 2011.

[97] F. Tian, G. Y. Zhou, F. S. Chau, J. Deng, and R. Akkipeddi, "Measurement of coupled cavities' optomechanical coupling coefficient using a nanoelectromechanical actuator," *Applied Physics Letters*, vol. 102, Feb 25 2013.

[98] J. Gao, J. F. McMillan, M. C. Wu, J. J. Zheng, S. Assefa, and C. W. Wong, "Demonstration of an air-slot mode-gap confined photonic crystal slab nanocavity with ultrasmall mode volumes," *Applied Physics Letters*, vol. 96, Feb 1 2010.

[99] M. Winger, T. D. Blasius, T. P. M. Alegre, A. H. Safavi-Naeini, S. Meenehan, J. Cohen, *et al.*, "A chip-scale integrated cavity-electro-optomechanics platform," *Optics Express*, vol. 19, pp. 24905-24921, Dec 5 2011.

[100] A. Pitanti, J. M. Fink, A. H. Safavi-Naeini, J. T. Hill, C. U. Lei, A. Tredicucci, *et al.*, "Strong opto-electro-mechanical coupling in a silicon photonic crystal cavity," *Optics Express*, vol. 23, pp. 3196-3208, Feb 9 2015.

[101] F. Tian, G. Y. Zhou, F. S. Chau, J. Deng, Y. Du, X. S. Tang, *et al.*, "Tuning of split-ladder cavity by its intrinsic nano-deformation," *Optics Express*, vol. 20, pp. 27697-27707, Dec 3 2012.

[102] P. Shi, H. Du, F. S. Chau, G. Y. Zhou, and J. Deng, "Tuning the quality factor of split nanobeam cavity by nanoelectromechanical systems," *Optics Express*, vol. 23, pp. 19338-19347, Jul 27 2015.

[103] T. Lin, F. Tian, P. Shi, F. S. Chau, G. Y. Zhou, X. S. Tang, *et al.*, "Design of mechanically-tunable photonic crystal split-beam nanocavity," *Optics Letters*, vol. 40, pp. 3504-3507, Aug 1 2015.

[104] T. Lin, X. W. Zhang, Y. C. Zou, F. S. Chau, J. Deng, and G. Y. Zhou, "Out-of-plane nano-electro-mechanical tuning of the Fano resonance in photonic crystal split-beam nanocavity," *Applied Physics Letters*, vol. 107, Oct 12 2015.

[105] S. V. Zhukovsky, D. N. Chigrin, A. V. Lavrinenko, and J. Kroha, "Switchable lasing in multimode microcavities," *Phys Rev Lett.*, vol. 99, p. 073902, Aug 17 2007.

[106] Y. Sato, Y. Tanaka, J. Upham, Y. Takahashi, T. Asano, and S. Noda, "Strong coupling between distant photonic nanocavities and its dynamic control,"

Nature Photonics, vol. 6, pp. 56-61, 2011.

[107] X. Yang, M. Yu, D. L. Kwong, and C. W. Wong, "All-optical analog to electromagnetically induced transparency in multiple coupled photonic crystal cavities," *Phys Rev Lett,* vol. 102, p. 173902, May 1 2009.

[108] M. Notomi, E. Kuramochi, and T. Tanabe, "Large-scale arrays of ultrahigh-Q coupled nanocavities," *Nature Photonics,* vol. 2, pp. 741-747, 2008.

[109] B. R. Johnson, M. D. Reed, A. A. Houck, D. I. Schuster, L. S. Bishop, E. Ginossar, *et al.*, "Quantum non-demolition detection of single microwave photons in a circuit," *Nature Physics,* vol. 6, pp. 663-667, 2010.

[110] T. Mukaiyama, K. Takeda, H. Miyazaki, Y. Jimba, and M. Kuwata-Gonokami, "Tight-Binding Photonic Molecule Modes of Reson," *Phys. Rev. Lett,* vol. 82, p. 4623, 1999.

[111] M. Bayer, T. Gutbrod, J. P. Reithmaier, A. Forchel, T. L. Reinecke, P. A. Knipp, *et al.*, "Optical Modes in Photonic Molecules," *Phys. Rev. Lett.*, vol. 81, p. 2582, 1998.

[112] X. Zhang, H. Li, X. Tu, X. Wu, L. Liu, and L. Xu, "Suppression and hopping of whispering gallery modes in multiple-ring-coupled microcavity lasers," *Journal of the Optical Society of America B,* vol. 28, pp. 483-488, 2011.

[113] H. Wang, M. Mariantoni, R. C. Bialczak, M. Lenander, E. Lucero, M. Neeley, *et al.*, "Deterministic entanglement of photons in two superconducting microwave resonators," *Phys Rev Lett,* vol. 106, p. 060401, Feb 11 2011.

[114] T. C. Liew and V. Savona, "Single photons from coupled quantum modes," *Phys Rev Lett,* vol. 104, p. 183601, May 7 2010.

[115] P. Hamel, S. Haddadi, F. Raineri, P. Monnier, G. Beaudoin, I. Sagnes, *et al.*, "Spontaneous mirror-symmetry breaking in coupled photonic-crystal nanolasers," *Nature Photonics,* vol. 9, pp. 311-315, 2015.

[116] M. Abbarchi, A. Amo, V. G. Sala, D. D. Solnyshkov, H. Flayac, L. Ferrier, *et al.*, "Macroscopic quantum self-trapping and Josephson oscillations of exciton polaritons," *Nature Physics,* vol. 9, pp. 275-279, 2013.

[117] N. Caselli, F. Intonti, F. Riboli, and M. Gurioli, "Engineering the mode parity of the ground state in photonic crystal molecules," *Opt Express,* vol. 22, pp. 4953-9, Mar 10 2014.

[118] N. Caselli, F. Intonti, C. Bianchi, F. Riboli, S. Vignolini, L. Balet, *et al.*, "Post-fabrication control of evanescent tunnelling in photonic crystal molecules," *Applied Physics Letters,* vol. 101, p. 211108, 2012.

[119] K. C. Neuman and S. M. Block, "Optical trapping," *Rev Sci Instrum,* vol. 75, pp. 2787-809, Sep 2004.

[120] M. L. Povinelli, M. Lončar, M. Ibanescu, E. J. Smythe, S. G. Johnson, F. Capasso, *et al.*, "Evenescent-wave bonding between optical waveguides," *Opt Lett,* vol. 30, pp. 3042-3044, 2005.

[121] W. H. P. Pernice, M. Li, K. Y. Fong, and H. X. Tang, "Modeling of the optical force between propagating lightwaves in parallel 3D waveguides," *Optics Express,* vol. 17, pp. 16032-16037, 2009.

[122] F. Riboli, A. Recati, M. Antezza, and I. Carusotto, "Radiation induced force between two planar waveguides," *The European Physical Journal D*, vol. 46, pp. 157-164, 2007.

[123] W. H. P. Pernice, M. Li, and H. X. Tang, "Theoretical investigation of the transverse optical force between a silicon nanowire waveguide and a substrate," *Optics Express*, vol. 17, pp. 1806-1816, 2009.

[124] M. L. Povinelli, S. G. Johnson, M. Lončar, M. Ibanescu, E. J. Smythe, F. Capasso, *et al.*, "High-Q enhancement of attractive and repulsive optical forces between coupled whispering-gallery-mode resonators," *Optics Express*, vol. 13, pp. 8286-8295, 2005.

[125] H. Taniyama, M. Notomi, E. Kuramochi, T. Yamamoto, Y. Yoshikawa, Y. Torii, *et al.*, "Strong radiation force induced in two-dimensional photonic crystal slab cavities," *Physical Review B*, vol. 78, 2008.

[126] M. Eichenfield, C. P. Michael, R. Perahia, and O. Painter, "Actuation of micro-optomechanical systems via cavity-enhanced optical dipole forces," *Nature Photonics*, vol. 1, pp. 416-422, 2007.

[127] M. Li, W. H. Pernice, C. Xiong, T. Baehr-Jones, M. Hochberg, and H. X. Tang, "Harnessing optical forces in integrated photonic circuits," *Nature*, vol. 456, pp. 480-4, Nov 27 2008.

[128] H. Cai, K. J. Xu, A. Q. Liu, Q. Fang, M. B. Yu, G. Q. Lo, *et al.*, "Nano-opto-mechanical actuator driven by gradient optical force," *Applied Physics Letters*, vol. 100, p. 013108, 2012.

[129] J. Rosenberg, Q. Lin, and O. Painter, "Static and dynamic wavelength routing via the gradient optical force," *Nature Photonics*, vol. 3, pp. 478-483, Aug 2009.

[130] G. S. Wiederhecker, L. Chen, A. Gondarenko, and M. Lipson, "Controlling photonic structures using optical forces," *Nature*, vol. 462, pp. 633-U103, Dec 3 2009.

[131] F. Tian, G. Y. Zhou, Y. Du, F. S. Chau, J. Deng, X. S. Tang, *et al.*, "Energy-efficient utilization of bipolar optical forces in nano-optomechanical cavities," *Optics Express*, vol. 21, pp. 18398-18407, Jul 29 2013.

[132] A. Mizrahi and L. Schächter, "Two-slab all-optical spring," *Opt Lett*, vol. 32, pp. 692-694, 2007.

[133] B. S. Sheard, M. B. Gray, C. M. Mow-Lowry, D. E. McClelland, and S. E. Whitcomb, "Observation and characterization of an optical spring," *Physical Review A*, vol. 69, 2004.

[134] M. Hossein-Zadeh and K. J. Vahala, "Observation of optical spring effect in a microtoroidal optomechanical resonator," *Opt Lett*, vol. 32, pp. 1611-1613 2007.

[135] F. Tian, G. Zhou, Y. Du, F. S. Chau, and J. Deng, "Optical spring effect in nanoelectromechanical systems," *Applied Physics Letters*, vol. 105, p. 061115, 2014.

[136] F. Tian, G. Zhou, F. S. Chau, and J. Deng, "Torsional optical spring effect in coupled nanobeam photonic crystal cavities," *Opt Lett*, vol. 39, pp. 6289-92, Nov 1 2014.

[137] Q. Lin, J. Rosenberg, D. Chang, R. Camacho, M. Eichenfield, K. J. Vahala, *et al.*, "Coherent mixing of mechanical excitations in nano-optomechanical structures," *Nature Photonics,* vol. 4, pp. 236-242, 2010.

[138] P. Verlot, A. Tavernarakis, T. Briant, P. F. Cohadon, and A. Heidmann, "Backaction amplification and quantum limits in optomechanical measurements," *Phys Rev Lett,* vol. 104, p. 133602, Apr 2 2010.

[139] T. Weiss, C. Bruder, and A. Nunnenkamp, "Strong-coupling effects in dissipatively coupled optomechanical systems," *New Journal of Physics,* vol. 15, p. 045017, 2013.

[140] M. Hossein-Zadeh and K. J. Vahala, "An Optomechanical Oscillator on a Silicon Chip," *IEEE Journal of Selected Topics in Quantum Electronics,* vol. 16, pp. 276-287, 2010.

[141] I. Favero and K. Karrai, "Optomechanics of deformable optical cavities," *Nature Photonics,* vol. 3, pp. 201-205, 2009.

[142] T. J. Kippenberg and K. J. Vahala, "Cavity opto-mechanics," *Optics Express,* vol. 15, pp. 17172-17205, Dec 10 2007.

[143] O. Arcizet, P. F. Cohadon, T. Briant, M. Pinard, and A. Heidmann, "Radiation-pressure cooling and optomechanical instability of a micromirror," *Nature,* vol. 444, pp. 71-4, Nov 2 2006.

[144] G. Anetsberger, O. Arcizet, Q. P. Unterreithmeier, R. Rivière, A. Schliesser, E. M. Weig, *et al.*, "Near-field cavity optomechanics with nanomechanical oscillators," *Nature Physics,* vol. 5, pp. 909-914, 2009.

[145] J.-J. Li and K.-D. Zhu, "Nonlinear optical mass sensor with an optomechanical microresonator," *Applied Physics Letters,* vol. 101, p. 141905, 2012.

[146] S. Forstner, S. Prams, J. Knittel, E. D. van Ooijen, J. D. Swaim, G. I. Harris, *et al.*, "Cavity optomechanical magnetometer," *Phys Rev Lett,* vol. 108, p. 120801, Mar 23 2012.

[147] G. Anetsberger, R. Rivière, A. Schliesser, O. Arcizet, and T. J. Kippenberg, "Ultralow-dissipation optomechanical resonators on a chip," *Nature Photonics,* vol. 2, pp. 627-633, 2008.

[148] S. Weis, R. Riviere, S. Deleglise, E. Gavartin, O. Arcizet, A. Schliesser, *et al.*, "Optomechanically induced transparency," *Science,* vol. 330, pp. 1520-3, Dec 10 2010.

[149] H. Jing, S. K. Ozdemir, Z. Geng, J. Zhang, X. Y. Lu, B. Peng, *et al.*, "Optomechanically-induced transparency in parity-time-symmetric microresonators," *Sci Rep,* vol. 5, p. 9663, 2015.

[150] X. S. Jiang, Q. Lin, J. Rosenberg, K. Vahala, and O. Painter, "High-Q double-disk microcavities for cavity optomechanics," *Optics Express,* vol. 17, pp. 20911-20919, Nov 9 2009.

[151] M. Zhang, G. Luiz, S. Shah, G. Wiederhecker, and M. Lipson, "Eliminating anchor loss in optomechanical resonators using elastic wave interference," *Applied Physics Letters,* vol. 105, p. 051904, 2014.

[152] G. S. Wiederhecker, S. Manipatruni, S. Lee, and M. Lipson, "Broadband tuning

of optomechanical cavities," *Optics Express,* vol. 19, pp. 2782-2790, 2011.

[153] M. Eichenfield, R. Camacho, J. Chan, K. J. Vahala, and O. Painter, "A picogram- and nanometre-scale photonic-crystal optomechanical cavity," *Nature,* vol. 459, pp. 550-5, May 28 2009.

[154] T. P. M. Alegre, R. Perahia, and O. Painter, "Optomechanical zipper cavity lasers: theoretical analysis of tuning range and stability," *Optics Express,* vol. 18, pp. 7872-7885, 2010.

[155] J. Chan, M. Eichenfield, R. Camacho, and O. Painter, "Optical and mechanical design of a "zipper" photonic crystal optomechanical cavity," *Optics Express,* vol. 17, pp. 3802-3817, 2009.

[156] M. Notomi, H. Taniyama, S. Mitsugi, and E. Kuramochi, "Optomechanical wavelength and energy conversion in high- double-layer cavities of photonic crystal slabs," *Phys Rev Lett,* vol. 97, p. 023903, Jul 14 2006.

[157] J. Chan, A. H. Safavi-Naeini, J. T. Hill, S. n. Meenehan, and O. Painter, "Optimized optomechanical crystal cavity with acoustic radiation shield," *Applied Physics Letters,* vol. 101, p. 081115, 2012.

[158] M. Eichenfield, J. Chan, R. M. Camacho, K. J. Vahala, and O. Painter, "Optomechanical crystals," *Nature,* vol. 462, pp. 78-82, Nov 5 2009.

[159] J. T. Hill, A. H. Safavi-Naeini, J. Chan, and O. Painter, "Coherent optical wavelength conversion via cavity optomechanics," *Nature Communications,* vol. 3, Nov 2012.

[160] A. H. Safavi-Naeini, T. P. M. Alegre, M. Winger, and O. Painter, "Optomechanics in an ultrahigh-Q two-dimensional photonic crystal cavity," *Applied Physics Letters,* vol. 97, p. 181106, 2010.

[161] T. P. M. Alegre, A. Safavi-Naeini, M. Winger, and O. Painter, "Quasi-two-dimensional optomechanical crystals with a complete phononic bandgap," *Optics Express,* vol. 19, pp. 5658-5669, 2011.

[162] T. Antoni, A. G. Kuhn, T. Briant, P.-F. Cohadon, A. Heidmann, R. Braive, *et al.*, "Deformable two-dimensional photonic crystal slab for cavity optomechanics," *Opt Lett,* vol. 36, pp. 3434-3436, 2011.

[163] S. M. Meenehan, J. D. Cohen, S. Gröblacher, J. T. Hill, A. H. Safavi-Naeini, M. Aspelmeyer, *et al.*, "Silicon optomechanical crystal resonator at millikelvin temperatures," *Physical Review A,* vol. 90, 2014.

[164] D. Ramos, E. Gil-Santos, V. Pini, J. M. Llorens, M. Fernandez-Regulez, A. San Paulo, *et al.*, "Optomechanics with silicon nanowires by harnessing confined electromagnetic modes," *Nano Lett,* vol. 12, pp. 932-7, Feb 8 2012.

[165] A. G. Kuhn, M. Bahriz, O. Ducloux, C. Chartier, O. Le Traon, T. Briant, *et al.*, "A micropillar for cavity optomechanics," *Applied Physics Letters,* vol. 99, p. 121103, 2011.

[166] M. Ren, J. Huang, H. Cai, J. M. Tsai, J. Zhou, Z. Liu, *et al.*, "Nano-optomechanical Actuator and Pull-Back Instability," *Acs Nano,* vol. 7, pp. 1676-1681, 2013.

[167] E. Gavartin, P. Verlot, and T. J. Kippenberg, "A hybrid on-chip optomechanical

transducer for ultrasensitive force measurements," *Nat Nanotechnol,* vol. 7, pp. 509-14, Aug 2012.

[168] H. Li, Y. Chen, J. Noh, S. Tadesse, and M. Li, "Multichannel cavity optomechanics for all-optical amplification of radio frequency signals," *Nature Communications,* vol. 3, Oct 2012.

[169] J. D. Teufel, T. Donner, M. A. Castellanos-Beltran, J. W. Harlow, and K. W. Lehnert, "Nanomechanical motion measured with an imprecision below that at the standard quantum limit," *Nat Nanotechnol,* vol. 4, pp. 820-3, Dec 2009.

[170] M. Aspelmeyer, T. J. Kippenberg, and F. Marquardt, "Cavity optomechanics," *Reviews of Modern Physics,* vol. 86, pp. 1391-1452, 2014.

[171] L. Conti, M. De Rosa, F. Marin, L. Taffarello, and M. Cerdonio, "Room temperature gravitational wave bar detector with optomechanical readout," *Journal of Applied Physics,* vol. 93, p. 3589, 2003.

[172] K. Y. Fong, M. Poot, and H. X. Tang, "Nano-Optomechanical Resonators in Microfluidics," *Nano Lett,* vol. 15, pp. 6116-20, Sep 9 2015.

[173] E. Gil-Santos, C. Baker, D. T. Nguyen, W. Hease, C. Gomez, A. Lemaitre, *et al.*, "High-frequency nano-optomechanical disk resonators in liquids," *Nat Nanotechnol,* vol. 10, pp. 810-6, Sep 2015.

[174] F. Liu, S. Alaie, Z. C. Leseman, and M. Hossein-Zadeh, "Sub-pg mass sensing and measurement with an optomechanical oscillator," *Opt Express,* vol. 21, pp. 19555-67, Aug 26 2013.

[175] Y. Chen and A. Pepin, "Nanofabrication: Conventional and nonconventional methods," *Electrophoresis,* vol. 22, pp. 187-207, Jan 2001.

[176] Z. W. Kowalski and I. W. Rangelow, "Microelectronic and Medical Applications of an Ion-Beam Milling System," *Journal of Materials Science,* vol. 18, pp. 741-752, 1983.

[177] H. Jansen, H. Gardeniers, M. deBoer, M. Elwenspoek, and J. Fluitman, "A survey on the reactive ion etching of silicon in microtechnology," *Journal of Micromechanics and Microengineering,* vol. 6, pp. 14-28, Mar 1996.

[178] S. W. Pang, D. D. Rathman, D. J. Silversmith, R. W. Mountain, and P. D. DeGraff, "Damage induced in Si by ion milling or reactive ion etching," *Journal of Applied Physics,* vol. 54, p. 3272, 1983.

[179] F. Marty, L. Rousseau, B. Saadany, B. Mercier, O. Français, Y. Mita, *et al.*, "Advanced etching of silicon based on deep reactive ion etching for silicon high aspect ratio microstructures and three-dimensional micro- and nanostructures," *Microelectronics Journal,* vol. 36, pp. 673-677, 2005.

[180] F. Laermer and A. Urban, "Challenges, developments and applications of silicon deep reactive ion etching," *Microelectronic Engineering,* vol. 67-68, pp. 349-355, 2003.

[181] K. L. Choy, "Chemical vapour deposition of coatings," *Progress in Materials Science,* vol. 48, pp. 57-170, 2003.

[182] U. Helmersson, M. Lattemann, J. Bohlmark, A. P. Ehiasarian, and J. T. Gudmundsson, "Ionized physical vapor deposition (IPVD): A review of

technology and applications," *Thin Solid Films,* vol. 513, pp. 1-24, 2006.

[183] J. Singh and D. E. Wolfe, "Nano and macro-structured component fabrication by electron beam-physical vapor deposition (EB-PVD)," *Journal of Materials Science,* vol. 40, pp. 1-26, Jan 1 2005.

[184] S. M. Rossnagel, "Metal ion deposition from ionized mangetron sputtering discharge," *Journal of Vacuum Science & Technology B: Microelectronics and Nanometer Structures,* vol. 12, p. 449, 1994.

[185] Y. I. Lee, K. H. Park, J. Lee, C. S. Lee, H. J. Yoo, C. J. Kim, *et al.*, "Dry release for surface micromachining with HF vapor-phase etching," *Journal of Microelectromechanical Systems,* vol. 6, pp. 226-233, Sep 1997.

[186] J. D. Joannopoulos, S. G. Johnson, J. N. Winn, and R. D. Meade, *Photonic crystals: molding the flow of light*: Princeton university press, 2011.

[187] Q. M. Quan and M. Loncar, "Deterministic design of wavelength scale, ultra-high Q photonic crystal nanobeam cavities," *Optics Express,* vol. 19, pp. 18529-18542, Sep 12 2011.

[188] Q. M. Quan, P. B. Deotare, and M. Loncar, "Photonic crystal nanobeam cavity strongly coupled to the feeding waveguide," *Applied Physics Letters,* vol. 96, May 17 2010.

[189] Q. Li, T. Wang, Y. Su, M. Yan, and M. Qiu, "Coupled mode theory analysis of mode-splitting in coupled cavity system," *Optics Express,* vol. 18, pp. 8367-8382, 2010.

[190] A. Yariv, "Coupled-Mode Theory for Guided-Wave Optics," *IEEE Journal of Quantum Electronics,* vol. 9, pp. 919-933, 1973.

[191] A. Hardy and W. Streifer, "Coupled Mode Theory of Parallel Waveguides," *Journal of Lightwave Technology,* vol. 3, pp. 1135-1146, 1985.

[192] H. Haus, W. Huang, S. Kawakami, and N. Whitaker, "Coupled-mode theory of optical waveguides," *Journal of Lightwave Technology,* vol. 5, pp. 16-23, 1987.

[193] W.-P. Huang, "Coupled-mode theory for optical waveguides an overview," *Journal of the Optical Society of America A,* vol. 11, pp. 963-983, 1994.

[194] H. A. Haus and W. Huang, "Coupled-mode theory," *Proc. IEEE,* vol. 79, pp. 1505-1518, 1991.

[195] P. B. Deotare, I. Bulu, I. W. Frank, Q. Quan, Y. Zhang, R. Ilic, *et al.*, "All optical reconfiguration of optomechanical filters," *Nat Commun,* vol. 3, p. 846, 2012.

[196] S. Haddadi, P. Hamel, G. Beaudoin, I. Sagnes, C. Sauvan, P. Lalanne, *et al.*, "Photonic molecules: tailoring the coupling strength and sign," *Optics Express,* vol. 22, pp. 12359-12368, May 19 2014.

[197] A. Majumdar, A. Rundquist, M. Bajcsy, and J. Vučković, "Cavity quantum electrodynamics with a single quantum dot coupled to a photonic molecule," *Physical Review B,* vol. 86, 2012.

[198] A. Dousse, J. Suffczynski, A. Beveratos, O. Krebs, A. Lemaitre, I. Sagnes, *et al.*, "Ultrabright source of entangled photon pairs," *Nature,* vol. 466, pp. 217-20, Jul 8 2010.

[199] J. Li, R. Yu, C. Ding, W. Wang, and Y. Wu, "Optical-frequency-comb generation

and entanglement with low-power optical input in a photonic molecule," *Physical Review A,* vol. 90, 2014.

[200] S. Liu, R. Yu, J. Li, and Y. Wu, "Creation of quantum entanglement with two separate diamond nitrogen vacancy centers coupled to a photonic molecule," *Journal of Applied Physics,* vol. 114, p. 244306, 2013.

[201] D. Gerace, H. E. Türeci, A. Imamoglu, V. Giovannetti, and R. Fazio, "The quantum-optical Josephson interferometer," *Nature Physics,* vol. 5, pp. 281-284, 2009.

[202] D. Van Thourhout and J. Roels, "Optomechanical device actuation through the optical gradient force," *Nature Photonics,* vol. 4, pp. 211-217, Apr 2010.

[203] F. Tian, G. Y. Zhou, Y. Du, F. S. Chau, J. Deng, S. L. Teo, *et al.*, "Nanoelectromechanical-systems-controlled bistability of double-coupled photonic crystal cavities," *Optics Letters,* vol. 38, pp. 3394-3397, Sep 1 2013.

[204] A. Di Virgilio, L. Barsotti, S. Braccini, C. Bradaschia, G. Cella, C. Corda, *et al.*, "Experimental evidence for an optical spring," *Physical Review A,* vol. 74, 2006.